Department of Physics and Astronomy

University of Heidelberg

Master thesis

in Physics

submitted by

Johannes Maria René Welter

born in Starnberg

2013

Oscillation phenomenology of gauged sterile neutrinos

This Master thesis has been carried out by Johannes Maria René Welter

at the

Max Planck Institute for Nuclear Physics

under the supervision of

Dr. Joachim Kopp

Oszillationsphänomene geeichter steriler Neutrinos:

Als mögliche Lösung für aktuell ungeklärte Anomalien in Experimenten auf der Suche nach dunkler Materie schlug Pospelov in 2011 eine Erweiterung des Standard Modells vor, die sterile Neutrinos mit Massen der Größenordnung eV einführt, welche über ein neues baryonisches Eichboson mit Materie wechselwirken. Kürzlich haben Karagiorgi, Shaevitz und Konrad die Auswirkungen dieses Modells auf die "short-baseline anomaly" untersucht. Ihre Ergebnisse weisen darauf hin, dass sterile Neutrinos, die stärker als die schwache Kraft mit Baryonen wechselwirken, die Möglichkeit haben, die Anomalie zu erklären. In dieser Arbeit untersuchen wir die Oszillations-Phenomenologie dieses Modells. In diesem Rahmen leiten wir erneut analytische Näherungsformeln für die Oszillationswahrscheinlichkeiten her, welche die vormals berechneten korrigieren. Wir führen außerdem eine numerische χ^2-Analyse mit Datensätzen von MINOS, MiniBooNE und solaren Experimenten durch. Die Resultate zeigen, dass sich die Unstimmigkeiten, die man in einfachen sterile-Neutrino-Szenarien erhält, nicht mit baryonischen sterilen Neutrinos auflösen lassen. Unter der Annahme, dass das MiniBooNE-Signal durch aktiv-sterile Mischung im Rahmen eines Modells aus drei aktiven und einem sterilen Neutrino erklärt werden kann, schließen wir, dass das baryonische Modell für den interessanten Bereich des neuen Materiepotentials unwahrscheinlich ist.

Oscillation Phenomenology of gauged sterile neutrinos:

As a possible solution to currently unresolved anomalies in dark matter direct detection experiments a Standard Model extension was proposed by Pospelov in 2011, containing a sterile neutrino with mass of the order eV, which interacts with matter via a new baryonic gauge boson. Recently, the impact of this model on the short-baseline anomaly has been studied by Karagiorgi, Shaevitz and Konrad. Their results indicate that sterile neutrinos interacting with baryons stronger than weak force have the possibility to explain the tensions of the anomaly. In this thesis, we investigate the oscillation phenomenology of this model. We re-derive analytical approximations for the oscillation probabilities in this framework and revise the previous result. We perform a numerical χ^2 analysis with data sets from MINOS, MiniBooNE and solar experiments. The results show that baryonic sterile neutrinos can not resolve the tensions obtained in simple sterile neutrino scenarios. Assuming that the MiniBooNE signal is due to active-sterile mixing in a three active plus one sterile neutrino framework we conclude that the interesting parameter range for the baryonic matter potential is disfavoured.

Contents

Chapter 1

Introduction

Today, the Standard Model (SM) of particle physics based on the principles of General Relativity and Quantum Field Theory is founded on numerous measurements yielding accurate agreement between theory and experiment. In the last year, the LHC (Large Hadron Collider) discovered a new particle [1, 2] of mass $\sim 125\,\mathrm{GeV}$, which is compatible with a SM Higgs boson. The analysis of this Higgs-like particle is not finished yet, but so far the interaction properties are consistent with those expected for a SM Higgs [3, 4]. A confirmation that this particle is indeed the SM Higgs would complete the model and contribute to its great success.

The phenomenon of neutrino oscillations first proposed by Pontecorvo in 1968 [5] and proven by various experiments in the last decades is by now accepted as an experimental fact. It inevitably leads to the conclusion that the SM needs to be extended to account for small, but non-zero neutrino masses. This can be done by adding sterile right-handed neutrinos and introduce Dirac and/or Majorana mass terms in the SM Lagrangian. Usually the right-handed neutrinos are assumed to be very heavy so that they can be integrated out and do not contribute to flavour mixing. In the following we will refer to this framework for the description of three flavour neutrino oscillations as the *standard picture*. In total, six additional parameters are introduced: three mixing angles, θ_{12}, θ_{23}, θ_{13}, two mass squared differences $\Delta m^2_{21} = m^2_2 - m^2_1$, $\Delta m^2_{31} = m^2_3 - m^2_1$ and one phase δ. They can explain the majority of the results obtained in neutrino oscillation experiments. While (Δm^2_{21}, θ_{12}) has been determined by the observation of flavour transitions from solar electron neutrinos into muon neutrinos, ($|\Delta m^2_{31}|$, θ_{23}) could be used to explain oscillations of atmospheric neutrinos. A measurement of θ_{13} was made this year by accelerator and reactor neutrino experiments. The value of δ and the sign of Δm^2_{31} are not determined yet[1].

[1] The sign of Δm^2_{21} is positive and was determined by solar flavour transitions, which require resonant

Results of different type of experiments give evidence for neutrino oscillations, which are not compatible with the standard picture. These *anomalies* motivate the introduction of mixing between active and sterile neutrinos. It has been shown [6] that in simple sterile neutrino scenarios it is not possible to resolve these tensions. A recent publication [7] by Karagiorgi, Shaevitz and Conrad considered a model[2], in which a sterile neutrino with strong[3] non-standard matter interactions is introduced. They analysed the LSND/MiniBooNE anomaly and calculated analytical approximations for the oscillation probabilities.

This work is organized in the following way. The basic formalism for the mathematical description of neutrino oscillation is summarized in chapter two. We than give an overview of the current experimental status of neutrino oscillation experiments in chapter three, where we also explain the tensions arising from the Gallium, the short-baseline as well as the reactor neutrino anomaly. In chapter four, we describe the motivation and basic ideas of the baryonic neutrino model and re-derive analytical expressions for the oscillation probabilities in this scenario resulting in an important correction of the previously derived formula. A quantitative phenomenological investigation of this model is presented in chapter five. We perform a numerical χ^2 analysis in a three active plus one sterile neutrino oscillation framework allowing for large values of the baryonic matter potential. The simulation is done for experimental data sets from MiniBooNE, MINOS and solar experiments. It shows that the tensions due to the short-baseline anomaly can not be resolved by the baryonic neutrino model. Finally we summarize this work including a discussion of our results and draw conclusions in chapter six.

enhancement through matter effects as described in section 2.3.2. Therefore the neutrino mass hierarchy is given by the sign of Δm^2_{31}. $\Delta m^2_{31} > 0$ is called *normal hierarchy* and $\Delta m^2_{31} < 0$ *inverted hierarchy*.

[2] This model was originally proposed by Pospelov [8] in order to explain signals in dark matter direct detection experiments. It was also studied in [9, 10].

[3] The interesting parameter range for this interaction is 10^1 to 10^4 times stronger than the weak force.

Chapter 2

Model and formalism in the standard picture

2.1 Neutrino mass and mixing matrix

2.1.1 Most general neutrino mass term

The most simple way to introduce neutrino masses is to add right-handed neutrinos N_R, which are "sterile", i.e. they are total singlets under the SM gauge group. This is done by introducing the Yukawa coupling

$$\mathcal{L}_{\mathrm{Y}} = -\sum_{i,j} y^{ij} \bar{L}_L^i N_R^j (i\tau_2 h^*) \tag{2.1}$$

with the SM Higgs doublet h, the second Pauli matrix τ_2 and the lepton doublet L_L. Here we assume the general case of n lepton generations, i.e. the lepton doublet is composed of the neutrino fields ν_L and charged lepton fields l_L, which are both n dimensional vectors in flavour space: $L_L^i = (\nu_L^i,\, l_L^i)^T$. After the electroweak symmetry breaking by the nonzero vacuum expectation value v of the Higgs field this yields

$$\mathcal{L}_{\mathrm{Dirac}} = -\sum_{i,j} y^{ij} \frac{v}{\sqrt{2}} \bar{\nu}_L^i N_R^j + h.c. \equiv \sum_{i,j} -\bar{\nu}_L^i m_D^{ji*} N_R^j + h.c., \tag{2.2}$$

where we have defined the Dirac mass matrix m_D.

Another possibility are left- or right-handed Majorana mass terms:

$$\begin{aligned}\mathcal{L}_{\text{Majorana}} &= -\frac{1}{2}\sum_{i,j}\overline{\left(\nu_L^i\right)^C} m_L^{ij}\nu_L^i - \frac{1}{2}\sum_{i,j}\overline{\left(N_R^i\right)^C} m_R^{ij} N_R^j + h.c. \\ &= -\frac{1}{2}\sum_{i,j}\left(\nu_L^i\right)^T C m_L^{ij}\nu_L^j - \frac{1}{2}\sum_{i,j}\left(N_R^i\right)^T C\left(m_R^{ij}\right)^* N_R^j + h.c. \quad (2.3)\end{aligned}$$

Here the matrix multiplication in flavour space is omitted for simplicity and $C = i\gamma^2\gamma^0$ is the charge conjugation operator. The introduction of such mass terms would break lepton number conservation. However, this symmetry is not imposed a priori in the SM. Therefore, if one introduces right-handed Majorana neutrinos, a right-handed Majorana mass term would be a direct consequence. To introduce Majorana mass terms for left-handed neutrinos in a gauge invariant way requires more effort (via an isotriplet Higgs field).

The most general neutrino mass term (including a left-handed Majorana mass m_L) for n neutrino flavours is then [11]:

$$\mathcal{L}_m = \mathcal{L}_{\text{Dirac}} + \mathcal{L}_{\text{Majorana}} = -\frac{1}{2} n_L^T C \mathcal{M} n_L + h.c. \quad (2.4)$$

Here $n_L = \begin{pmatrix}\nu_L \\ (N_R)^C\end{pmatrix}$ is a $2n$ component vector and $\mathcal{M}$ is the mass matrix, composed of the Dirac mass matrix m_D and the left- and right-handed Majorana mass matrices m_L, m_R:

$$\mathcal{M} = \begin{pmatrix} m_L & m_D \\ m_D^T & m_R \end{pmatrix} \quad (2.5)$$

This matrix is in general not diagonal. In order to study the effect of non-zero neutrino masses it is convenient to diagonalize $\mathcal{M}$, which corresponds to changing the basis from neutrino flavour eigenstates to mass eigenstates.

2.1.2 Diagonalizing the neutrino mass matrix

For $n = 3$ the part of the Lagrangian containing neutrino masses in flavour basis reads

$$\mathcal{L}_{\text{mass}} = -\frac{1}{2}\begin{pmatrix}\nu_L \\ (N_R)^C\end{pmatrix}^T C \begin{pmatrix} m_L & m_D \\ m_D^T & m_R \end{pmatrix}\begin{pmatrix}\nu_L \\ (N_R)^C\end{pmatrix} + h.c., \quad (2.6)$$

where now $\nu_L = \left(\nu_L^e, \nu_L^\mu, \nu_L^\tau\right)^T$ and $N_R = \left(N_R^1, N_R^2, N_R^3\right)^T$ are the left- and right-handed neutrinos respectively. As we will see later, diagonalizing this term has an impact on the leptonic charge current interactions, which in flavour basis have the simple form:

$$\mathcal{L}_{\mathrm{CC}} = \frac{g}{\sqrt{2}} W_\mu^+ \bar{l}_L \gamma^\mu \nu_L + h.c. \tag{2.7}$$

For the charged leptons the flavour basis l_L is per definition identical to the mass eigenstates, but in a general Lagrangian the basis of the charged leptons a priori does not have to agree with the mass eigenstates. Therefore, if we start with a general arbitrary basis l'_L, the charged lepton mass term can also have non-zero off-diagonal entries and thus needs to be diagonalized likewise the neutrino mass matrix $\mathcal{M}$. In order to do so one introduces unitary matrices U_L (6×6 matrix) and V_L (3×3 matrix) relating the flavour eigenstates to the mass eigenstates. Only under this new basis the neutrino mass matrix $\mathcal{M}$ and the charged lepton mass matrix become diagonal

$$\begin{aligned}
\begin{pmatrix} \nu_L \\ (N_R)^C \end{pmatrix} &= U_L \begin{pmatrix} \nu_L^1 \\ \nu_L^2 \\ \nu_L^3 \\ \nu_L^4 \\ \nu_L^5 \\ \nu_L^6 \end{pmatrix} = U_L \nu'_L, \\
l_L = \begin{pmatrix} e_L \\ \mu_L \\ \tau_L \end{pmatrix} &= V_L \begin{pmatrix} e'_L \\ \mu'_L \\ \tau'_L \end{pmatrix} = V_L l'_L.
\end{aligned} \tag{2.8}$$

The charge current term then reads:

$$\mathcal{L}_{\mathrm{CC}} = \frac{g}{\sqrt{2}} \bar{l}_L \gamma^\mu \left(V_L^\dagger \tilde{U}_L \nu'_L\right) W_\mu^+ + h.c. \tag{2.9}$$

The matrix $\tilde{U}_L$ is the upper 3×6 block of the 6×6 matrix U_L. In the pure Dirac case the matrix U_L is only 3×3 dimensional and this reduces to $\tilde{U}_L \equiv U_L$. $U = V_L^\dagger U_L$ is then called the leptonic mixing matrix or PMNS-matrix (Pontecorvo-Maki-Nakagawa-Sakata matrix). The situation is similar in the pure Majorana case. Only in the most general Dirac+Majorana case there can be mixing into the right-handed sterile neutrino states N_R. Mixings from sterile into sterile states can be absorbed in the redefinition of the flavour basis, because they do not appear in charge current

interactions [11].

One can absorb the transformation for the charged leptons into the neutrino mixing matrix. Thus, we write $l'_L \equiv l_L$ in the following and the mixing matrix becomes

$$U = \begin{pmatrix} & V_L^\dagger \tilde{U}_L & & & & \\ & & & & & \\ * & * & * & 1 & 0 & 0 \\ * & * & * & 0 & 1 & 0, \\ * & * & * & 0 & 0 & 1 \end{pmatrix} \tag{2.10}$$

where the elements marked with $*$ are such that the matrix is unitary $UU^\dagger = \mathbb{1}$. The masses of N_R are usually assumed to be very heavy, so that they can be integrated out, i.e. the matrix elements in the upper right and lower left 3×3 block of U are negligible and thus the right-handed neutrinos are effectively decoupled. This finally leads to the three dimensional mixing matrix in the standard picture of neutrino oscillations $V_L^\dagger \tilde{U}_L$. In the following this matrix is referred to as U. In the context of this standard picture U is assumed to be unitary[1] and it is therefore convenient to assume pure Dirac neutrinos which are composed of the right- and left-handed neutrino components $\nu_\alpha = \nu_L^\alpha + \nu_R^\alpha$.

In this way the transformation between the neutrino matter fields $\nu'_i = \nu_1, \nu_2, \nu_3$ and flavour fields $\nu_\alpha = \nu_e, \nu_\mu, \nu_\tau$ can be written as

$$\nu_\alpha = \sum_i U_{\alpha i} \nu'_i. \tag{2.11}$$

In order to assign this transformation to the quantum states, consider the decomposition of a neutrino field ν'_i into its creation and annihilation operators[2] [12]:

$$\nu'_i(x) = \sum_{\text{spin } s=\pm} \int \frac{\mathrm{d}^3 p}{(2\pi)^2 2E} \left[b'^i_s(p) u_s(p) e^{-i(Et-px)} + d'^{\dagger i}_s(p) v_s(p) e^{i(Et-px)} \right]. \tag{2.12}$$

Here $u_\pm(p)$ and $v_\pm(p)$ are four-component spinors, solving the Dirac equation, $b'^i_\pm(p)$ is the annihilation operator of the neutrino and $d'^{\dagger i}_\pm(p)$ is the creation operator of

[1] In the general Dirac and Majorana case U is approximately unitary, since the entries in the mixing matrix in the upper right and lower left 3×3 block can be neglected. If Majorana masses are absent, these entries are zero and unitarity become exact.

[2] This can be done only for free particles. For now, let us consider a neutrino freely propagating in vacuum.

the anti-neutrino. Omitting the spin and momentum dependencies for notational simplicity and using equation 2.11 we find

$$\nu_\alpha = \sum_i \sum_s \int \frac{\mathrm{d}^3 p}{(2\pi)^2 2E} \left[U_{\alpha i} b'^i u e^{-i(Et-px)} + U_{\alpha i} d'^{\dagger i} v e^{i(Et-px)} \right] \tag{2.13}$$

and finally can identify the creation operator of the neutrino flavour eigenstate:

$$b^{\dagger\alpha} = \left(\sum_i U_{\alpha i} b'^i \right)^\dagger = \sum_i U^*_{\alpha i} b'^{\dagger i}. \tag{2.14}$$

Note that in general there are some problems with defining creation and annihilation operators for the eigenstates of the weak interaction. See references [13, 14] for more details and a correct treatment.

This leads us to the transformation written in quantum mechanical notation:

$$|\nu_\alpha\rangle = b^{\dagger\alpha} |0\rangle = \sum_i U^*_{\alpha i} b'^{\dagger i} |0\rangle = \sum_i U^*_{\alpha i} |\nu'_i\rangle . \tag{2.15}$$

In the following we drop the primes and use Greek indicees to indicate flavour eigenstates and Latin indicees to indicate mass eigenstates.

The Hamiltonian for neutrinos propagating in vacuum can now be written in flavour basis in the simple form

$$H_{\text{flavour}} = U \,\mathrm{diag}\,(\lambda_1, \lambda_2, \lambda_3)\, U^\dagger. \tag{2.16}$$

2.2 Neutrino oscillations in vacuum

Consider a neutrino source producing relativistic neutrinos of flavour α via charge current interactions traveling over a length L until the neutrino will be detected again via a charge current interaction. Then the probability that the detected neutrino has flavour β is given by the square of the quantum mechanical transition amplitude

$$\begin{aligned} P_{\nu_\alpha \to \nu_\beta} &= \left| \langle \nu_\beta | \nu_\alpha(t) \rangle \right|^2 \\ &= \left| \sum_i \langle \nu_\beta | \, U^*_{\alpha i} \, | \nu_i(t) \rangle \right|^2 \\ &= \left| \sum_{i,\gamma} \langle \nu_\beta | \, U^*_{\alpha i} e^{-itE_i} U_{\gamma i} \, | \nu_\gamma \rangle \right|^2 \end{aligned}$$

$$
\begin{aligned}
&= \Big| \sum_i U^*_{\alpha i} e^{-iLE_i} U_{\beta i} \Big|^2 \\
&\approx \Big| \sum_i U^*_{\alpha i} e^{-iL|\mathbf{p}|} e^{-iL\frac{m_1^2}{2E}} e^{-iL\frac{\Delta m^2_{i1}}{2E}} U_{\beta i} \Big|^2 \\
&= \Big| \sum_i U^*_{\alpha i} e^{-iL\frac{\Delta m^2_{i1}}{2E}} U_{\beta i} \Big|^2 . \qquad (2.17)
\end{aligned}
$$

Here E_i are the energies of the mass eigenstates which (in vacuum) corresponds to the energy eigenstates and $\Delta m^2_{ij} = \Delta m^2_i - \Delta m^2_j$. This simplified calculation assumes a relativistic neutrino $t \approx L$ and a definite three-momentum that is the same for all the contributing mass eigenstates, so that one can approximate $E_i \approx |\mathbf{p}| + \frac{m_i^2}{2|\mathbf{p}|} \approx |\mathbf{p}| + \frac{m_i^2}{2E}$. Although this gives the right result, the correct treatment would require more quantum mechanical effort. It has been shown that derivations including the momentum spread of the neutrino and using the correct quantum field theoretical formalism respectively lead to the same formula [15, 16].

The above calculation assumes that the neutrino stays in a coherent superposition of mass eigenstates until it will be detected. The correctness of this assumption depends on the so called coherence length. This is the characteristic length scale at which the wave packets, corresponding to different mass eigenstates, become spatially separated [16]:

$$
L_{\text{coh}} = \frac{4\sqrt{2}E^2}{|\Delta m^2|} \Delta L. \qquad (2.18)
$$

Here ΔL is the total effective spacial uncertainty, which can be obtained from the uncertainties in the detection and production processes [16]: $\Delta L^2 = \Delta L_d^2 + \Delta L_p^2$. If $L \gg L_{\text{coh}}$, the superposition loses the coherence on the way between source and detection. In this case the oscillation probability is calculated as follows:

$$
\begin{aligned}
P^{\text{incoh}}_{\nu_\alpha \to \nu_\beta} &= \sum_i P_{\nu_\alpha \to \nu_i} \cdot P_{\nu_i \to \nu_\beta} \\
&= \sum_i \big| \langle \nu_i | \nu_\alpha(t) \rangle \big|^2 \cdot \big| \langle \nu_\beta | \nu_i \rangle \big|^2 \\
&= \sum_i \Big| U^*_{\alpha i} e^{-iL\frac{\Delta m^2_{i1}}{2E}} \Big|^2 \cdot |U_{\beta i}|^2 \\
&= \sum_i |U_{\alpha i}|^2 \cdot |U_{\beta i}|^2 . \qquad (2.19)
\end{aligned}
$$

The essential difference to equation 2.17 is that one has to sum over the product of transition probabilities instead of squaring the whole amplitude $\langle\nu_\beta|\nu_\alpha(t)\rangle$.

2.2.1 Two flavour oscillations

In the simplified case of only two Dirac neutrinos, e.g. electron and muon, the mixing matrix can be parametrized by one mixing angle θ [3]:

$$U = \begin{pmatrix} \cos\theta & \sin\theta \\ -\sin\theta & \cos\theta \end{pmatrix}. \tag{2.20}$$

Together with the formula 2.17 the probability for an electron neutrino of energy E being detected as a muon neutrino after it traveled a distance L can be calculated by

$$\begin{aligned} P_{\nu_e\to\nu_\mu} &= \Big|\sum_i U^*_{ei} e^{-iL\frac{\Delta m^2_{i1}}{2E}} U_{\mu i}\Big|^2 \\ &= \left|U^*_{e1}U_{\mu 1} + U^*_{e2}e^{-iL\frac{\Delta m^2_{21}}{2E}}U_{\mu 2}\right|^2 \\ &= \sin^2\theta\cos^2\theta\left|-1+e^{-iL\frac{\Delta m^2_{21}}{2E}}\right|^2 \\ &= 4\sin^2\theta\cos^2\theta\sin^2\left(\frac{\Delta m^2_{21}}{4E}L\right) \\ &= \sin^2 2\theta\sin^2\left(\frac{\Delta m^2_{21}}{4E}L\right). \end{aligned} \tag{2.21}$$

Correspondingly, the probability that the electron neutrino is detected in its original flavour state is

$$P_{\nu_e\to\nu_e} = 1 - \sin^2 2\theta\sin^2\left(\frac{\Delta m^2_{21}}{4E}L\right). \tag{2.22}$$

In figure 2.1 the two flavour survival and transition probability is shown. These probabilities are oscillating with the amplitude given by the mixing angle $\sin^2 2\theta$ and the oscillation length L_{osc} given by the neutrino energy and its mass $L_{\text{osc}} = \frac{4\pi E}{\Delta m^2_{21}}$. The maximal "disappearance" of electrons can be found at distances $L = (n+1/2)L_{\text{osc}}$, $n \in \mathbb{N}$ away from the neutrino source as long as the neutrino stays in a coherent superposition of mass eigenstates. If $\frac{\Delta m^2 L}{2E} \gg 1$, the oscillation is effectively averaged out due to the finite detector energy and space resolution. Therefore, an experiment

[3] For Majorana neutrinos, there would be an additional phase, which however does not contribute to neutrino oscillations, see e.g. [16].

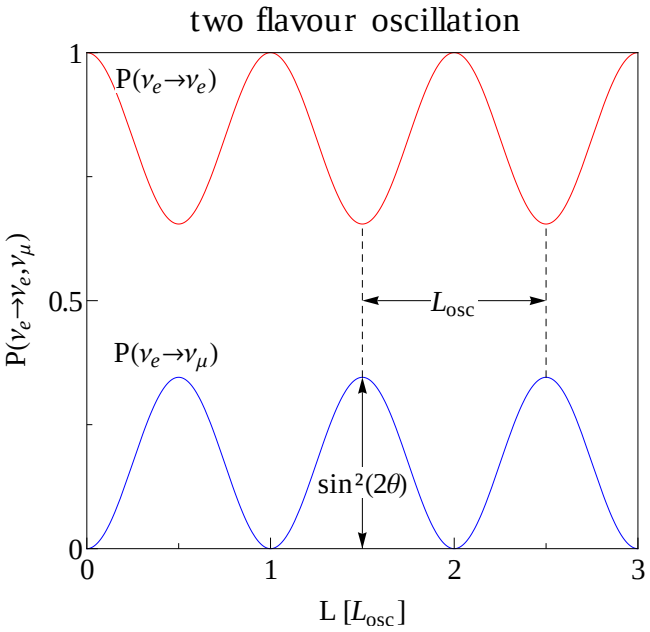

Figure 2.1: The two flavour oscillation probabilities.

would only be sensitive to the amplitude. An experiment with $\frac{\Delta m^2 L}{2E} \ll 1$ on the other hand could not measure flavour transitions at all.

2.2.2 Three flavour oscillations

For the general case of n neutrino flavours the unitary mixing matrix U depends on $n(n-1)/2$ rotation angles and $n(n+1)/2$ complex phases. Since U appears only in the leptonic charge current interaction term and the rest of the Lagrangian is invariant under a global phase shift of the left-handed charged lepton fields, one can eliminate n phases by an appropriate phase shift and a redefinition of the lepton fields. In addition, one can eliminate $n-1$ phases by a redefinition of the neutrino fields[4] leading to a final amount of $n(n-3)/2+1$ complex phases [16].

For $n = 3$ flavour neutrino oscillations U is therefore usually parametrized by 3

[4]Note that in the case of Majorana neutrinos one does not have the freedom to eliminate these $n-1$ phases. However neutrino oscillation experiments are not sensitive to such Majorana phases, because they would cancel in the calculation of equation 2.17 [11]. See also [16], [17] for more details.

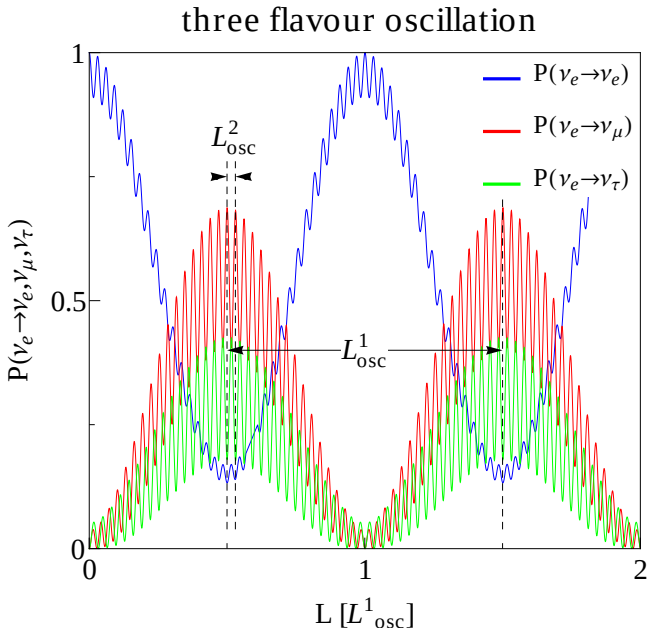

Figure 2.2: The three flavour oscillation probabilities.

rotation matrices and 1 complex phase:

$$
\begin{aligned}
U &= \begin{pmatrix} U_{e1} & U_{e2} & U_{e3} \\ U_{\mu 1} & U_{\mu 2} & U_{\mu 3} \\ U_{\tau 1} & U_{\tau 2} & U_{\tau 3} \end{pmatrix} \\
&= \begin{pmatrix} 1 & 0 & 0 \\ 0 & c_{23} & s_{23} \\ 0 & -s_{23} & c_{23} \end{pmatrix} \begin{pmatrix} c_{13} & 0 & s_{13}e^{-i\delta} \\ 0 & 1 & 0 \\ -s_{13}e^{i\delta} & 0 & c_{13} \end{pmatrix} \begin{pmatrix} c_{12} & s_{12} & 0 \\ -s_{12} & c_{12} & 0 \\ 0 & 0 & 1 \end{pmatrix} \\
&= \begin{pmatrix} c_{12}c_{13} & s_{12}c_{13} & s_{13}e^{-i\delta} \\ -s_{12}c_{23} - c_{12}s_{13}s_{23}e^{i\delta} & c_{12}c_{23} - s_{12}s_{13}s_{23}e^{i\delta} & c_{13}s_{23} \\ s_{12}s_{23} - c_{12}s_{13}c_{23}e^{i\delta} & -c_{12}s_{23} - s_{12}s_{13}c_{23}e^{i\delta} & c_{13}c_{23} \end{pmatrix}. \qquad (2.23)
\end{aligned}
$$

Here the abbreviation $s_{ij} = \sin\theta_{ij}$ and $c_{ij} = \cos\theta_{ij}$ is used.

Figure 2.2 illustrates the oscillation probabilities in the three flavour regime with realistic values for the mixing parameters as known today. One can clearly identify the oscillation lengths $L^1_{\text{osc}} = \frac{4\pi E}{\Delta m^2_{21}}$ and $L^2_{\text{osc}} = \frac{4\pi E}{\Delta m^2_{31}} \approx \frac{4\pi E}{\Delta m^2_{32}}$, given by the mass differences similar to the two flavour case.

2.3 Neutrino oscillations in matter

2.3.1 Derivation of the matter potential

The first strong evidence that neutrino oscillations are affected by matter were the results of solar neutrino measurements. There one observed a deficit in electron neutrinos compared to the predictions of all current solar models. This discrepancy between prediction and observation could be explained by the so called Mikheyev-Smirnov-Wolfenstein (MSW) effect, which is the resonant enhancement of neutrino oscillations due to interactions with matter. Those interactions are proportional to the square of the Fermi constant G_F and therefore very small. However, they can experience a matter potential through coherent elastic forward scattering, where their momentum stays unchanged. This potential is also proportional to G_F, but in the case it is approximately as large as the kinetic energy difference $\frac{\Delta m^2}{2E}$ it can become quite important for neutrino oscillations.

At energies far below the Z^0 and $W^\pm$ masses the neutrino charge current interactions with matter is approximately given by

$$\begin{aligned} -\mathcal{L}_{\mathrm{CC}} &= \frac{G_F}{\sqrt{2}} \left[\bar{e}\gamma_\mu \left(1-\gamma_5\right) \nu_e\right] \left[\bar{\nu}_e \gamma_\mu \left(1-\gamma_5\right) e\right] \\ &= \frac{G_F}{\sqrt{2}} \left[\bar{e}\gamma_\mu \left(1-\gamma_5\right) e\right] \left[\bar{\nu}_e \gamma_\mu \left(1-\gamma_5\right) \nu_e\right], \end{aligned} \tag{2.24}$$

where in the second step the Fierz transformation was used. In order to obtain the averaged matter-induced potential for the neutrino propagation in matter the electron degrees of freedom have to be integrated out. For unpolarized matter of zero mean velocity this results in the potential [11]

$$V_{\mathrm{CC}} = -\left\langle \mathcal{L}_{\mathrm{CC}} \right\rangle_{\mathrm{electron}} = \sqrt{2} G_F N_e. \tag{2.25}$$

Here N_e is the number density of electrons in the matter, where the neutrino propagates. On the earth it is approximately $N_e = Y_e \cdot \rho / m_N \approx 0.5 \cdot \rho / m_N$ with Y_e being the number of electrons per nucleon, ρ the matter density and m_N the mass of the nucleon.

In ordinary matter, there are only electrons, protons and neutrons the neutrinos can scatter of. Therefore, charge current elastic forward scattering is only relevant for electron neutrinos. Neutral current elastic forward scattering on the contrary occurs to all neutrino flavours. The corresponding potential in electrically neutral matter is given by the elastic forward neutrino-neutron scattering only, because the

contributions from electrons and protons cancel each other. The derivation is similar to the CC matter potential and yields [11]:

$$V_{\mathrm{NC}} = -\frac{G_F}{\sqrt{2}} N_n. \tag{2.26}$$

Here N_n is the number density of neutrons. For anti-neutrinos the matter potentials V_{CC} and V_{NC} get an additional minus sign. The connection to the density is $N_n = (1 - Y_e) \cdot \rho / m_N$.

However, for standard neutrino oscillations the NC potential drops out of the calculation of the oscillation probabilities: V_{NC} is the same for muon, electron and tauon neutrinos. Therefore, the corresponding contribution to the effective Hamiltonian in flavour space is proportional to the unit matrix and thus let the oscillation probabilities unchanged.

2.3.2 The MSW effect

In the two flavour approximation the effective Hamiltonian in flavour space is given by

$$H_{\mathrm{eff}}^{\mathrm{flavour}} = \frac{1}{2E} U \begin{pmatrix} 0 & 0 \\ 0 & \Delta m^2 \end{pmatrix} U^\dagger + \begin{pmatrix} V_{\mathrm{CC}}(t) & 0 \\ 0 & 0 \end{pmatrix} \tag{2.27}$$

with $U = \begin{pmatrix} \cos\theta_0 & \sin\theta_0 \\ -\sin\theta_0 & \cos\theta_0 \end{pmatrix}$ and θ_0 being the mixing angle in vacuum. The neutrino mixing in matter can now be calculated from the neutrino evolution equation [11]

$$\begin{aligned} i\frac{d}{dt}\begin{pmatrix} \nu_e \\ \nu_\mu \end{pmatrix} &= H_{\mathrm{eff}}^{\mathrm{flavour}} \begin{pmatrix} \nu_e \\ \nu_\mu \end{pmatrix} \\ &= \begin{pmatrix} -\frac{\Delta m^2}{4E}\cos 2\theta_0 + V_{\mathrm{CC}}(t) & \frac{\Delta m^2}{4E}\sin 2\theta_0 \\ \frac{\Delta m^2}{4E}\sin 2\theta_0 & \frac{\Delta m^2}{4E}\cos 2\theta_0 \end{pmatrix} \begin{pmatrix} \nu_e \\ \nu_\mu \end{pmatrix}. \end{aligned} \tag{2.28}$$

The potential V_{CC} is proportional to the number density of electrons N_e and therefore in general time dependent. To simplify the discussion let us assume that N_e is constant. In this case one can introduce the effective mixing angle in matter θ, given as

$$\tan 2\theta = \frac{\sin 2\theta_0}{\cos 2\theta_0 - \frac{2EV_{\mathrm{CC}}}{\Delta m^2}} \tag{2.29}$$

and diagonalize $H_{\text{eff}}^{\text{flavour}}$ corresponding to a basis change from flavour to *matter* eigenstates, which for $V_{\text{CC}} \neq 0$ do not coincide with *mass* eigenstates. The oscillation probability is then calculated as in equation 2.21 with the only difference that the mixing angle is now the mixing angle in matter and the difference of the eigenvalues of the Hamiltonian (which in vacuum was $\frac{\Delta m^2_{21}}{2E}$) is now replaced by those in matter:

$$\lambda_1 - \lambda_2 = \sqrt{\left(\frac{\Delta m^2}{2E}\cos 2\theta_0 - V_{\text{CC}}\right)^2 + \left(\frac{\Delta m^2}{2E}\right)^2 \sin^2 2\theta_0}. \tag{2.30}$$

Finally this leads to the two flavour transition probability in matter

$$P_{\nu_e \to \nu_\mu} = \sin^2 2\theta \sin^2\left(\frac{L}{2(\lambda_1 - \lambda_2)}\right), \tag{2.31}$$

where the oscillation amplitude is given by

$$\sin^2 2\theta = \frac{\sin^2 2\theta_0}{\left(\cos 2\theta_0 - \frac{2EV_{\text{CC}}}{\Delta m^2}\right)^2 + \sin^2 2\theta_0} \tag{2.32}$$

being maximal when the, so called, MSW resonance condition $V_{\text{CC}} = V_{\text{res}}$ is fulfilled. In the simple two flavour case the resonance position is given by

$$V_{\text{res}} := \frac{\Delta m^2}{2E}\cos 2\theta_0. \tag{2.33}$$

Chapter 3

Phenomenology of neutrino oscillations – current status

Today neutrino physics is a quite established research field with numerous experiments, which have been accomplished in the past, being carried out at the moment and are planned for the future. In this chapter, the intension is to describe the present phenomenological status in view of the neutrino oscillation parameters, especially within the standard picture of three neutrino flavour oscillations. We do not give a complete review of all relevant experiments or the implications of their results. In addition some tensions, which at present could not be resolved within this picture, are presented. For more details about the historical development of the phenomenology of neutrino oscillations, see e.g. references [11, 16, 17, 18, 19].

3.1 Solar neutrino oscillations

Thermonuclear fusion reactions in the interior of the sun are responsible for a high solar neutrino flux of $6 \cdot 10^{10}\mathrm{cm}^{-2}\mathrm{s}^{-1}$ at the earth. The processes involved in this reactions can be summarized into two production chains, the *pp* chain and the carbon-nitrogen-oxygen (CNO) cycle. However, neutrinos emitted in the CNO cycle are not expected to be important for neutrino oscillation experiments, since it is responsible for less than 2% of the solar energy. Both chains result in the net reaction [11, 19]:

$$4p + 2e^- \rightarrow {}^4\mathrm{He} + 2\nu_e + 26.73\,\mathrm{MeV}. \tag{3.1}$$

During these fusion processes neutrinos are produced via beta decays and electron capture reactions. Therefore, only electron neutrinos are produced in the sun. The

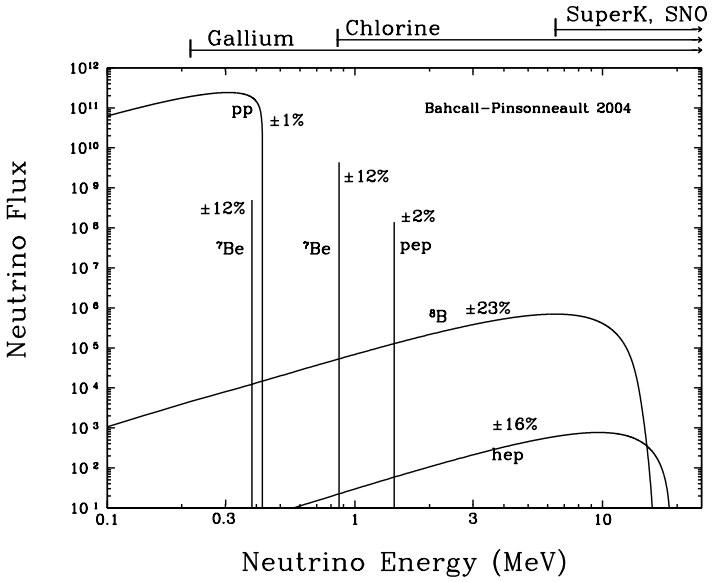

Figure 3.1: The solar neutrino energy spectrum for processes in the *pp* chain. The percentages correspond to uncertainties for each neutrino flux contribution. The energy ranges from solar neutrino oscillation experiments using Gallium and Chlorine as well as scintillator experiments Super-Kamiokande and SNO are shown at the top. Figure taken from [21].

energies of the emitted neutrinos depend on the specific underlying production process and have been calculated in various solar models. Figure 3.1 shows the neutrino energy spectrum for the different contributions of solar neutrino production according to the solar model BS'05 (OP) [20]. The energy range of solar neutrinos starts at below 0.1 MeV and reaches maximal values at approximately 11 MeV.

3.1.1 The solar neutrino problem and its solution

The first measurement of solar neutrinos was made by the Homestake experiment [22] over the period 1970 to 1994. It is located in the Homestake Gold Mine in South Dakota, USA, 1.5 km underground in order to reduce the background mainly caused by muons produced in cosmic rays. The Homestake detector consists of a tank containing 615 tons of tetrachlorethylene (C_2Cl_4). As detection reaction the experiment uses the inverse beta decay of the ^{37}Cl Chlorine isotope induced by an

incoming electron neutrino:

$$\nu_e + {}^{37}\mathrm{Cl} \rightarrow {}^{37}\mathrm{Ar}^{+} + e^{-} \tag{3.2}$$

with the neutrino energy treshold of 0.814 MeV. The produced ^{37}Ar atoms can be extracted and counted by chemical methods to deduce the electron neutrino flux and in this way test the predictions of solar models. Their final result for the measured neutrino flux is one third of the predicted one deviating by more than 3σ [16, 22]. This discrepancy is called the Solar neutrino problem.

Also the Gallium experiments, GALLEX/GNO (GALLium EXperiment/Gallium Neutrino Observatory) [23, 24] and SAGE (Soviet-American Gallium Experiment) [25], which came up in the 1990s detected less neutrinos than expected. These experiments used Gallium to measure solar electron neutrinos using the inverse beta decay reaction

$$\nu_e + {}^{71}\mathrm{Ga} \rightarrow {}^{71}\mathrm{Ge} + e^{-}, \tag{3.3}$$

extracted and counted the produced ^{71}Ge atoms. The neutrino energy treshold of 0.233 MeV is lower than for the Chlorine experiment and thus allows to measure also the low energetic neutrino flux coming from the *pp* reaction, which has the largest neutrino flux contribution of all *pp* chain processes (see figure 3.1). Their results indicate an even more distinct tension with respect to the solar model with about 5σ deviation, measuring only half of the predicted neutrino flux [16, 23, 24, 25].

An other experiment, the Kamioka Nucleon Decay Experiment (Kamiokande) [26], was built 1983 in the Kamioka mine in Japan for the original purpose of measuring nucleon decays. They used a water Cherenkov detector, consisting of a 1 kton water tank surrounded by 1000 photomultipliers (PMTs). In this setting one is able to measure solar neutrinos via elastic scattering with electrons by detecting the Cherenkov light emitted by the recoiling relativistic electrons propagating in water. The advantage over radiochemical experiments is the ability to reconstruct the interaction vertex, the direction and energy of the recoil electron. In this sense Kamiokande was the first experiment measuring solar neutrinos in real-time. With the no-oscillation assumption their results also lead to the conclusion, that the solar model predictions are higher than the actual observed neutrino fluxes. These results agree with the outcome of the first phase of Super-Kamiokande [27], an follow-up precision experiment to Kamiokande and also located in the Kamioka mine, Japan, with larger detector dimensions (50 kton water and a factor 10 more PMTs). Both experiments measured half as much events than expected, deviating from standard solar models by 2σ

[16, 26, 27].

In the year 2001 all current solar neutrino experiments indicate that there has to be a problem either in the detection processes, the solar or the particle physics model. However, as discussed in detail in [11] it is very unlikely that the solar neutrino problem is due to wrong solar model predictions, because if one assumes the solar neutrino spectra to be undistorted, the experimental results are in conflict with each other, independent of the underlying solar model.

The break through was achieved the SNO (Sudbury Neutrino Observatory) experiment [28], located in the Creighton mine, near Sudbury in Canada. The detector consists of 1 kton heavy water and is able to measure not only the electron flux, but also the total flux of all three flavours by three different reactions, electron capture (ES), charge current (CC) and neutral current (NC) reactions

$$\text{ES:} \quad \nu_{e,\mu,\tau} + e^- \rightarrow \nu_{e,\mu,\tau} + e^- \tag{3.4}$$

$$\text{CC:} \quad \nu_e + d \rightarrow e^- + p + p \tag{3.5}$$

$$\text{NC:} \quad \nu_{e,\mu,\tau} + d \rightarrow \nu_{e,\mu,\tau} + n + p. \tag{3.6}$$

The resulting electrons and subsequent-electrons (in the NC reaction, the neutron is absorbed by deuterium or by $MgCl_2$ under emission of a photon, which in turn Compton scatters with electrons) respectively are detected by their emission of Cherenkov light with the help of almost 9500 PMTs. The SNO experiment was accomplished in three phases, where in the second phase $NaCl$ have been added to improve the neutron absorption cross-section and in the third phase this has been further improved by additional ^{3}He counter tubes. Already the results of the first and second phase favoured the flavour oscillation hypothesis [16, 29, 30, 31]. This evidence became stronger after the third phase [32]. The sensitivity to neutrino flavour transitions is given by the relation of the three measurement channels and the results clearly indicates neutrino flavour transitions as the solution to the solar neutrino problem. The charge current neutrino flux Φ_{CC} corresponds to incoming electron neutrinos, the measured neutral current flux Φ_{NC} to the sum of electron, muon and tauon neutrinos and the flux measured in the electron scattering channel Φ_{ES} corresponds to the flux combination $\Phi_{\nu_e} + 0.1553 \cdot \Phi_{\nu_e,\nu_\mu}$ [16]. The measured fluxes are [32]:

$$\Phi_{\text{CC}} = 1.67^{+0.05}_{-0.04}(\text{stat})^{+0.07}_{-0.08}(\text{syst}) \cdot 10^6\,\text{cm}^{-3}\text{s}^{-1} \tag{3.7}$$

$$\Phi_{\text{ES}} = 1.77^{+0.24}_{-0.21}(\text{stat})^{+0.09}_{-0.10}(\text{syst}) \cdot 10^6\,\text{cm}^{-3}\text{s}^{-1} \tag{3.8}$$

$$\Phi_{\text{NC}} = 5.54^{+0.33}_{-0.31}(\text{stat})^{+0.36}_{-0.34}(\text{syst}) \cdot 10^6\,\text{cm}^{-3}\text{s}^{-1} \tag{3.9}$$

yielding a ratio $\Phi_{CC}/\Phi_{NC} = 0.301 \pm 0.033$ [32]. This implies that a fraction of about 69.1% of the originally electron neutrinos are converted to muon and tauon neutrinos before reaching the earth. The no oscillation assumption would expect the same flux for the charge current and neutral current reactions and is thus excluded at a large confidence level, if one assumes the underlying model for the computation of the ^{8}Be spectrum to be correct. It turned out that the data is compatible with a mixing angle of $\tan^2\theta_{12} = 0.447$ and a mass difference of $\Delta m^2_{21} = 4.57 \cdot 10^{-5}\,\mathrm{eV}^2$, which is a result of the SNO best fit for the data of all three phases[1]. It is important to note that for this mixing parameters the solar neutrino transition probability is affected by the MSW effect as discussed in section 2.3.2, because in this case the resonance density becomes

$$V_{\mathrm{res}} = \frac{\Delta m^2_{21}}{2E}\cos 2\theta_{12} = \frac{8.73 \cdot 10^{-12}\,\mathrm{eV}}{E/\mathrm{MeV}} = \frac{1.11 \cdot V_{\mathrm{CC,\,sun}}}{E/\mathrm{MeV}}. \tag{3.10}$$

Hence, for the SNO relevant energy range (see figure 3.1) V_{res} is slightly above the charge current matter potential evaluated at the center of the sun $V_{\mathrm{CC,\,sun}}$ and thus it is possible for electron neutrinos produced by ^{8}Be decays with energies $E \geq 1.11\,\mathrm{MeV}$ to pass the resonant density inside the sun. This leads to resonantly enhanced flavour transitions such that it becomes compatible with the 30.1% electron disappearance measured by SNO.

3.1.2 The Gallium Anomaly

Although the results of the GALLEX and SAGE solar neutrino oscillation experiments confirmed the solar oscillation parameters as already described above, both experiments performed cross checks with intense radioactive sources (GALLEX: using a ^{51}Cr source [33, 34, 35]; SAGE: using a ^{51}Cr source [36, 37] and later also a ^{37}Ar source [38, 39]; both sources are ν_e emitter) measuring significant lower neutrino fluxes than expected. The average ratio of the measured and predicted neutrino fluxes for these radioactive source experiments deviates with about 3σ from unity. This is called the *Gallium Anomaly*. It is still unclear if this anomaly is due to yet unknown systematic errors in the experiments or can be interpreted as a hint towards new physics, such as an additional sterile neutrino. Assuming that this effect is caused by sterile-active neutrino mixing, Giunti and Laveder performed a χ^2 analysis in [40] for

[1] In the corresponding SNO analysis also included: the measurement of the day-night asymmetry, which is due to the matter effect of the neutrinos inside the earth. For a discussion of this so called *regeneration in the earth* effect, see e.g. [11, 16].

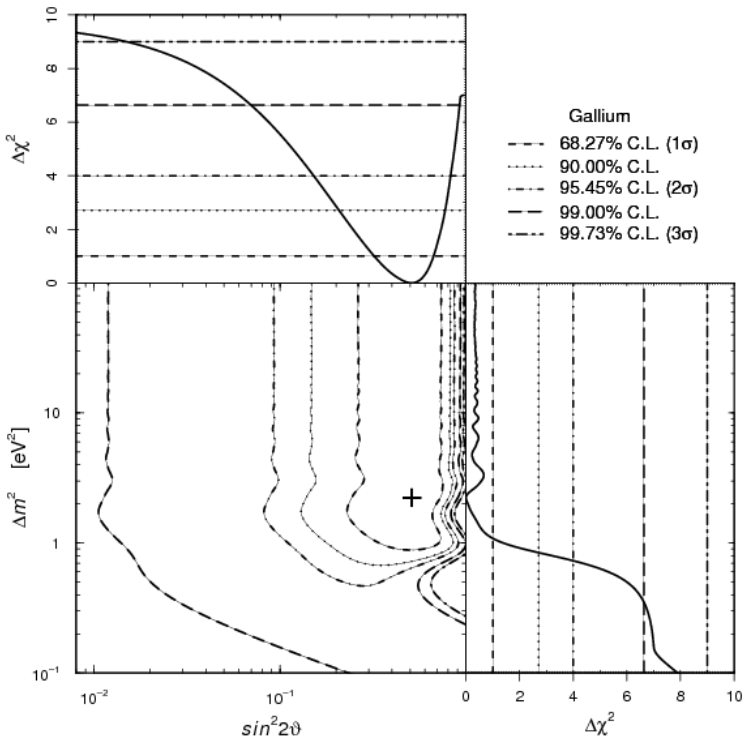

Figure 3.2: The figure shows contours of constant $\chi^2 - \chi^2_{\text{min}}$ differences corresponding to specific confidence levels for the two flavour neutrino oscillation fit performed by Giunti and Laveder with the data sets of the Gallium radioactive source experiments performed in GALLEX and SAGE. The best fit point is indicated with a cross and corresponds to $\sin^2 2\theta = 0.5$ and $\Delta m^2 = 2.24\,\text{eV}^2$. Figure taken from [40].

the GALLEX and SAGE data sets. They found best fit values preferring oscillation parameter values of $\sin^2 2\theta \gtrsim 0.07$ and $\Delta m^2 \gtrsim 0.35\,\text{eV}^2$ at 99% confidence level.

3.2 Atmospheric neutrino oscillations

Cosmic ray particles are mainly composed of protons and a small component of heavier nuclei. When hitting the atmosphere they interact with atoms and induce hadronic showers. Among other particles also pions and kaons are produced, which both can decay into muons, electrons and muon and electron neutrinos according to the reac-

tions [11, 16]:

$$\pi^{\pm}(K^{\pm}) \rightarrow \mu^{\pm} + \nu_{\mu}(\overline{\nu}_{\mu}), \tag{3.11}$$

$$\mu^{\pm} \rightarrow e^{\pm} + \nu_{e}(\overline{\nu}_{e}) + \overline{\nu}_{\mu}(\nu_{\mu}). \tag{3.12}$$

These atmospheric neutrinos are produced in a large energy range. Typical atmospheric neutrino experiments are sensitive to neutrino energies from about 100 MeV to about 100 GeV. They can be detected via the interaction with nuclei A of large mass according to the reactions [11, 16]:

$$\nu_{e}(\overline{\nu}_{e}) + A \rightarrow e^{-}(e^{+}) + X, \tag{3.13}$$

$$\nu_{\mu}(\overline{\nu}_{\mu}) + A \rightarrow \mu^{-}(\mu^{+}) + X. \tag{3.14}$$

Note that the amount of produced muon neutrinos is larger than the number of produced electron neurinos. This ratio of the muon and electron neutrino rate is energy dependent and can be calculated using Monte Carlo simulations. These calculations suffer from large uncertainties. Thus, it is convenient to use the ratio $R = (\nu_{\mu} + \overline{\nu}_{\mu})/(\nu_{e} + \overline{\nu}_{e})$ (where large uncertainties are canceled out) in order to compare the Monte Carlo predictions with measurements [11, 16].

The first experiments, which measured atmospheric neutrino fluxes with their results hinting at a possible neutrino oscillation, were IMB (Irvine-Michigan-Brookhaven) and Kamiokande. The latter measured a deficit in the atmospheric neutrino flux for sub-GeV events (fully contained events of visible energy < 1.33 GeV) as well as for multi-GeV events (fully contained events of visible energy > 1.33 GeV) of [16, 41, 42]:

$$\left.\frac{R_{\mathrm{MC}}}{R_{\mathrm{exp}}}\right|_{\text{sub-GeV}} = 0.60^{+0.07}_{-0.06} \pm 0.05 \tag{3.15}$$

$$\left.\frac{R_{\mathrm{MC}}}{R_{\mathrm{exp}}}\right|_{\text{multi-GeV}} = 0.57^{+0.08}_{-0.07} \pm 0.07, \tag{3.16}$$

where R_{MC} refers to the Monte Carlo prediction and R_{exp} to the measured muon-electron event ratio. Also the zenith-angle distribution of the upward-going muons provided hints for neutrino oscillations [16, 43].

The IMB experiment used (like Kamiokande) a water Cherenkov detector with 8 kton water. It was located in the Morton Thiokol salt mine in Ohio deep under ground in order to shield against the cosmic muons. As for the Kamiokande experiment the original intension was to measure nucleon decays. Their background

analysis including atmospheric neutrino events resulted in a deficit of muon neutrinos for contained vertex events[2] of energies below 1.5 GeV [44, 45]. For only partially contained events as well as the upward-going muon events, no deficit was measured [46, 47]. Quantitatively the measured deficit was $R_{\mathrm{MC}}/R_{\mathrm{exp}} = 0.54 \pm 0.05 \pm 0.11$ [16, 45]. This result is consistent with the Kamiokande results and served as an additional hint towards atmospheric neutrino oscillations, although the global picture of neutrino oscillations at that time was not clear at all[48].

The results of the Kamiokande follow-up experiment Super-Kamiokande solved this puzzle. The increased sensitivity in the directional measurement of atmospheric neutrino events led them to measure an significant asymmetry between upward-going and downward-going high-energy ν_μ events. For those high-energy events the effect of the gyromagnetic field of the earth is reduced. Therefore, assuming that no oscillation occurs one would expect an almost uniform distribution of the high-energy atmospheric neutrino events. The asymmetry parameter is given by the ratio $A = (U - D)/(U + D)$, where U = upward-going events and D = downward-going events. Super-Kamiokande measured muon and electron neutrino asymmetries of [49]

$$A_{\nu_\mu} = -0296 \pm 0.048 \pm 0.01 \tag{3.17}$$

$$A_{\nu_e} = -0.036 \pm 0.067 \pm 0.02. \tag{3.18}$$

Since ν_e events show no deficit, but the ν_μ events deviate with 6σ from the no oscillation prediction, this result strongly favours a $\nu_\mu \to \nu_\tau$ neutrino oscillation solution of the atmospheric neutrino anomaly indicating that muon neutrinos passing through the earth oscillate on their way towards the detector. In contrary, the path length for neutrinos coming from the opposite direction is too small for a neutrino transition of downward-going ν_μ. The deficit is observed for energies $L/E \gtrsim 10^2\,\mathrm{km\,GeV^{-1}}$ indicating a corresponding atmospheric mass squared difference of the order $\Delta m^2_{23} \approx 2.4 \cdot 10^{-3}\,\mathrm{eV}^2$ with a mixing angle of $\theta_{23} > 0.82$ at 90% confidence level. Also more detailed analysis of the L/E dependence and the ν_μ event zenith angle distribution supports this interpretation [11, 16, 49] (see section 3.4 for a discussion of the current experimental results in the context of a global analysis).

At this point, there are two more experiments to mention, which confirmed the atmospheric neutrino oscillation picture independently: The Soudan 2 experiment, located in the Soudan underground Mine State Park, Minnesota, and the MACRO

[2] Contained vertex events are events, where the neutrino interaction with matter happens inside the detector and the trajectories of all involved particles are contained in the detector.

experiment (Monopole Astrophysics and Cosmic Ray Observatory), located in the Laboratoi Nazionali del Gran Sasso, Italy. Soudan 2 consisted of a time projection, tracking calorimeter out of iron with a total mass of 963 tons. Their results for the ratio $R_{\mathrm{MC}}/R_{\mathrm{exp}}$ as well as the zenith angle distribution of contained events and upward-going muons reported in [50, 51] are fully consistent with those obtained by Super-Kamiokande [16]. MACRO was a multiple-purpose experiment and consisted of a $12 \times 76 \times 9.4\,\mathrm{m}^3$ large detector containing 600 tons of liquid scintillator. Their analysis of the atmospheric neutrino data gave a further confirmation for the $\nu_\mu \to \nu_\tau$ oscillation [16, 52, 53].

3.3 Terrestrial neutrino oscillations

Terrestrial neutrino oscillation experiments use two types of neutrino sources: electron anti-neutrinos emitted by nuclear reactors and accelerator experiments, where neutrinos are produced in the decays of pions, kaons and muons originating from a primary proton beam hitting a target. In the following we will give an overview over some of these experiments, which are the most relevant for the current status of three flavour neutrino oscillations. In addition the short-baseline (SBL) anomaly and the reactor anomaly is presented.

3.3.1 Reactor experiments

Reactor experiments measure the electron anti-neutrino flux resulting from the chain of β-decays of the fission products. The anti-neutrinos are produced at a very high rate and with energies of a few MeV. Since the neutrino emission is isotropic the flux decreases rapidly with increasing distance, most reactor experiments have detectors with short baselines of $L \sim 10 - 100\,\mathrm{m}$. The results of these SBL reactor experiments are used to test the complicated theoretical neutrino flux predictions and thus yields a reduction in the uncertainty for reactor experiments with long baselines. The detectors of such experiments are typically large liquid scintillators and use the detection reaction [16]

$$\overline{\nu}_e + p \to n + e^+. \tag{3.19}$$

The positron annihilates with a surrounding electron and deposits energy in the scintillator. The signal-background discrimination is achieved by a coincident neutron inducing a delayed nuclear capture reaction. The neutrino threshold energy in this

reaction is calculated, e.g. in [16]: $E_{\text{th}} = 1.8\,\text{MeV}$. In order to further improve the signal to background ratio it is important to shield the detector from cosmic ray showers. In contrast to atmospheric and solar neutrino detectors the $\overline{\nu}_e$ flux is much larger and thus it is sufficient to reduce the background below the $\overline{\nu}_e$ flux, i.e. the detectors does not necessarily have to be located as deep underground as solar and atmospheric neutrino experiments. For a more detailed discussion of the reactor experiments see reference [16].

There have been numerous SBL reactor experiments setting limits on neutrino oscillations at low mass squared differences $\Delta m^2 \sim 0.1\,\text{eV}^2$ like for example [11, 16]: ILL [54], Gosgen [55], Rovno [56], Krasnoyarsk [57], Bugey [58] and Savannah River [59], but here we want to focus on those experiments, which dominate the current knowledge about the values of the three flavour oscillation parameters obtained from global fits like in [60], see section 3.4.

The long baseline (LBL) reactor experiments CHOOZ and Palo Verde are located at distances of the order 1 km away from the reactors and are thus sensitive to lower Δm^2 values. CHOOZ, located near to the two reactors of the CHOOZ power stations in France, measured the background very accurately, because the data taking started before the reactor was put into operation. Their results set limits on the $\overline{\nu}_e$ oscillation essentially excluding the possibility that the atmospheric mixing is due to $\nu_\mu \to \nu_e$ oscillation [16, 61]. Additionally, the limit on the at this time unknown mixing angle θ_{13} could be further improved [62]. The experiment Palo Verde, located near to the three reactors of the Palo Verde Nuclear Generation Station in Arizona, confirmed the results of CHOOZ [16, 63].

At that time the neutrino oscillation picture of three flavour oscillations was established and well founded on various experimental results, but there were (and still are) some open questions. For example, the question about the size of θ_{13} was very important for completing the knowledge about neutrino oscillations. If θ_{13} would be zero, this would imply that the CP-phase δ in equation 2.23 is eliminated and would lead to a drastically simplified oscillation picture. Also the possible measurement of the mass hierarchy is affected from the size of θ_{13}. In order to obtain a better sensitivity to the mixing angle θ_{13} a new generation of $\overline{\nu}_e$ disappearance experiments had been developed. The basic idea of these new experiments is that each of them consists out of two almost identical detectors of different distances to the reactor. This leads to a significant reduction of the total flux uncertainty, since systematic uncertainties cancel out. With this purpose the experiments Double-Chooz, Daya Bay and Reno have been build. The first results from Double-CHOOZ (with only the far detector

running) [64] already indicated a non-zero θ_{13} value. Double-CHOOZ is located at the same place as the former CHOOZ experiment near to the two reactors of the CHOOZ power stations in France. The distance from the power plant to the near and far detector respectively is about 100 m and 1 km. In this setting the ratio L/E is such that Double-CHOOZ is sensitive to anti-neutrino oscillations of the form [64]

$$P_{\overline{\nu}_e \to \overline{\nu}_e} \approx 1 - \sin^2 2\theta_{13} \sin^2 \left(\frac{\Delta m^2_{31}}{4E} L \right). \tag{3.20}$$

With the same purpose, two other experiments were constructed: Daya Bay, located near to three reactors of the Daya Bay nuclear power complex in the southern coast of China [65], and RENO (Reactor Experiment for Neutrino Oscillation), located near to six reactors of the Yonggwang nuclear power plant at the west coast of South Korea [66]. The first results published in 2012 by these two experiments were based on a rate-only analysis, i.e. without a more detailed examination of the energy shape of the electron anti-neutrinos. Daya Bay reported in [67] a value for $\sin^2 2\theta_{13}$ of $0.092 \pm 0.016(\text{stat}) \pm 0.005(\text{syst})$ with a 5.2σ evidence for the mixing angle to be non-zero. RENO published a compatible result for the mixing angle of $\sin^2 2\theta_{13} = 0.113 \pm 0.013(\text{stat}) \pm 0.019(\text{syst})$ (corresponding to a 4.9σ evidence) [68]. A further confirmation came from the Double-CHOOZ collaboration. They presented an analysis using the neutron capture on hydrogen for the detection of the neutrino events [69] in addition to the usual signal induced by neutron capture on Gadolinium. This could only be done, because of the low background (and a good knowledge of the background[3]) in their detector. This measurement yielded the value $\sin^2 2\theta_{13} = 0.097 \pm 0.034(\text{stat}) \pm 0.034(\text{syst})$ (corresponding to 2.0σ evidence), which is in full agreement with their previous result (using the neutron capture on Gadolinium) of $\sin^2 2\theta_{13} = 0.109 \pm 0.030(\text{stat}) \pm 0.025(\text{syst})$ (corresponding to 2.9σ evidence) [70]. Note that in the Double-CHOOZ analysis also the energy shape information had been included. It can be expected that the results of these three experiments will improve during the next periods of data taking.

All reactor experiments discussed until this point have in common that they are build to measure the electron anti-neutrino flux of one power plant. There is one other reactor experiment being able to measure $\overline{\nu}_e$ at very long baselines: KamLAND (KAMioka Liquid scintillator Antineutrino Detector) [71], located at the site of the earlier Kamiokande experiment, consists out of a very large detector with 1 kton liquid scintillator. In this setting KamLAND detects $\overline{\nu}_e$ from all power reactors in

[3] This is one essential advantage of Double-CHOOZ compared to RENO and Daya Bay.

Japan and some contributions from even more distant reactors (about 3% of the $\overline{\nu}_e$ flux). The average distance is about 180 km. Therefore, KamLAND is sensitive on the parameter range of solar neutrino oscillations. Their result confirmed the solar neutrino oscillations[4] and is still important for the precise determination of the oscillation parameters. While the solar experiments have better sensitivity on the mixing angle the contribution of KamLAND increases the precision on the mass squared difference in global fits, what can be seen e.g. in the more recent publication [72].

3.3.2 The reactor neutrino anomaly

A recent recalculation [73] of the electron anti-neutrino flux emitted from nuclear rectors leads to a reduction of about 3% of the previously calculated flux prediction at SBL neutrino reactor experiments. With this correction, the average of the in SBL reactor experiments [54, 55, 56, 57, 58, 59] measured ratio of observed and predicted $\overline{\nu}_\mu$ event rates is now shifted from previously 0.976 ± 0.024 to 0.943 ± 0.023. As indicated in figure 3.3, one possible solution of this anomaly is neutrino oscillation with a relatively large mass squared difference of the order $\Delta m^2 \sim \text{eV}^2$. This would require the introduction of a new neutrino[5], which mixes with the active neutrinos via oscillation.

In September 2013, Hayes, Friar, Garvey and Jonkmans published in [75] a reanalysis of the reactor anomaly, where they claimed that the 30% of the total reactor electron anti-neutrino flux coming from forbidden decays would introduce a large uncertainty into the predicted flux such that the effect of the reactor anomaly would be smaller than the uncertainty of the flux prediction.

However, this anomaly motivates a further investigation of the possibility for introducing a sterile neutrino. On the experimental side, the upcoming NUCIFER (Reactor neutrino detection for thermal power measurement and non-proliferation purpose) experiment has the potential to check if there are some yet undiscovered $\overline{\nu}_e$ oscillation at very short reactor-detector distances, see e.g. reference [76] for more details.

[4] Especially the so called *large mixing angle* (LMA) solution could be confirmed. Other possible solutions, where the solar mixing parameters have different values, have been excluded by the KamLAND results. For a more detailed discussion about these parameter regions, see e.g. [11, 16].

[5] Such a new neutrino state should be sterile, i.e. non-weakly interacting, because of the constraints coming from the precise measurement of the Z width in LEP (Large Electron-Positron Collider) [74].

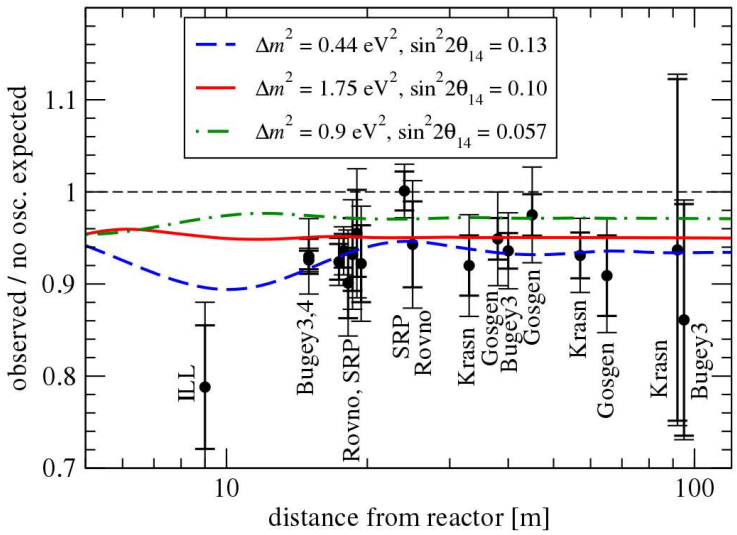

Figure 3.3: The figure shows the ratio of the observed and predicted $\overline{\nu}_\mu$ event rates measured by various SBL reactor experiments at different baselines. The black dashed line corresponds to the oscillation prediction in the standard three flavour scenario (which predicts no oscillation at such short baselines). The blue, red and green lines are computed for active-sterile mixing for three parameter sets, which give a better explanation for the $\sim 6\%$ flux deficit. Figure taken from [6].

3.3.3 Accelerator experiments

Accelerator experiments use proton beams produced in particle accelerators that are focused on a high-mass target. Out of these proton-target collisions (anti-)neutrinos are emitted mostly as a product of hadronic decays. Many experiments have been performed in the past searching for oscillations with baselines of the order $L/E \lesssim$ km/GeV (called SBL accelerator experiments) corresponding to the sensitivity for mass squared differences of $\Delta m^2 \gtrsim 1\,\mathrm{eV}^2$. None of these experiments found evidence for neutrino oscillation, what sets limits in the $\sin^2\theta$ - Δm^2 plane for different oscillation channels. Only the LSND (Liquid Scintillator Neutrino Detector) as well as later the MiniBooNE (Booster Neutrino Experiment) experiment observed an indication of a positive oscillation signal. This is called the SBL anomaly (as discussed in the next section) [16].

Accelerator experiments with long baselines (LBL) on the contrary, have observed oscillation effects. The beam energy and source-detector distance is chosen such that the sensitivity for the atmospheric mass squared difference is achieved, i.e. $L/E \sim 10^3$ km/GeV. K2K (KEK to Kamioka) [77] was the first of these type of experiments. It used a 12 GeV proton beam from the proton synchrotron at KEK, which is located in Tsukuba in Japan. The proton beam hits an aluminium target producing pions, which are focused towards a decay tunnel of 200 m length. This tunnel ends with a beam dump and is followed after a distance of 80 m by a near detector. The pions decay into muon neutrinos which then are detected at the near and far detector. The far detector uses the water Cherenkov detector of Super-Kamiokande at a total distance to the target of 250 km. The near detector is a smaller version of the Super-Kamiokande detector and is used to reduce systematic uncertainties, which cancel out in the comparison of the near and far detector data. Their final result [77] of the ν_μ disappearance measurement gave a 4.3σ evidence in favour of oscillation and is compatible with the atmospheric mixing parameters. This result was a very important confirmation for the atmospheric oscillation signals [16].

An other important experiment is MINOS (Main Injector Neutrino Oscillation Search) [78] using the NuMI (Neutrinos at Main Injector) wide band muon neutrino beam at Fermilab, located near Chicago. It consists of two detectors at baselines of 965 m and 735 km and is thus sensitive to the atmospheric mixing parameters and to θ_{13} depending on the oscillation channel the analysis is referring to (either appearance or disappearance). Similar to KEK, this is achieved with the *decay in flight* method, where either π^+ or π^- are focused towards the decay pipe decaying in ν_μ or $\overline{\nu}_\mu$ respectively. While the disappearance channel ($\nu_\mu, \overline{\nu}_\mu \to \nu_\mu, \overline{\nu}_\mu$) is sensitive to the

atmospheric mixing, the ν_e appearance measurement gives information about θ_{13} at leading order according to equation [79]

$$P_{\nu_e \to \nu_\mu} \approx \sin^2 \theta_{23} \sin^2 2\theta_{13} \sin^2 \left(\frac{\Delta m^2_{32}}{4E} \right). \tag{3.21}$$

If this appearance measurement can be further improved, it is in principle possible to determine the CP-phase δ and the mass hierarchy, see e.g. reference [80] for the subleading terms omitted in the approximation of equation 3.21. Recent results of MINOS give the precise measurement of [81] $\sin^2 2\theta_{23} = 0.957^{+0.035}_{-0.036}$, $|\Delta m^2_{31}| = 2.39^{+0.09}_{-0.10} \cdot 10^{-3}\,\mathrm{eV}^2$ and sets a limit $0.01(0.03) < 2\sin^2\theta_{23}\sin^2 2\theta_{13} < 0.12(0.19)$ at 90% confidence level assuming the CP-phase δ to be zero for normal (inverted) mass hierarchy. The latter result was a confirmation of the previously reported first measurement of θ_{13} in a $\nu_\mu \to \nu_e$ appearance measurement by T2K [82].

The T2K (Tokai to Kamioka) experiment [82] uses like the earlier K2K experiment the large Super-Kamiokande detector as their far detector. The neutrino production method is similar to those of MINOS and K2K with the main difference that they use an off-axis beam (the far detector is located at an angle of 2.5 degrees with respect to the beam axis), which amplifies the signal to background ratio for the detection of ν_e neutrinos in the ν_μ beam. T2K uses two near detectors, one of them located on-axis and one off-axis in order to measure the neutrino spectrum accurately as well as to have a reference measurement for the flux prediction at the far detector. Very recently (November 2013) they published in [82] an updated result of $\sin^2 2\theta_{13} = 0.140^{+0.038}_{-0.032}$ for normal and $\sin^2 2\theta_{13} = 0.170^{+0.045}_{-0.037}$ for the inverted hierarchy (under the assumption of $|\Delta m^2_{32}| = 2.4 \cdot 10^{-3}\,\mathrm{eV}^2$, $\sin^2\theta_{23} = 0.5$ and $\delta = 0$).

3.3.4 The short-baseline anomaly

The LSND (Liquid Scintillator Neutrino Detector) experiment [83] was a SBL accelerator experiment designed to search for $\overline{\nu}_\mu \to \overline{\nu}_e$ oscillations at a baseline of only 30 m. It was located at the Los Alamos Neutron Science Center in New Mexico. In contrast to the above described accelerator experiments it used a different neutrino production mechanism optimized to measure $\overline{\nu}_e$ appearance in a $\overline{\nu}_\mu$ beam. Protons with 798 MeV hit a water target followed by a Cu beam dump. The proton beam produces a large number of pions, most of them π^+. π^- and μ^- produced in the reaction chain are mainly absorbed. Thus, the resulting neutrino beam consists out

of $\overline{\nu}_\mu$, ν_μ and ν_e created in the reactions

$$\pi^+ \to \mu^+ + \nu_\mu, \tag{3.22}$$

$$\mu^+ \to e^+ + \nu_e + \overline{\nu}_\mu. \tag{3.23}$$

This leads to a very low contamination of $\overline{\nu}_e$ events in the neutrino beam, which increases the sensitivity on $\overline{\nu}_e$ appearance.

LSND reported a positive signal in the $\overline{\nu}_\mu \to \overline{\nu}_\mu$ oscillation channel [84] and later also in the neutrino channel $\nu_\mu \to \nu_\mu$ [85] giving evidence for neutrino oscillation, which can not be explained within the three flavour mixing framework. If explained by neutrino mixing, their combined results would only be compatible with mass squared differences in the range $0.2 - 10\,\mathrm{eV}^2$ [83].

In order to test these results, the MiniBooNE (Booster Neutrino Experiment) experiment [86] was constructed. It is located at Fermilab and uses 8 GeV protons hitting a beryllium target. The produced pions decay inside a 50 m long decay pipe followed by a beam dump. The total distance from target to detector is 541 m and is chosen such that MINOS is sensitive for the same Δm^2 region as the former LSND experiment[6]. Since the energy range as well as the neutrino production mechanism is different, MiniBooNE constitutes an independent test of the LSND signal. Their current result is compatible with LSND and can be explained by two flavour oscillations in the range $0.01\,\mathrm{eV}^2 < \Delta m^2 < 1\,\mathrm{eV}^2$ [87].

Note that although LSND and MiniBooNE are compatible with each other and both favour an active-sterile mixing solution, there are severe tesnions with ν_μ and $\overline{\nu}_\mu$ disappearance searches, even if one includes a sterile neutrino in the analysis [6]. On the other hand, LSND and MiniBooNE are not yet completely excluded by other $\nu_\mu, \overline{\nu}_\mu \to \nu_e, \overline{\nu}_e$ appearance searches as one can see in figure 3.4.

3.4 Global fit to three neutrino mixing

In [60] Gonzalez-Garcia, Maltoni, Salvado and Schwetz presented a global fit to data from solar, atmospheric, reactor and accelerator neutrino oscillation experiments. The parameters in their analysis are those of equation 2.23: θ_{12}, θ_{13}, θ_{23}, δ, Δm^2_{21} and Δm^2_{31}, i.e. assuming three flavor mixing only. Their results are shown in figure 3.5 and are representative for the current status of the standard three flavour pic-

[6] The MiniBooNE neutrinos have typical energies of 500 MeV compared to the LSND energies of about 30 MeV and a baseline of 30 m. Therefore, the same L/E ratio is achieved.

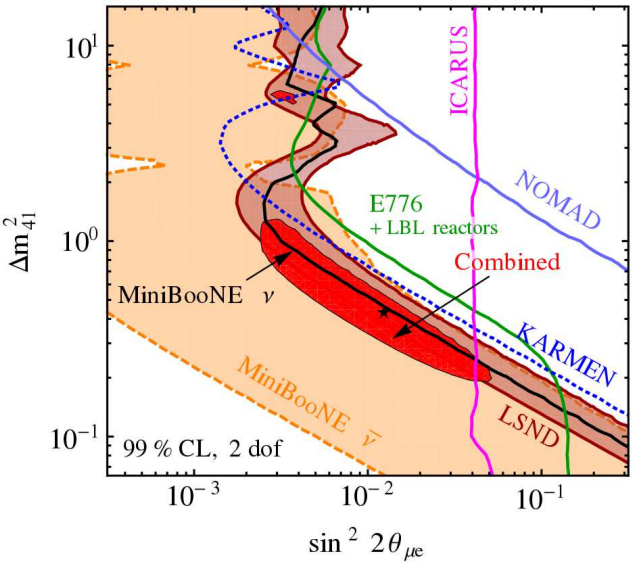

Figure 3.4: The figure shows the allowed regions and upper bounds at 99% confidence level for $\nu_\mu, \overline{\nu}_\mu \to \nu_e, \overline{\nu}_e$ appearance experiments obtained in a three active plus one sterile neutrino framework computed in [6]. As one can see, the LSND and MiniBooNE results are the only ones in favour of an active-sterile oscillations. However, they are not excluded by other accelerator appearance measurements (such as KARMEN [88], ICARUS [89], NOMAD [90], E776 [91]) or LBL reactor experiments. Figure taken from [6].

ture. The first order oscillation terms are precisely measured. This results in the high precision for the atmospheric (θ_{23} and Δm^2_{31}) and solar (θ_{12} and Δm^2_{21}) mixing parameters as a result of the combination of the various atmospheric and solar experiments respectively and from terrestrial experiments such as KamLAND, Super-Kamiokande, MINOS and others (see discussions in previous sections). Even θ_{13} is precisely determined by the most recent LBL reactor and accelerator experiments[7], but there remains an additional uncertainty in θ_{13} due to the normalization of the reactor fluxes, which is still an unsolved problem [60].

For future experiments the remaining questions are the measurement of the mass hierarchy, the CP-phase δ as well as the so called octant degeneracy of the mixing angle θ_{23}, which is due to the fact that in first order the sensitivity on θ_{23} is given by the sine squared of *two* times the mixing angle $\sin^2 2\theta_{23}$. In addition, we have seen that the Gallium anomaly, SBL reactor anomaly and the SBL anomaly give evidence for additional active-sterile mixing. However, these anomalies are in tension with other results, even by introducing one or two sterile neutrinos [6]. In the following chapters, we want to address this problem by investigating a sterile neutrino model as studied e.g. in [8, 9, 7, 10] with non-standard matter interactions with the possibility to resolve the tension obtained in usual sterile neutrino scenarios.

[7] Note that this analysis is from 2012 and thus the precision in figure 3.5 is driven by RENO, Daya Bay and Double-CHOOZ. Including the new results from T2K would further improve the precision on θ_{13}.

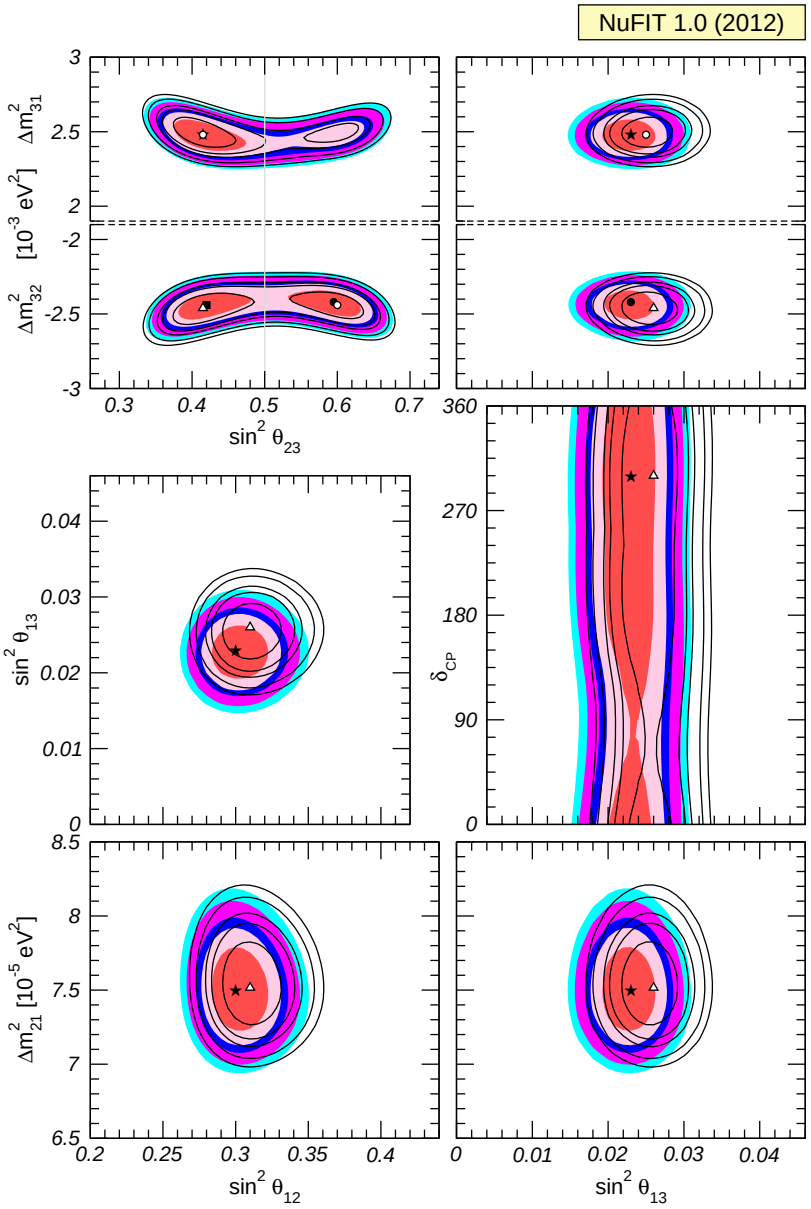

Figure 3.5: Global three flavour oscillation analysis. Each panel shows the $\chi^2 - \chi^2_{\text{min}}$ value as function of two out of in total six parameters, where the other parameters are chosen such that $\chi^2 - \chi^2_{\text{min}}$ becomes minimal. The contours correspond to 1σ, 90%, 2σ, 99% and 3σ confidence level. The coloured regions are calculated including the SBL reactor data with the flux normalization as a fitting parameter. The black contour lines correspond to an analysis without the SBL reactor experiments. The atmospheric mass squared difference Δm^2_{32} is used for inverted mass hierarchy and Δm^2_{31} for normal hierarchy. Figure taken from [60].

Chapter 4

Oscillation probabilities in a sterile baryonic neutrino model

After motivating a model introducing a new *quasi-sterile*[1] neutrino based on the ideas of references [8, 9, 7, 10], we give a short formal description with emphasis on the phenomenology of neutrino oscillation and derive approximate analytical expressions for the oscillation probabilities in order to compare it with the results of [7] and an exact numerical computation.

4.1 Motivation

In the previous chapters we introduced the current established standard scenario of neutrino oscillations and summarized some of the most important experiments in that field. Even though one was able to find values for the oscillation parameters in the slightly extended SM with three massive neutrinos that are consistent with many experimental results, one can also see that there is some tension coming from experimental anomalies, which can not be resolved in this framework. In the following we describe an extension of the SM with the potential to give an explanation not only for these anomalies, but possibly also for some signals observed in current dark matter detection experiments. The basic idea of this model is to introduce an additional $U(1)$ gauge symmetry, under which only quarks and an additional (otherwise sterile, i.e. not weakly interacting) neutrino have a non-zero charge. If the corresponding gauge boson is relatively light (compared to the electro-weak scale), the coupling can be

[1] The neutrino is sterile in the sense that it does not interact via the weak interaction, but in the presented model it couples to baryons. In the following we will refer to it as *sterile*.

large[2] and yield a large matter potential. This in turn can enhance the active-sterile neutrino mixing and lead to new MSW resonances.

This idea was proposed in [8] by Maxim Pospelov with the motivation to find a possible explanation for anomalies found in current dark matter experiments: the annual modulation signal in DAMA [92] and the low-energy recoil signal measured by CoGeNT [93]. He found that for large couplings mediated by the new gauge boson the DAMA and CoGeNT signals could be explained by solar standard model neutrinos which oscillate into the new neutrino state via the MSW effect for the new potential. He also showed that a large baryonic coupling, up to three orders of magnitude larger than the weak coupling, is still allowed by current experimental data.

Karagiorgi, Shaevitz and Conrad investigated in [7] the phenomenological consequences of the same model, but now with respect to the MiniBooNE and LSND short-baseline anomalies. They made an approximate analytical calculation and performed a χ^2 fit to the MiniBooNE neutrino [94], MiniBooNE anti-neutrino [95] and LSND anti-neutrino data [83]. They found that the new model is preferred against the standard scenario, indicating that the new matter effect can serve as a possible solution of the anomalies. They claimed that MINOS is not sensitive to the baryonic neutrino at their LSND/MiniBooNE best fit point, but as we will see in section 4.5, the in their analysis underlying analytical expressions for the oscillation probability are not valid for the whole parameter space of the model. Especially at the MINOS energy range and detector distance the approximation in [7] misleadingly suggests that their LSND/MiniBooNE best fit is compatible with the MINOS data. Therefore, we will reanalyse the MiniBooNE and MINOS data in the model at hand using a full numerical calculation and provide improved analytical approximations. It can further be expected that the new MSW resonances affect the solar neutrino oscillation. To make more conclusive phenomenological statements, it is not avoidable to investigate the constraints coming from solar neutrino oscillation experiments.

4.2 The baryonic neutrino model

The starting point is gauged baryon number, i.e. to introduce a new $U(1)_B$ gauge symmetry under which quarks have the charge $g_b/3$. In addition a new particle is introduced: a new neutrino state ν_b, a singlet under the SM gauge group and with the charge g_b' under the new symmetry $U(1)_B$. Hence, in this framework there exist three SM left-handed neutrinos ν_L^e, ν_L^μ, ν_L^τ, three corresponding right-handed neutrinos N_R^1,

[2] The interesting parameter range for the coupling is $10^2 - 10^3 \cdot G_F$ [8].

N_R^2, N_R^3 and an additional left-handed neutrino ν_L^b. In principle one can also add a right-handed partner for ν_L^b, but this is not important for the following discussions and analysis[3]. We will stick to the most important ingredients of this model and not aim for absolute completeness, since there exist many different possible variants in the details of the model building and we want to focus on the phenomenological consequences.

Assuming a spontaneous symmetry breaking of $U(1)_B$ by a new Higgs field, the relevant part of the Lagrangian can be written as [8]:

$$\begin{aligned}\mathcal{L} &= -\frac{1}{4}\left(\partial_\mu X_\nu - \partial_\mu X_\nu\right)\left(\partial^\mu X^\nu - \partial^\mu X^\nu\right) + \frac{1}{2}m_X^2 X_\mu X^\mu \\ &\quad + \bar{\nu}_b\gamma_\mu\left(i\partial^\mu + g_b' X_\mu\right)\nu_b + \sum_q \bar{q}\left(i\not{\partial}_{\mathrm{SM}} + \frac{1}{3}g_b\gamma_\mu X^\mu\right)q + \mathcal{L}_m\,, \end{aligned} \tag{4.1}$$

where X_μ is the corresponding vector boson of mass m_X, q are the SM quark fields and $\mathcal{L}_m$ is the part of the Lagrangian containing the masses. If we consider the Lagrangian at energies much smaller than m_X, we can write down an effective coupling for fermions in terms of a coupling constant G_B. Since we are interested in the low-energy phenomenology, we can also switch from the quark to the nucleon level. In this way we obtain the neutral current baryonic (NCB) coupling term induced by the vector boson exchange in the low-energy limit [8]:

$$\mathcal{L}_{\mathrm{NCB}} = \frac{G_B}{\sqrt{2}}\bar{\nu}_b\gamma_\mu\left(1-\gamma_5\right)\nu_b\left[\bar{p}\gamma^\mu\left(1-\gamma_5\right)p + \bar{n}\gamma^\mu\left(1-\gamma_5\right)n\right], \tag{4.2}$$

where $G_B = g_b g_b'/m_X^2$ is the baryonic coupling constant.

The matter potentials for the charged current and neutral current weak interactions are derived in section 2.3.1. For the new baryonic interaction this derivation is similar, since the Lagrangian has the same structure as in equation 2.24. The comparison with equation 2.26 yields for the baryonic potential V_b:

$$V_b = -\frac{G_B}{\sqrt{2}}N_n. \tag{4.3}$$

If G_B is some orders of magnitude higher than the Fermi constant G_F, this could lead to observable signals in dark matter detectors induced by solar neutrinos oscillating into the sterile state ν_b. It would be a possible explanation for the dark matter

[3] In principal, there are also other mechanisms possible without the need of right-handed neutrinos, which we do not discuss in this work.

anomalies, such as the results of CoGeNT and DAMA [8]. It has also been argued in [8] that the constraints coming from meson decays like $K \to \pi\bar{\nu}_b\nu_b$ are not in conflict with large values for the matter potential, because the underlying loop amplitude processes are loop suppressed, compensating possible enhancements due to a large coupling G_B.

In the following we will parametrize this new potential as

$$V_b = \epsilon \cdot \sqrt{2} G_F \frac{\rho}{m_N} = \epsilon \cdot \frac{V_{\mathrm{CC}}}{Y_e}. \tag{4.4}$$

With this definition $\epsilon = G_B/(Y_e \cdot G_F)$ gives the scale of how much larger V_b is compared to the standard charged current potential. As pointed out in [9], ϵ can be of either sign and thus affects whether the corresponding MSW resonance is in the neutrino or in the anti-neutrino sector. Y_e is the number of electrons per nucleon and in general depends on the exact location on the neutrino path.

Let us now consider the mass terms containing a new Higgs - baryonic neutrino coupling as introduced in [8]:

$$\mathcal{L}_m = \mathcal{L}_Y - \sum_j b^j \bar{\nu}_L^b N_R^j (i\tau_2 h_b^*) - \frac{1}{2} \sum_{i,j} \overline{\left(N_R^i\right)^C} m_R^{ij} N_R^j + h.c. \tag{4.5}$$

Here $\mathcal{L}_Y$ is the standard Yukawa term, see equation 2.1 and h_b is the baryonic Higgs doublet. Diagonalizing the mass terms for the neutrinos in a similar way to the standard scenario, see section 2.1, leads to active-sterile mixing. At this point we do not analyse possible mechanisms to explain the magnitude of the neutrino masses and mixing angles. We will focus on the phenomenological analysis and scan over the parameter space, i.e. the mixing angles and mass squared differences.

4.3 Analytical approximation

In order to study the phenomenological implications of such a baryonic neutrino model, in particular on short-baseline neutrino oscillation, Karagiorgi, Shaevitz and Conrad (KSC) investigated this three active plus one sterile neutrino framework, assuming the baryonic matter potential for the sterile neutrino state to be some orders of magnitude larger than the standard matter interactions, i.e. $|\epsilon| \gg 1$, [7]. They derived approximate analytical expressions for the oscillation probabilities that we are not able to reproduce. In the following, we will therefore give a short derivation of the oscillation probabilities obtained in this scenario deviating from the KSC results.

The effective Hamiltonian in the flavour basis, describing neutrino propagation in matter, reads

$$H_{\text{eff}}^{\text{flavour}} = \frac{1}{2E} U \begin{pmatrix} 0 & 0 & 0 & 0 \\ 0 & 0 & 0 & 0 \\ 0 & 0 & 0 & 0 \\ 0 & 0 & 0 & \Delta m_{41}^2 \end{pmatrix} U^\dagger + \begin{pmatrix} 0 & 0 & 0 & 0 \\ 0 & 0 & 0 & 0 \\ 0 & 0 & 0 & 0 \\ 0 & 0 & 0 & V_b \end{pmatrix}, \tag{4.6}$$

where we have assumed $|\Delta m_{41}^2| \gg |\Delta m_{31}^2|, \Delta m_{21}^2$; $|V_B| \gg V_{\text{NC}}, V_{\text{CC}}$ and neglected the subdominant terms for simplicity. In addition we assume $U_{\tau 4} = 0$ in order to further simplify the analytical discussion, following [7]. The probability for a neutrino produced in a certain flavour α travelling over a distance $L \approx t$ to be measured in a flavour β can then be calculated as

$$P_{\nu_\alpha \to \nu_\beta} = \left| \langle \nu_\beta | \nu_\alpha(t) \rangle \right|^2 = \sum_{j=1}^{4} \left| \tilde{U}_{\alpha j}^* \tilde{U}_{\beta j} e^{-iL\lambda_j} \right|^2, \tag{4.7}$$

where $\tilde{U}$ is the unitary matrix diagonalizing the effective Hamiltonian and λ_i are the corresponding eigenvalues: $H_{\text{eff}}^{\text{flavour}} = \tilde{U} \text{diag}(\lambda_1, \lambda_2, \lambda_3, \lambda_4) \tilde{U}^\dagger$. The diagonalization gives $\lambda_1 = \lambda_2 = 0$ as well as $\tilde{U}_{\mu 1} = 0$ and $\tilde{U}_{e1} = 0$. Note that the approximation $\lambda_3 = 0$ is used in [7], which we will not follow here. For the $\nu_\mu \to \nu_\mu$ disappearance channel ($\alpha = \beta = \mu$ in equation 4.7) this yields

$$P_{\nu_\mu \to \nu_\mu} = \left| e^{-i\lambda_3 L} + |\tilde{U}_{\mu 2}|^2 (1 - e^{-i\lambda_3 L}) + |\tilde{U}_{\mu 4}|^2 (e^{-i\lambda_4 L} - e^{-i\lambda_3 L}) \right|^2, \tag{4.8}$$

where we have used the unitarity condition $|\tilde{U}_{\mu 3}|^2 = 1 - |\tilde{U}_{\mu 2}|^2 - |\tilde{U}_{\mu 4}|^2$. We expand this expression by using the relation for the squared absolute value of the sum of three complex numbers $|a + b + c|^2 = |a|^2 + |b|^2 + |c|^2 + 2\,\text{Re}\,[a^* b + a^* c + b^* c]$:

$$\begin{aligned} P_{\nu_\mu \to \nu_\mu} = \; & 1 + |\tilde{U}_{\mu 2}|^4 |1 - e^{-i\lambda_3 L}|^2 + |\tilde{U}_{\mu 4}|^4 |e^{-i\lambda_4 L} - e^{-i\lambda_3 L}|^2 \\ & + 2\,\text{Re}\Big[|\tilde{U}_{\mu 2}|^2 e^{i\lambda_3 L} (1 - e^{-i\lambda_3 L}) + |\tilde{U}_{\mu 4}|^2 e^{i\lambda_3 L} (e^{-i\lambda_4 L} - e^{-i\lambda_3 L}) \\ & + |\tilde{U}_{\mu 2}|^2 |\tilde{U}_{\mu 4}|^2 (1 - e^{i\lambda_3 L})(e^{-i\lambda_4 L} - e^{-i\lambda_3 L}) \Big]. \end{aligned} \tag{4.9}$$

With the expressions for the exponential function, $|e^{ix} - e^{-ix}|^2 = 4 \sin^2 x$, as well as

$\mathrm{Re}\left[e^{-ix}\right] = \cos x$, we obtain:

$$\begin{aligned} P_{\nu_\mu \to \nu_\mu} &= 1 + 4|\tilde{U}_{\mu 2}|^4 \sin^2\left(\frac{\lambda_3}{2}L\right) + 4|\tilde{U}_{\mu 4}|^4 \sin^2\left(\frac{\lambda_4 - \lambda_3}{2}L\right) \\ &\quad +2|\tilde{U}_{\mu 2}|^2 \left[\cos(\lambda_3 L) - 1\right] + 2|\tilde{U}_{\mu 4}|^2 \left[\cos\left((\lambda_4 - \lambda_3)L\right) - 1\right] \\ &\quad +2|\tilde{U}_{\mu 2}|^2 |\tilde{U}_{\mu 4}|^2 \left[\cos(\lambda_4 L) - \cos(\lambda_3 L) - \cos\left((\lambda_4 - \lambda_3)L\right) + 1\right]. \end{aligned} \tag{4.10}$$

Using the trigonometric identity $\cos x = 1 - 2\sin^2(x/2)$ leads to

$$\begin{aligned} P_{\nu_\mu \to \nu_\mu} &= 1 + \left(4|\tilde{U}_{\mu 4}|^4 + 4|\tilde{U}_{\mu 2}|^2 |\tilde{U}_{\mu 4}|^2 - 4|\tilde{U}_{\mu 4}|^2\right) \sin^2\left(\frac{\lambda_4 - \lambda_3}{2}L\right) \\ &\quad + \left(4|\tilde{U}_{\mu 2}|^4 + 4|\tilde{U}_{\mu 2}|^2 |\tilde{U}_{\mu 4}|^2 - 4|\tilde{U}_{\mu 2}|^2\right) \sin^2\left(\frac{\lambda_3}{2}L\right) \\ &\quad -4|\tilde{U}_{\mu 2}|^2 |\tilde{U}_{\mu 4}|^2 \sin^2\left(\frac{\lambda_4}{2}L\right). \end{aligned} \tag{4.11}$$

Now one has to insert the expressions for the eigenvalues and the entries of $\tilde{U}$ obtained from the diagonalization:

$$\lambda_3 = \frac{1}{2}\left(V_b + \frac{\Delta m_{41}^2}{2E} - A\right), \tag{4.12}$$

$$\lambda_4 = \frac{1}{2}\left(V_b + \frac{\Delta m_{41}^2}{2E} + A\right), \tag{4.13}$$

$$|\tilde{U}_{\mu 2}|^2 = \frac{|U_{e4}|^2}{1 - |U_{s4}|^2}, \tag{4.14}$$

$$|\tilde{U}_{\mu 4}|^2 = |U_{\mu 4}|^2 \frac{\frac{\Delta m_{41}^2}{2E}\left(A + \frac{\Delta m_{41}^2}{2E} - V_b\right)}{A\left(A + \frac{\Delta m_{41}^2}{2E} + V_b\right)}, \tag{4.15}$$

where for notational simplicity the following abbreviations have been introduced:

$$\begin{aligned} A &= \sqrt{\left(V_b - \frac{\Delta m^2_{41}}{2E}\right)^2 + 4|U_{s4}|^2 \frac{\Delta m^2_{41}}{2E} V_b}, \\ &= \sqrt{(V_b - V_{\text{res}})^2 + \left(\frac{\Delta m^2_{41}}{2E}\right)^2 - V^2_{\text{res}}}, \qquad (4.16) \\ \phi_1 &= \frac{\lambda_4 - \lambda_3}{2} L = \frac{L}{2} A, \qquad (4.17) \\ \phi_2 &= \frac{\lambda_3}{2} L = \frac{L}{4}(V_b + \frac{\Delta m^2_{41}}{2E} - A), \qquad (4.18) \\ \phi_3 &= \frac{\lambda_4}{2} L = \frac{L}{4}(V_b + \frac{\Delta m^2_{41}}{2E} + A). \qquad (4.19) \end{aligned}$$

At this point it is interesting to note that A becomes maximal, when the MSW resonance condition $V_b = V_{\text{res}}$ is fulfilled. In the simplest two flavour case it corresponds to equation 2.33. Here it is given by

$$V_{\text{res}} := -\frac{\Delta m^2_{41}}{2E}(2|U_{s4}|^2 - 1). \qquad (4.20)$$

Inserting the above expressions into equation 4.11 finally gives the result:

$$\begin{aligned} P_{\nu_\mu \to \nu_\mu} &= 1 - 4\frac{|U_{\mu 4}|^4 |U_{s4}|^2}{1 - |U_{s4}|^2} \frac{(\frac{\Delta m^2_{41}}{2E})^2}{A^2} \sin^2 \phi_1 \\ &\quad -2\frac{|U_{e4}|^2 |U_{\mu 4}|^2}{(1 - |U_{s4}|^2)^2} \left(1 + \frac{V_b - V_{\text{res}}}{A}\right) \sin^2 \phi_2 \\ &\quad -2\frac{|U_{e4}|^2 |U_{\mu 4}|^2}{(1 - |U_{s4}|^2)^2} \left(1 - \frac{V_b - V_{\text{res}}}{A}\right) \sin^2 \phi_3. \qquad (4.21) \end{aligned}$$

Similarly one obtains the probabilities for the other oscillation channels: For the $\nu_e \to \nu_e$ survival probability one just has to replace $\tilde{U}_{\mu i}$ with $\tilde{U}_{ei}$ and obtains from equation 4.11:

$$\begin{aligned} P_{\nu_e \to \nu_e} &= 1 + \left(4|\tilde{U}_{e4}|^4 + 4|\tilde{U}_{e2}|^2 |\tilde{U}_{e4}|^2 - 4|\tilde{U}_{e4}|^2\right) \sin^2 \phi_1 \\ &\quad + \left(4|\tilde{U}_{e2}|^4 + 4|\tilde{U}_{e2}|^2 |\tilde{U}_{e4}|^2 - 4|\tilde{U}_{e2}|^2\right) \sin^2 \phi_2 \\ &\quad -4|\tilde{U}_{e2}|^2 |\tilde{U}_{e4}|^2 \sin^2 \phi_3. \qquad (4.22) \end{aligned}$$

Inserting the eigenvalues and entries of $\tilde{U}$

$$|\tilde{U}_{e2}|^2 = \frac{|U_{\mu 4}|^2}{1-|U_{s4}|^2}, \tag{4.23}$$

$$|\tilde{U}_{e4}|^2 = |U_{e4}|^2 \frac{(A+\frac{\Delta m^2_{41}}{2E}-V_b)^2}{4|U_{s4}|^2(A+\frac{\Delta m^2_{41}}{2E})V_b+(A+\frac{\Delta m^2_{41}}{2E}-V_b)^2}, \tag{4.24}$$

finally leads to:

$$\begin{aligned} P_{\nu_e\to\nu_e} &= 1-4\frac{|U_{e4}|^4|U_{s4}|^2}{1-|U_{s4}|^2}\frac{(\frac{\Delta m^2_{41}}{2E})^2}{A^2}\sin^2\phi_1 \\ &\quad -2\frac{|U_{e4}|^2|U_{\mu 4}|^2}{(1-|U_{s4}|^2)^2}\left(1+\frac{V_b-V_{\text{res}}}{A}\right)\sin^2\phi_2 \\ &\quad -2\frac{|U_{e4}|^2|U_{\mu 4}|^2}{(1-|U_{s4}|^2)^2}\left(1-\frac{V_b-V_{\text{res}}}{A}\right)\sin^2\phi_3. \end{aligned} \tag{4.25}$$

Similarly one can compute the transition probability for $\nu_\mu \to \nu_e$:

$$\begin{aligned} P_{\nu_\mu\to\nu_e} &= -4\tilde{U}_{\mu 2}\tilde{U}^*_{e2}\tilde{U}^*_{\mu 4}\tilde{U}_{e4}\sin^2\phi_1 \\ &\quad +4\left(\tilde{U}_{\mu 2}\tilde{U}^*_{e2}\tilde{U}^*_{\mu 4}\tilde{U}_{e4}+|\tilde{U}_{\mu 2}|^2|\tilde{U}_{e2}|^2\right)\sin^2\phi_2 \\ &\quad +4\left(\tilde{U}_{\mu 2}\tilde{U}^*_{e2}\tilde{U}^*_{\mu 4}\tilde{U}_{e4}+|\tilde{U}_{\mu 4}|^2|\tilde{U}_{e4}|^2\right)\sin^2\phi_3 \end{aligned} \tag{4.26}$$

$$\begin{aligned} &= -4\frac{|U_{e4}|^2|U_{\mu 4}|^2|U_{s4}|^2}{1-|U_{s4}|^2}\frac{(\frac{\Delta m^2_{41}}{2E})^2}{A^2}\sin^2\phi_1 \\ &\quad +2\frac{|U_{e4}|^2|U_{\mu 4}|^2}{(1-|U_{s4}|^2)^2}\left(1+\frac{V_b-V_{\text{res}}}{A}\right)\sin^2\phi_2 \\ &\quad +2\frac{|U_{e4}|^2|U_{\mu 4}|^2}{(1-|U_{s4}|^2)^2}\left(1-\frac{V_b-V_{\text{res}}}{A}\right)\sin^2\phi_3. \end{aligned} \tag{4.27}$$

In the first step we used the fact that the product $\tilde{U}_{\mu 2}\tilde{U}^*_{e2}\tilde{U}^*_{\mu 4}\tilde{U}_{e4}$ is real-valued. This

can be seen by writing

$$\begin{aligned}
\tilde{U}_{\mu 2}\tilde{U}^*_{e2}\tilde{U}^*_{\mu 4}\tilde{U}_{e4} &= \left(\frac{1}{\sqrt{1+\frac{|U_{\mu 4}|^2}{|U_{e4}|^2}}}\right)\cdot\left(-\frac{1}{\sqrt{1+\frac{|U_{\mu 4}|^2}{|U_{e4}|^2}}}\frac{U^*_{\mu 4}}{U^*_{e4}}\right)^* \\
&\quad\cdot\left(U_{\mu 4}\frac{2\frac{\Delta m^2_{41}}{2E}V_b U^*_{s4}}{\sqrt{AV_b\left(A-\frac{\Delta m^2_{41}}{2E}+V_b\right)\left(A+\frac{\Delta m^2_{41}}{2E}+V_b\right)}}\right)^* \\
&\quad\cdot\left(U_{e4}\frac{2\frac{\Delta m^2_{41}}{2E}V_b U^*_{s4}}{\sqrt{AV_b\left(A-\frac{\Delta m^2_{41}}{2E}+V_b\right)\left(A+\frac{\Delta m^2_{41}}{2E}+V_b\right)}}\right) \qquad (4.28) \\
&= \frac{-|U_{e4}|^2|U_{\mu 4}|^2}{|U_{e4}|^2+|U_{\mu 4}|^2}\frac{4\left(\frac{\Delta m^2_{41}}{2E}\right)^2 V_b|U_{s4}|^2}{A\left(A-\frac{\Delta m^2_{41}}{2E}+V_b\right)\left(A+\frac{\Delta m^2_{41}}{2E}+V_b\right)}. \qquad (4.29)
\end{aligned}$$

4.4 Numerical calculation

To verify the validity of the analytical calculations of the previous section, the exact calculation is performed numerically. The following procedure is also used for the phenomenological analysis in chapter 5 the to compute the oscillation probabilities.

We start with the complete effective Hamiltonian

$$H^{\text{flavour}}_{\text{eff}} = \frac{1}{2E}U\begin{pmatrix}0&0&0&0\\0&\Delta m^2_{21}&0&0\\0&0&\Delta m^2_{31}&0\\0&0&0&\Delta m^2_{41}\end{pmatrix}U^\dagger + \begin{pmatrix}V_{\text{CC}}&0&0&0\\0&0&0&0\\0&0&0&0\\0&0&0&V_b\end{pmatrix} \qquad (4.30)$$

and diagonalize it numerically. The resulting unitary matrix $\tilde{U}$ and the eigenvalues λ_i, satisfying the relation

$$H^{\text{flavour}}_{\text{eff}} = \tilde{U}\,\text{diag}\,(\lambda_1,\lambda_2,\lambda_3)\,\tilde{U}^\dagger \qquad (4.31)$$

can now be used to compute the oscillation probability according to equation 4.7.

Note that the matter potential V_{NC} can be absorbed in the definition of V_b. Since V_{NC} is proportional to the neutron number and V_b is proportional to the nucleon number, this is not quite correct in the case of varying matter composition. However, one can replace V_b in the final result with $V_b - V_{\text{NC}}$ if the potentials are of the same

order of magnitude and the change of the number of neutrons per nucleon becomes non-negligible. For our purposes we assume a much larger baryonic potential so that we can stick to the above form of the effective Hamiltonian.

In order to average out very fast oscillations that anyway would not be resolvable by experiments, one can apply a low pass filter in the numerical calculation. It is implemented by weighting each term in the oscillation probability with a Gaussian factor. Starting with the general expression for the oscillation probability in vacuum (equation 2.17) it is easy to show that

$$P_{\nu_\alpha \to \nu_\beta} = \sum_{i,j} U^*_{\alpha i} U_{\beta i} U_{\alpha j} U^*_{\beta j} e^{-iL\frac{\Delta m^2_{ij}}{2E}}. \tag{4.32}$$

Applying the filter leads to

$$P_{\nu_\alpha \to \nu_\beta} = \sum_{i,j} U^*_{\alpha i} U_{\beta i} U_{\alpha j} U^*_{\beta j} e^{-iL\frac{\Delta m^2_{ij}}{2E}} \cdot e^{-\left(L\frac{\Delta m^2_{ij}}{2E}\right)^2 \cdot \frac{\sigma_f(E)^2}{2E^2}}, \tag{4.33}$$

where the width $\sigma_f(E)$ can in general be energy dependent[4]. This method is natural in the sense that the correct wave packet description would yield a term with the same structure as a result of the momentum uncertainty in the neutrino detection and production processes, see references [96, 97, 98] for more details.

It is also possible to apply a filter to the analytical calculations. Essentially one has to perform the following replacement for each oscillation term, e.g. $\sin^2\phi_i$ in equation 4.21:

$$\sin^2\phi \mapsto \frac{1}{2}\left(1 - \cos(2\phi) \cdot e^{-(2\phi)^2 \frac{\sigma_f(E)^2}{2E^2}}\right), \tag{4.34}$$

see e.g. [98] for the derivation in the two flavour framework.

4.5 Discussion of the analytical approximation

In contrast to the analytical approximation by Karagiorgi, Shaevitz and Conrad in [7], our approximation takes into account the third Hamiltonian eigenvalue obtained from the diagonalization, see equation 4.12. In the KSC derivation, they have made the approximation in the expressions for the eigenvalues $A \approx V_b + \frac{\Delta m^2_{41}}{2E}$ leading

[4] Typical values for $\sigma_f(E)$ are a few percent of the energy corresponding to the energy uncertainty in the detection process.

to $\lambda_3 = 0$ and $\lambda_4 = V_b + \frac{\Delta m^2_{41}}{2E}$. The oscillation phases then become $\phi_1 = \phi_3 = \frac{L}{2}\left(V_b + \frac{\Delta m^2_{41}}{2E}\right)$ and $\phi_2 = 0$. With this approximation the complete term proportional to $\sin^2\phi_2$ (see equation 4.21) is neglected. As an example for of the implication of this approximation, let us consider the ν_μ survival probability, equation 4.21. In the limit of very large matter potential $V_b \gg \frac{\Delta m^2_{41}}{2E}, |V_{\text{res}}|$, which leads to $A \approx V_b$, the oscillation probability becomes approximately

$$\begin{aligned} P_{\nu_\mu\to\nu_\mu} &\approx 1 - 4\frac{|U_{\mu4}|^4|U_{s4}|^2}{1-|U_{s4}|^2}\frac{\left(\frac{\Delta m^2_{41}}{2E}\right)^2}{V_b^2}\sin^2\left(\frac{L}{2}V_b\right) \\ &\quad -4\frac{|U_{e4}|^2|U_{\mu4}|^2}{\left(1-|U_{s4}|^2\right)^2}\sin^2\left(\frac{L}{4}V_b\right). \end{aligned} \tag{4.35}$$

The second term is suppressed by $\left(\frac{\Delta m^2_{41}}{2E}/V_b\right)^2$ and the amplitude of the third term can in general be of order 1. Setting for example $\left|U_{\mu4}\right|^2 = \left|U_{e4}\right|^2 = 0.05$ gives

$$P_{\nu_\mu\to\nu_\mu} \sim 1 - \sin^2\left(\frac{L}{4}V_b\right). \tag{4.36}$$

Note that, as mentioned above, in the KSC approximations this term is neglected, which is the leading order term in this parameter regime. For the KSC LSND/MiniBooNE best fit values it even dominates over the atmospheric oscillation (see figure 4.1). Their best fit parameters are $V_b = 2\cdot10^{-10}\,\text{eV}$ ($\epsilon \sim 10^3$), $\Delta m^2_{41} = 0.74\,\text{eV}^2$ and $\left|U_{\mu4}\right|^2 = \left|U_{e4}\right|^2 = 0.05$.

Figure 4.1 shows $P_{\nu_\mu\to\nu_\mu}$ for the numerical calculation, the KSC analytical approximation as well as our approximation derived in the previous section. Here we have applied a low pass filter (as introduced in section 4.4) with $\sigma_f = 0.1\,\text{GeV}$ in order to average out very fast oscillations. The computation was done for the neutrino path length of the MINOS near and far detector at the energy range MINOS is sensitive to. The results clearly show that at the far detector for the KSC best fit value of the matter potential the oscillation pattern is dominated by the term proportional to $\sin^2\phi_2$ (see equation 4.21) as discussed above. The KSC approximation therefore holds only at the near detector. In the limit $V_b = 0$ (gray curves) the two analytical approximations coincide. Since the numerical calculation also accounts for the standard mixing parameters, one can see the effect of the atmospheric oscillation, which however is suppressed for large matter potentials V_b. At this point, we have to mention that the KSC plot (figure 11 in [7]) can not fully be reproduced, although we used the same analytical expressions and parameter values: The structure for $V_b = 0$,

$L = 735\,\mathrm{km}$ at higher energies slightly[5] deviates from our plot.

On the other hand, at the MiniBooNE sensitive energy range, the KSC result (figure 7 in [7]) can be reproduced as shown in figure 4.2. Here we have used again the KSC best fit values, but this time applied no low pass filter in the calculation, since there are no fast oscillations at that energy range. We have checked that the numerical calculation yields the same result as our analytical approximation (since in the standard scenario no ν_μ appearance is expected at MiniBooNE). Therefore only the two analytical expressions are compared with each other. The figure shows a large discrepancy at high energies in the anti-neutrino mode. The difference in the neutrino mode is much smaller. The KSC fit is nevertheless useful, because the rise at low energies is the relevant feature for explaining the MiniBooNE and LSND anomalies. Note that Karagiorgi et al. used the MiniBooNE anti-neutrino data set with $5.66 \cdot 10^{20}$ protons on target (POT) from [95]. The data collection in the anti-neutrino mode has continued in the meantime and the MiniBooNE collaboration has presented a anti-neutrino data set containing events from $11.27 \cdot 10^{20}$ POT [87]. In our analysis presented in the next chapter we use the newer data set.

In summary of this chapter, we have introduced an interesting SM extension with the potential to give a possible explanation not only for anomalies in neutrino oscillation experiments, but also for signals found in current dark matter direct detection experiments [8, 9]. We have derived approximate analytical expressions for the oscillation probabilities offering a simple description of the new features introduced by the baryonic neutrino model. We have seen that although the analysis by Karagiorgi et al. is based on an analytical approximation, which does not give the correct result in the whole parameter space, their work motivates a more detailed phenomenological analysis of the baryonic neutrino model, especially with respect to the LSND/MiniBooNE anomalies (now including the current anti-neutrino data set), the MINOS long baseline experiment as well as solar experiments.

In the next chapter we study the quantitative implications of the baryonic neutrino model using the numerical calculation in the full four flavour framework. In this context we find that the KSC best fit is excluded by the MINOS data.

[5] The KSC plot for $V_b = 0$, $L = 735\,\mathrm{km}$ shows some oscillating structure, but the amplitude is similar.

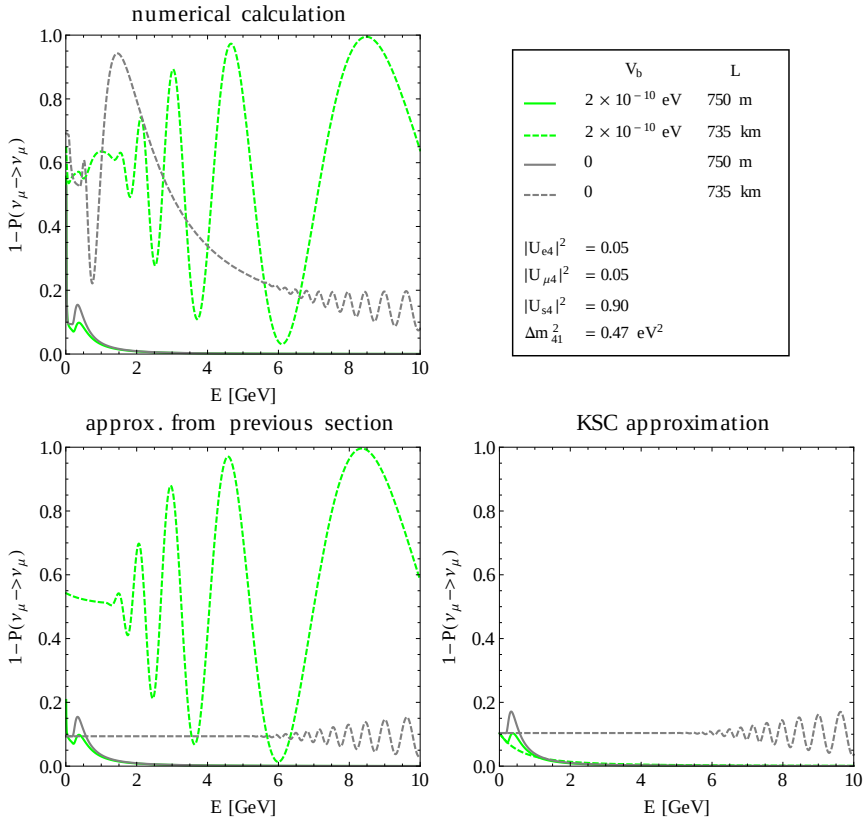

Figure 4.1: The figure shows the analytical expressions for the ν_μ disappearance probability derived in section 4.3 (lower left panel) for the KSC LSND/MiniBooNE best fit values. It is compared to the approximation of Karagiorgi, Shaevitz and Conrad (using equations 20 and 28 in [7]) that they have used to test the compatibility of their LSND/MiniBooNE fit with the MINOS neutrino disappearance experiment (lower right panel). As one can see, their approximation is valid for the MINOS near detector $L_{\text{near}} = 750\,\text{m}$ and in the limit $V_b = 0$, but at the far detector $L_{\text{far}} = 735\,\text{km}$ with $V_b = 2 \times 10^{-10}\,\text{eV}$ there is a large discrepancy between these two approximations. In the upper panel the result of the exact numerical calculation is shown using the full four flavour oscillation framework with the standard oscillation parameter values taken from the global analysis by Gonzales-Garcia et al. [60]. Here the essential difference compared to the approximation from section 4.3 is the effect of the atmospheric oscillation parameters, which is suppressed if the new matter potential is switched on.

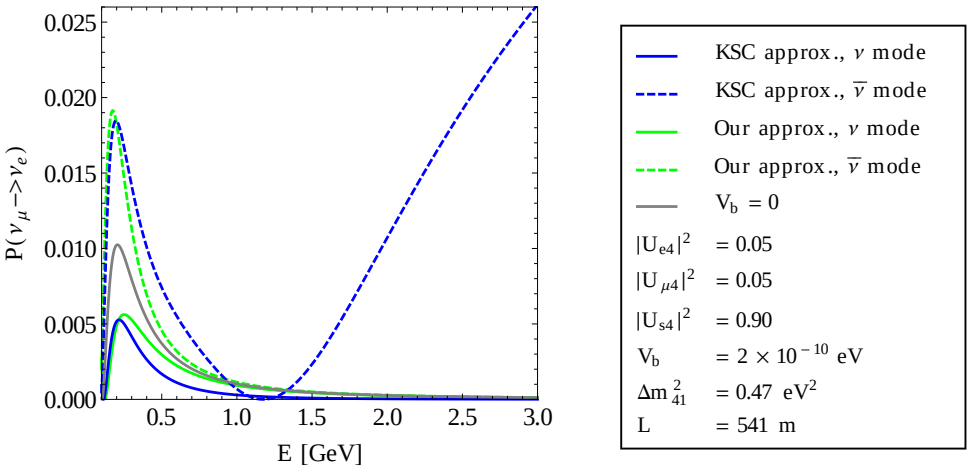

Figure 4.2: The figure shows the electron (anti-)neutrino appearance probability in a beam of muon (anti-)neutrinos as function of energy. Solid curves correspond to the neutrino mode, dashed curves to the anti-neutrino mode, i.e. to a negative sign of the matter potential V_b. The neutrino path length is chosen such that MiniBooNE would be sensitive to a possible neutrino appearance in this energy range. The blue curves show the KSC approximation (equation 21 and 22 in [7]). It reproduces figure 7 in [7]. In green: the result of our approximation, using equation 4.27. In the given parameter space, the exact numerical calculation (including the three flavour standard scenario parameters) yields the same result. In gray: the oscillation probability for $V_b = 0$, in this limit all three methods coincide.

Chapter 5

Phenomenological analysis of gauged sterile neutrinos

In this section we study the phenomenological consequences of the previously introduced baryonic neutrino model. For this purpose the impact of neutrino oscillation measurements on the parameter space of this model is analysed. First the analysis procedure for each experiment is introduced in detail and second we present the results.

5.1 Analysis method

In order to extract limits from experimental data we start by assigning values to the oscillation parameters of the theory and calculate what experiments would have observed, if this particular parameter set was chosen by nature. We then compare this prediction with the results of the measurements and get an answer to the question wether or not this parameter choice is consistent with the data. In this way we scan the parameter space using the χ^2 function:

$$\chi^2 = \sum_{\text{energy bins}\,\{E_i\}} \frac{(N_{\text{theory}}(E_i) - N_{\text{experiment}}(E_i))^2}{\sigma^2(E_i)}. \tag{5.1}$$

The label "N" corresponds to the measured number of events or the oscillation probability $P_{\nu_\alpha \to \nu_\beta}$ (i.e. the ratio of the observed events and the no oscillation expectation $\frac{N_{\text{observed}}}{N_{\text{no osc}}}$) respectively depending on the experimental data refered to. E_i is the energy of the center of the i-th bin and $\sigma(E_i)$ the experimental uncertainty at that energy.

In the following subsections it is explained how the predicted event spectra N_{theory} for the different experiments are computed.

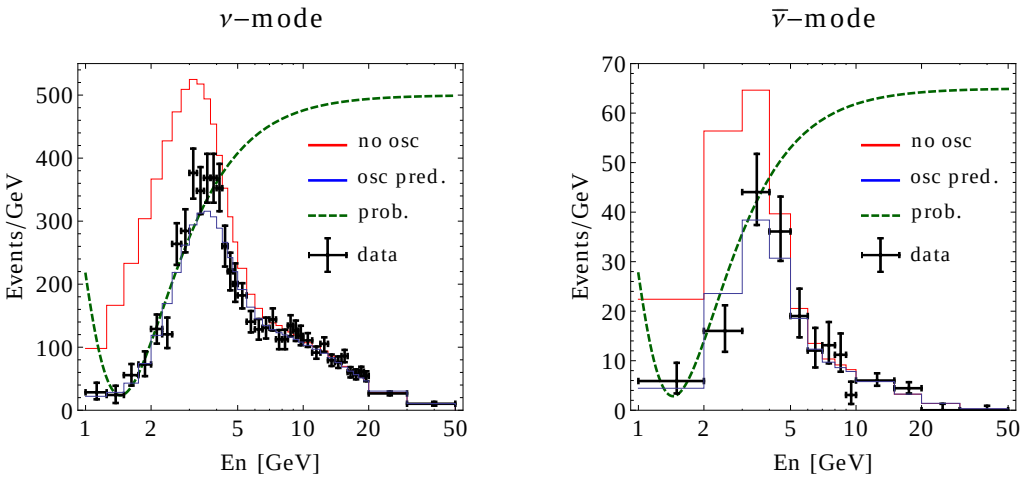

Figure 5.1: The event spectrum of the MINOS ν_μ and $\overline{\nu}_\mu$ disappearance measurement is shown. In red: The MINOS prediction assuming no neutrino oscillation. In blue: Our prediction assuming three flavour standard neutrino oscillation. Dashed green curve: The oscillation probability $P_{\nu_\mu \to \nu_\mu}$ streched by a factor of 540 (68) for the (anti-)neutrino mode. In black: The data points measured by the MINOS experiment.

5.1.1 MINOS ν_μ and $\overline{\nu}_\mu$ disappearance

In our analysis we use the data of the MINOS muon neutrino mode with $10.71 \cdot 10^{20}$ POT and the anti-neutrino mode with $3.36 \cdot 10^{20}$ POT as presented in [81]. In figure 5.1 the experimental data as well as the MINOS no oscillation prediction are shown. The blue line is computed with the method explained below and corresponds to the prediction assuming standard three flavour oscillations with the values taken from the global fit by Gonzalez-Garcia et al.[1][60].

In order to compute the predicted events/GeV as function of L/E we include the oscillation propability of the near and far detector P_{near}, P_{far} and account for the energy smearing, matter effects and the background. For this purpose we have to estimate the length of the neutrino path from the target to the near detector L_{near} and from the target to the far detector L_{far} as well as the averaged matter densities $\langle \rho_{\text{near}} \rangle$ and $\langle \rho_{\text{far}} \rangle$.

[1] In the following we will refer to this parameter set as the standard scenario for neutrino oscillations. However we set the CP violating phase to zero $\delta_{13} = 0$, because this is still a valid assumption and simplifies the analytical discussion.

Neutrino path length and averaged matter density

For the far detector the length is given as $L_{\text{far}} = 735\,\text{km}$ [78]. The density is estimated with the help of the matter profile of the earth obtained from the Preliminary Reference Earth Model (PREM) [99]. The first step is to average the density over the neutrino path:

$$\langle \rho_{\text{far}} \rangle = \frac{1}{L_{\text{far}}} \int_0^{L_{\text{far}}} \rho\left(r(l)\right) dl = \frac{2}{L_{\text{far}}} \int_0^{L_{\text{far}}/2} \rho\left(r(l)\right) dl. \tag{5.2}$$

Using the cosine formula $r^2 = l^2 + R^2 - 2lR\cos\alpha$ and the relation $\cos\alpha = \frac{L_{\text{far}}/2}{R}$ yields $r(l) = \sqrt{l^2 + R^2 - L_{\text{far}} l}$ (see figure 5.2) and one can perform a variable transformation $l \to r$:

$$\langle \rho_{\text{far}} \rangle = \frac{2}{L_{\text{far}}} \int_{\sqrt{R^2-(L_{\text{far}}/2)^2}}^{R} \rho(r) \frac{d}{dr} \left(\sqrt{r^2 - R^2 + (L_{\text{far}}/2)^2} \right) dr. \tag{5.3}$$

Discretising the integral leads to

$$\langle \rho_{\text{far}} \rangle = \sum_i \rho(r_i) \left. \sqrt{r^2 - R^2 + (L_{\text{far}}/2)^2} \right|_{r=r_{i-1}}^{r=r_i}, \tag{5.4}$$

where we use the stepsize in the sum over r as given by the PREM profile. Finally the result is $\langle \rho_{\text{far}} \rangle = 2.36 \frac{\text{g}}{\text{cm}^3}$.

Compared to the neutrino path length for the far detector, the estimate of the path length for the near detector L_{near} is more involved. Here the distance from the target to the near detector is $L_{\text{target}} = 965\,\text{m}$ so that the decay length of the pions become important. Only pions decaying inside the $L_{\text{pipe}} = 675\,\text{m}$ long decay pipe [78] contribute to the neutrino production otherwise they are stopped by the absorber. Therefore the neutrino path length L_{near} has to be estimated by calculating the average decay length of those pions decaying inside the decay pipe: Consider a pion with the velocity v produced by an incoming proton hitting the target. The probability density f that it decays after a distance s is proportional to $f(s) \sim e^{-\frac{s}{\tau\gamma v}}$, where τ is the mean lifetime of the pion and γ the Lorentz factor. The probability that one of these pions decays in a certain region Δs can then be calculated as

$$\int_{\Delta s} f(s) ds = \alpha^{-1} \int_{\Delta s} e^{-\frac{s}{\tau\gamma v}} ds, \tag{5.5}$$

where the normalization $\alpha = \tau\gamma v(1 - e^{-L_{\text{pipe}}/(\tau\gamma v)})$ is chosen such that $\int_0^{L_{\text{pipe}}} f(s) ds =$

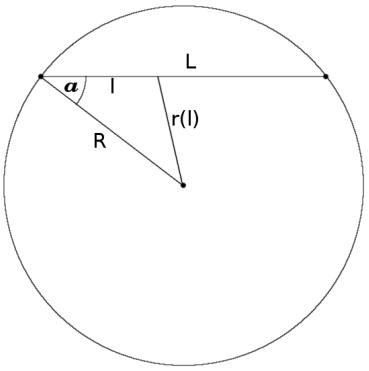

Figure 5.2: This figure illustrates the geometrical arguments for the calculation of the mean desity out of the PREM profile. L is the path length of the neutrino beam between the target and the far detector, R is the radius of the earth and r/l gives the current position of the neutrino with respect to the distance of the center of the earth/with respect to the near detector.

1. Now it is straightforward to calculate L_{near}, which is the average distance covered by the muon neutrinos from the point of production until they reach the near detector:

$$\begin{aligned} L_{\text{near}} &= L_{\text{target}} - \int_0^{L_{\text{pipe}}} f(s) s ds \\ &= L_{\text{target}} - \tau\gamma v - \frac{L_{\text{pipe}}}{1 - e^{\frac{L_{\text{pipe}}}{\tau\gamma v}}}. \end{aligned} \tag{5.6}$$

The momentum of the parent pions is on average $p_\pi \sim 4 - 5\,\text{GeV}$ [100]. Using this information, the relation $v\gamma = c\frac{p_\pi}{m_\pi}$ as well as the values of the pions mass m_π and mean lifetime τ we finally obtain the estimate $L_{\text{near}} = 763\,\text{m}$.

For the average matter density on the neutrino path from the target to the near detector $\langle\rho\rangle_{\text{near}}$ we use a rather rough estimate. The decay pipe is 675 m long. After the pions decay, the neutrinos pass through the rest of the evacuated decay pipe and then travel $L_{\text{dirt}} = 290\,\text{m}$ through the earth with roughly the density of $3\frac{\text{g}}{\text{cm}^3}$. Since the average neutrino path is approximately $L_{\text{near}} = 763\,\text{m}$ as argued above, we estimate the density to be around $\langle\rho\rangle_{\text{near}} = L_{\text{dirt}}/L_{\text{near}} \cdot 3\frac{\text{g}}{\text{cm}^3}$.

Computation of the predicted events

The analysis of the MINOS data with respect to the new model works as follows: We start with the MINOS no oscillation prediction for the measured number of events

as function of energy $N_{\text{no osc}}$ and subtract the background N_{bg}. The result has to be multiplied with the neutrino survival probability, which is given by the ratio $\frac{P_{\text{far}}}{P_{\text{near}}}$. The reason is that MINOS assumes $P_{\text{near}} = 1$. But in the case of a non-negligible neutrino disappearance at the near detector, the MINOS event prediction would be wrong. Therefore we compensate this effect by dividing by P_{near}. In this way we obtain the theoretically predicted number of signal events for the i-th energy bin:

$$N_{\text{th}}(E_i) = (N_{\text{no osc}}(E_i) - N_{\text{bg}}(E_i)) \frac{P_{\text{far}}(E_i)}{P_{\text{near}}(E_i)}. \tag{5.7}$$

In the caclulation of the oscillation probabilities we apply a low pass filter in order to average out very fast oscillations that would not be resolvable by the experiment and would lead to aliasing effects when evaluating the theoretical prediction at descrete points. The filter is implemented by weighting each summand in the oscillation probability with a Gaussian factor as it is described in section 4.4. The width is chosen to be $\sigma_f(E) = 0.06E$. The calculations of the neutrino oscillation probabilities for the χ^2 analysis including a low pass filter was made with the help of GLoBES [101, 102].

Before one can compare the result of equation 5.7 to the experimental data, the energy smearing has to be taken into account. Due to the statistical error in the energy reconstruction of detected events the measured event spectrum is distorted. Especially peaks and minima are affected, because it is more likely that events of true energy near a maximum are wrongly assigned to a different energy than those of true energy near a minimum. This leads to a smeared reconstructed spectrum. For a quantitative description we assume the uncertainties in the energy measurements to be Gaussian distributed. In this case the probability density to detect a neutrino of true energy E' as an event of energy E is given by

$$f(E, E') = \frac{1}{\sigma(E')\sqrt{2\pi}} \exp\left(-\frac{(E - E')^2}{2\sigma^2(E')}\right), \tag{5.8}$$

where the energy uncertainty $\sigma(E') = 0.2\,\text{GeV}\sqrt{E'/\text{GeV}}$ is chosen such that the MINOS standard oscillation prediction can be reproduced up to sufficient accuracy. With this information we obtain the reconstructed event spectrum from the theoretically predicted events by folding it with the probability density $f(E, E')$ and adding the background again:

$$N_{\text{rec}}(E') = \int_0^{E_{\max}} f(E, E') N_{\text{th}}(E) dE + N_{\text{bg}}(E') \tag{5.9}$$

The discretised version then reads:

$$N_{\mathrm{rec}}(E_i) = \sum_j \left(N_{\text{no osc}}(E_j) - N_{\mathrm{bg}}(E_j)\right) \frac{P_{\mathrm{far}}(E_j)}{P_{\mathrm{near}}(E_j)} f(E_i, E_j) + N_{\mathrm{bg}}(E_i) \tag{5.10}$$

with the smearing matrix

$$f(E_i, E_j) = \int_{E_i - \Delta E_i/2}^{E_i + \Delta E_i/2} f(E, E_j) dE. \tag{5.11}$$

As bin size for the unsmeared binning, i.e. the binning of the energy E_j in the previous equations, we use 0.25 GeV. We have checked that smaller bin sizes do not lead to further improvements in the results.

In addition to the individual statistical errors for each data point we include an overall systematic error of 10% in the calculation of χ^2, i.e. we replace $\sigma(E_i)$ in equation 5.1 with $\sigma(E_i) = \sigma_{\mathrm{stat}}(E_i) + 0.1 \cdot N_{\mathrm{experiment}}(E_i)$. This is a conservative approach in order to avoid bounds which are too strict. The choice of the amount of systematic error as well as the statistical error (see equation 5.8) included in our analysis is done in view of a χ^2 analysis in a simple two flavour approximation regime, where the MINOS analysis presented in [103] is used as reference. We also checked that our numerical calculation in the limit of no baryonic potential are in accordance with the limits obtained from an analysis of the MINOS data with sterile neutrinos as presented in [6].

5.1.2 MiniBooNE

Our computation of the predicted events for the MiniBooNE experiment is rather simple compared to the calculation of the MINOS prediction. Here we use the $\nu_\mu \to \nu_e$ neutrino appearance results in terms of the event ratio $\frac{N_{\mathrm{observed}}}{N_{\mathrm{expected}}}$ with $6.46 \cdot 10^{20}$ POT in neutrino mode and $11.27 \cdot 10^{20}$ POT in anti-neutrino mode [87]. Therefore we only have to compute the oscillation probability $P(\nu_\mu \to \nu_e)_{\mathrm{theory}}$ in order to obtain a reasonable estimate for the event ratio. As in the MINOS case we apply a low pass filter in the calculation of P_{theory} and we need to estimate the neutrino path length as well as the average matter density on that path. Figure 5.3 shows the MiniBooNE neutrino oscillation probability data compared to the prediction for the three flavour standard oscillation parameters and for the new model including a fourth neutrino.

Like in the MINOS calculation we also have to estimate the density and the neutrino path length in order to compute the oscillation probability. The length is approx-

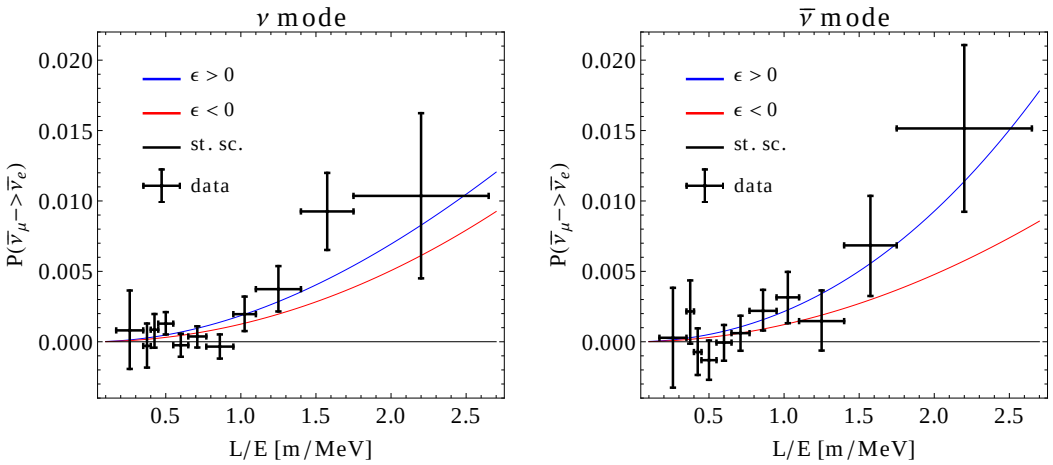

Figure 5.3: The MiniBooNE appearance data (in black) is compared to the standard scenario prediction (back line) and to the prediction including a baryonic neutrino for a matter potential V_b with the same sign as the standard potential V_{CC} (in blue) and with a different sign (in red). The standard scenario predicts a zero transition probability for the MiniBooNE relevant range of L/E. The oscillation probability in the new scenario is shown for the best fit values, see table 5.2.

imately equal to the distance from the target to the detector $L = 541\,\text{m}$, because the decay pipe is only 50 m long [86] and therefore the decay lengths of the neutrinos parent particles (pions and kaons) have only a - for our purpose - negligible impact on the neutrino path length. Likewise for the matter density we use the rough estimate $\langle\rho\rangle \sim 3\frac{\text{g}}{\text{cm}^3}$.

5.1.3 Solar experiments

For the comparison with solar neutrino oscillation experiments we use the data set taken from a recent Borexino publication [104], see figure 5.4. In these results data from Super-Kamiokande, SNO and other solar measurements are included.

The numerical computation is carried out in two ways: A more exact calculation with the help of GLoBES [101, 102] using an extension for the calculation of solar neutrinos [9] as well as a calculation using the adiabatic approximation, which is explained in the next section. As it turns out, the adiabatic calculation is sufficient for our purposes, so that the exact calculation is only used as a cross check in order to ensure the validity of the approximation. Due to the fact that the approximation is less computational expensive, it is the method of our choice. Figure 5.5 shows the

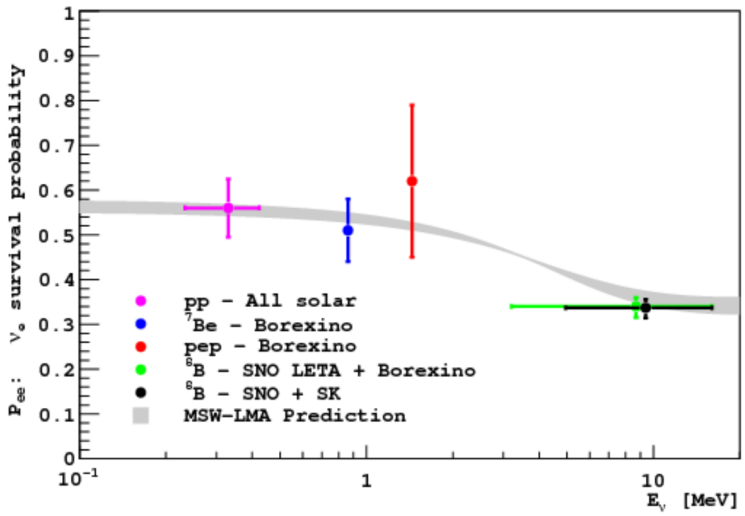

Figure 5.4: The Borexino summary of important solar neutrino oscillation results. This figure shows the neutrino oscillation probability $P_{ee} \equiv P_{\nu_e \to \nu_e}$ as function of energy, measured for different solar neutrino production processes. The gray band corresponds to a theoretical prediction made within the standard framework of neutrino oscillation. The figure is taken from [104].

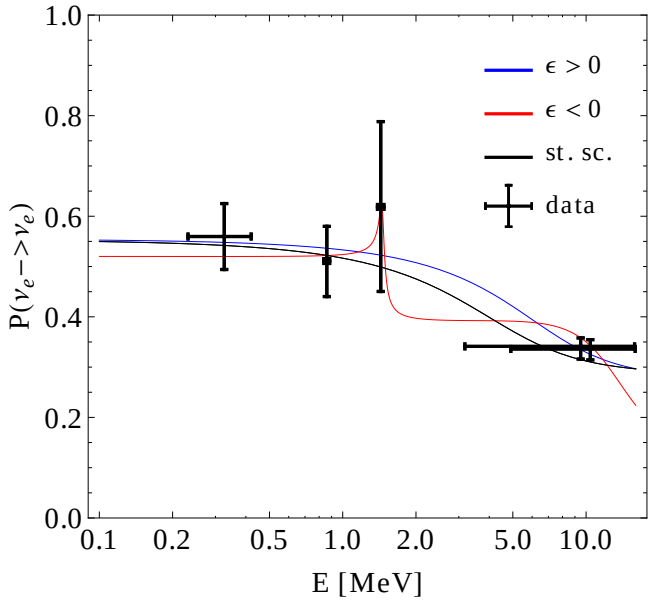

Figure 5.5: This figure shows the data points of solar neutrino oscillation experiments and the predictions for the standard scenario (in black) as well as for the new baryonic neutrino model. Here the best fit values for $\epsilon > 0$ (in blue) and $\epsilon < 0$ (in red) are used, see table 5.2. For a discussion about the features of the $\epsilon < 0$ best fit see section 5.2.4.

prediction for the solar neutrino oscillation obtained by the adiabatic calculation and compares it to the data points. In this plot the curves are shown for the best fit of the baryonic neutrino model as well as using the standard scenario parameters.

adiabatic calculation

The adiabatic approximation for the calculation of the solar neutrino oscillation probability works as follows. We start with the Schroedinger equation in flavour space:

$$i\frac{d}{dt}\left|\nu_\alpha(t)\right\rangle = \sum_\beta H_{\alpha\beta}(t)\left|\nu_\beta(t)\right\rangle = \sum_{\beta,i}\left(U_{\alpha i}\frac{\Delta m^2_{i1}}{2E}U^*_{i\beta} + \delta_{\alpha\beta}V_\beta(t)\right)\left|\nu_\beta(t)\right\rangle . \quad (5.12)$$

The effective Hamiltonian $H_{\alpha\beta}(t)$ is given by the contribution of the mixing matrix U, the eigenvalues in vacuum $\frac{\Delta m^2_{i1}}{2E}$ as well as the time dependent matter potential $V_\alpha(t)$, which in general can be different for each flavour α. To solve the equation it is necessary to diagonalize the matrix on the left hand side of the equation, corresponding to a basis change into the so called matter basis or matter eigenstates. Note

that this is now a third basis, which in matter is different from the flavour and mass basis, as we have discussed in section 2.3.2. We denote this new basis with a tilde and introduce the time dependent unitary matrix $\tilde{U}(t)$ with the properties:

$$|\nu_\alpha(t)\rangle = \sum_i \tilde{U}^*_{\alpha i}(t)\,|\tilde{\nu}_i(t)\rangle \text{ and} \tag{5.13}$$

$$\tilde{H}_{ij}(t) = \delta_{ij}\tilde{E}_i(t) = \sum_{\alpha,\beta} \tilde{U}_{i\alpha}(t) H_{\alpha\beta}(t) \tilde{U}^*_{\beta j}(t), \tag{5.14}$$

where $\tilde{E}_i$ are the eigenvalues of the effective Hamiltonian. By multiplying from the right with $\tilde{U}_{i\alpha}(t)$, summing over α and using equations 5.13 and 5.14, we obtain from equation 5.12:

$$\sum_\alpha \tilde{U}_{i\alpha}(t) i\frac{d}{dt}\left[\sum_j \tilde{U}^*_{\alpha j}(t)\,|\tilde{\nu}_j(t)\rangle\right] = \sum_\alpha \tilde{U}_{i\alpha}(t) \sum_\beta H_{\alpha\beta}(t) \sum_j \tilde{U}^*_{\beta j}(t)\,|\tilde{\nu}_j(t)\rangle \tag{5.15}$$

$$\Leftrightarrow \sum_{\alpha,j}\left[\tilde{U}_{i\alpha}(t)\tilde{U}^*_{\alpha j}(t)\frac{d}{dt} + \tilde{U}_{i\alpha}(t)\frac{d}{dt}\left(\tilde{U}^*_{\alpha j}(t)\right)\right]|\tilde{\nu}_j(t)\rangle = \sum_j \delta_{ij}\tilde{E}_i(t)\,|\tilde{\nu}_j(t)\rangle\,. \tag{5.16}$$

This is a set of coupled differential equations, which in general can not be solved analytically [11]. But if the matter potential changes only slowly with time, such that $\tilde{U}_{i\alpha}\frac{d}{dt}\tilde{U}^*_{\alpha j} \approx 0$, the equation decouples and simplifies to

$$\frac{d}{dt}\,|\tilde{\nu}_i(t)\rangle = \sum_j \delta_{ij}\tilde{E}_i(t)\,|\tilde{\nu}_j(t)\rangle = \tilde{E}_i(t)\,|\tilde{\nu}_i(t)\rangle\,. \tag{5.17}$$

Here we have used the unitarity condition $\tilde{U}_{i\alpha}\tilde{U}^*_{\alpha j} = \delta_{ij}$. Now one can integrate this differential equation and obtain for a neutrino of flavour α produced at time $t = 0$ and detected at time t:

$$\begin{aligned} |\nu_\alpha(t)\rangle &= \sum_i \tilde{U}^*_{\alpha i}(t)\,|\tilde{\nu}_i(t)\rangle \\ &= \sum_i \tilde{U}^*_{\alpha i}(t) \exp\left[-i\int_0^t \tilde{E}_i(t)dt\right]|\tilde{\nu}_i\rangle\,. \end{aligned} \tag{5.18}$$

The oscillation probability for solar neutrinos $P_{\nu_e\to\nu_e}$ can now be calculated by accounting for the incoherence of the neutrino state when reaching the detector at the

earth. This is done according to equation 2.19:

$$\begin{aligned} P_{\nu_e\to\nu_e} &= \sum_i P_{\nu_e\to\tilde{\nu}_i}\cdot P_{\tilde{\nu}_i\to\nu_e} \\ &= \sum_i |\langle\tilde{\nu}_i|\nu_e(t)\rangle|^2\cdot|\langle\nu_e|\tilde{\nu}_i\rangle|^2 \\ &= \sum_{i,j}|\tilde{U}^*_{ei}(t)\exp\left[-i\int_0^t\tilde{E}_i(t)dt\right]|^2\cdot|\langle\tilde{\nu}_j|\tilde{U}_{ej}(0)|\tilde{\nu}_i\rangle|^2 \\ &= \sum_i|\tilde{U}_{ei}(t)|^2\cdot|\tilde{U}_{ei}(0)|^2. \end{aligned} \tag{5.19}$$

For the numerical computation this result means that we have to diagonalize the effective Hamiltonian given by equation 5.12, in order to obtain the mixing matrix $\tilde{U}_{ei}(0)$. For simplicity we assume that the neutrinos are produced at time $t = 0$ in the center of the sun. Therefore the corresponding value for the density is $\rho_{\text{sun}} = 152.9\frac{\text{g}}{\text{cm}^3}$ and the number of electrons per nucleon $Y_e = 0.5\cdot(1+\frac{\#\text{ hydrogen atoms}}{\#\text{ atoms}}) \approx 0.677$ according to the solar standard model BS'05 (OP) [20]. For $\tilde{U}_{ei}(t)$ we use the vacuum mixing matrix, omitting matter effects of the earth. In the numerical calculation of the solar oscillation predictions we average over four equidistant points per energy bin in order to compare the theoretical results with the measurements shown in figure 5.4. We have checked that increasing this number of evaluation points per bin does not lead to substantial improvements in the results.

adiabaticity check

This adiabatic approximation we have used in the previous section is well tested in the framework of standard three flavour neutrino oscillations. However this changes with introducing a matter potential, which can be several orders of magnitude higher than the Fermi potential introduced in section 2.3.1. The approximation is only valid, if the potential changes slowly enough along the neutrino path. Quantitavely this condition corresponds to $\tilde{U}_{i\alpha}\frac{d}{dt}\tilde{U}^*_{\alpha j} \ll 1$, which is a necessary condition that equation 5.17 is valid. In the two flavour regime it can be expressed in terms of the adiabaticity parameter γ, which has to satisfy $\gamma^{-1} \ll 1$. For two neutrinos $(\nu_e\,,\,\nu_\alpha)^T$ with $\alpha = \mu,\tau$ it is given by [11]

$$\gamma^{-1} = \frac{\sin 2\theta\frac{\Delta m^2}{2E}}{|\lambda_1-\lambda 2|^3}\cdot\left|\frac{dV_{\text{CC}}}{dt}\right| \tag{5.20}$$

with the difference of the energy eigenvalues $\lambda_1 - \lambda 2$ given by equation 2.30. In order to check if the adiabaticity condition is still fulfilled for a matter potential of higher order of magnitude we have to calculate γ^{-1} for the two-neutrino system $(\nu_e\,,\,\nu_s)^T$. Here the relevant effective Hamiltonian is

$$H_{\text{flavour}} = U \begin{pmatrix} 0 & 0 \\ 0 & \frac{\Delta m^2}{2E} \end{pmatrix} U^\dagger + \begin{pmatrix} V_{\text{CC}} & 0 \\ 0 & V_b \end{pmatrix}. \tag{5.21}$$

As we have seen in equation 2.17 adding terms proportional to the unit matrix does not change the oscillation probability. Hence the effective Hamiltonian can also be written as

$$H_{\text{flavour}} = U \begin{pmatrix} 0 & 0 \\ 0 & \frac{\Delta m^2}{2E} \end{pmatrix} U^\dagger + \begin{pmatrix} V_{\text{CC}} - V_b & 0 \\ 0 & 0 \end{pmatrix}. \tag{5.22}$$

This leads us to the desired formula for the adiabaticity parameter

$$\gamma^{-1} = \frac{\sin 2\theta \frac{\Delta m^2}{2E}}{|\lambda_1 - \lambda 2|^3} \cdot \left| \frac{dV_{\text{CC}}}{dt} - \frac{dV_s}{dt} \right|. \tag{5.23}$$

Note that we omit the neutral current potential V_{NC}, since it can be absorbed in the definition of V_b. The time dependence of the matter potentials can be calculated with the help of the solar standard model BS'05 (OP) [20], which provides information about ρ and Y_e as function of the radial distance to the center of the earth r. In this way we compute the time derivatives

$$\frac{dV_{\text{CC}}}{dt} = \frac{dV_{\text{CC}}\left(\rho(r)\right)}{dr} \approx \frac{\sqrt{2}G_F}{m_N} \cdot \frac{\Delta Y_e(r)\rho(r) + Y_e(r)\Delta\rho(r)}{\Delta r} \tag{5.24}$$

and

$$\frac{dV_b}{dt} = \frac{dV_b\left(\rho(r)\right)}{dr} \approx \frac{\sqrt{2}G_F}{m_N} \cdot \epsilon \frac{\Delta\rho(r)}{\Delta r}. \tag{5.25}$$

Note that in contrast to the Fermi potential V_{CC} the baryonic potential V_b is not given by the interaction with electrons, but with every nucleon. Therefore its time derivative is given only by the change of the matter density.

For our purposes the interesting values for V_b are at least one order of magnitude higher than V_{CC}, i.e $|\epsilon| \gtrsim 10$ and the electron number per nucleon Y_e is always smaller

than 1. This is why we have

$$Y_e(r)\left|\frac{\Delta\rho(r)}{\Delta r}\right| \ll \left|\epsilon\frac{\Delta\rho(r)}{\Delta r}\right|. \tag{5.26}$$

We have checked explicitly for all radial positions in the sun that this is also true for the second term of the right hand side of equation 5.24:

$$\rho(r)\cdot\left|\frac{\Delta Y_e(r)}{\Delta r}\right| \ll \left|\epsilon\frac{\Delta\rho(r)}{\Delta r}\right|. \tag{5.27}$$

Putting all this together we obtain

$$\gamma^{-1} = \frac{\sin 2\theta\frac{\Delta m^2}{2E}\frac{\sqrt{2}G_F}{m_N}\left|\epsilon\frac{\Delta\rho(r)}{\Delta r}\right|}{\left[\left(\frac{\Delta m^2}{2E}\cos 2\theta + \frac{\sqrt{2}G_F}{m_N}\rho(r)\epsilon\right)^2 + \left(\frac{\Delta m^2}{2E}\right)^2\sin^2 2\theta\right]^{\frac{3}{2}}}. \tag{5.28}$$

The results are shown in figure 5.6, where the inverse adiabaticity parameter is plotted as function of the density in the sun. The computation is done using different values for the vacuum mixing angle θ, the ratio of the mass square difference and the energy $\frac{\Delta m^2}{2E}$ as well as the baryonic matter potential V_b, meaning different values for ϵ. The functional dependence can be understood in the following way: If $\cos 2\theta$ and ϵ have the same sign, there is a resonant increase in $\gamma^{-1}(\rho)$. It peaks at the density minimizing the denominator $|\lambda_1 - \lambda 2|^3$. This resonance density is

$$\rho_{\text{resonance}} = \frac{\Delta m^2\cos 2\theta}{2E\frac{\sqrt{2}G_F}{m_N}\epsilon} \tag{5.29}$$

and corresponds to the MSW resonance introduced in section 2.3.2. Assuming positive ϵ the resonance condition can only be fulfilled if $\sin^2\theta > 0.5$ and for negative ϵ only if $\sin^2\theta < 0.5$. With increasing ϵ as well as for decreasing $\frac{\Delta m^2}{2E}$ the resonance position is shifted towards lower densities. However the absolute value of γ^{-1} increases with ϵ and decreases with $\frac{\Delta m^2}{2E}$, because ϵ appears also in the numerator and $\frac{\Delta m^2}{2E}$ appears with higher power in the denominator than in the numerator. In the case of ϵ and $\cos 2\theta$ having the same sign, γ^{-1} is not affected by resonant behaviour. It increases with increasing ρ due to the rise in the density change $|\frac{\Delta\rho}{\Delta r}|$ (see figure 5.7) until $\frac{\Delta m^2}{2E}\cos 2\theta$ becomes about as large as $\sqrt{2}G_F\rho\epsilon/m_N$. Then $\sqrt{2}G_F\rho\epsilon/m_N$ in the denominator starts dominating and the inverse adiabaticity parameter drops down.

In figure 5.7 the density change $|\frac{\Delta\rho}{\Delta r}|$ is shown, again using the solar standard model.

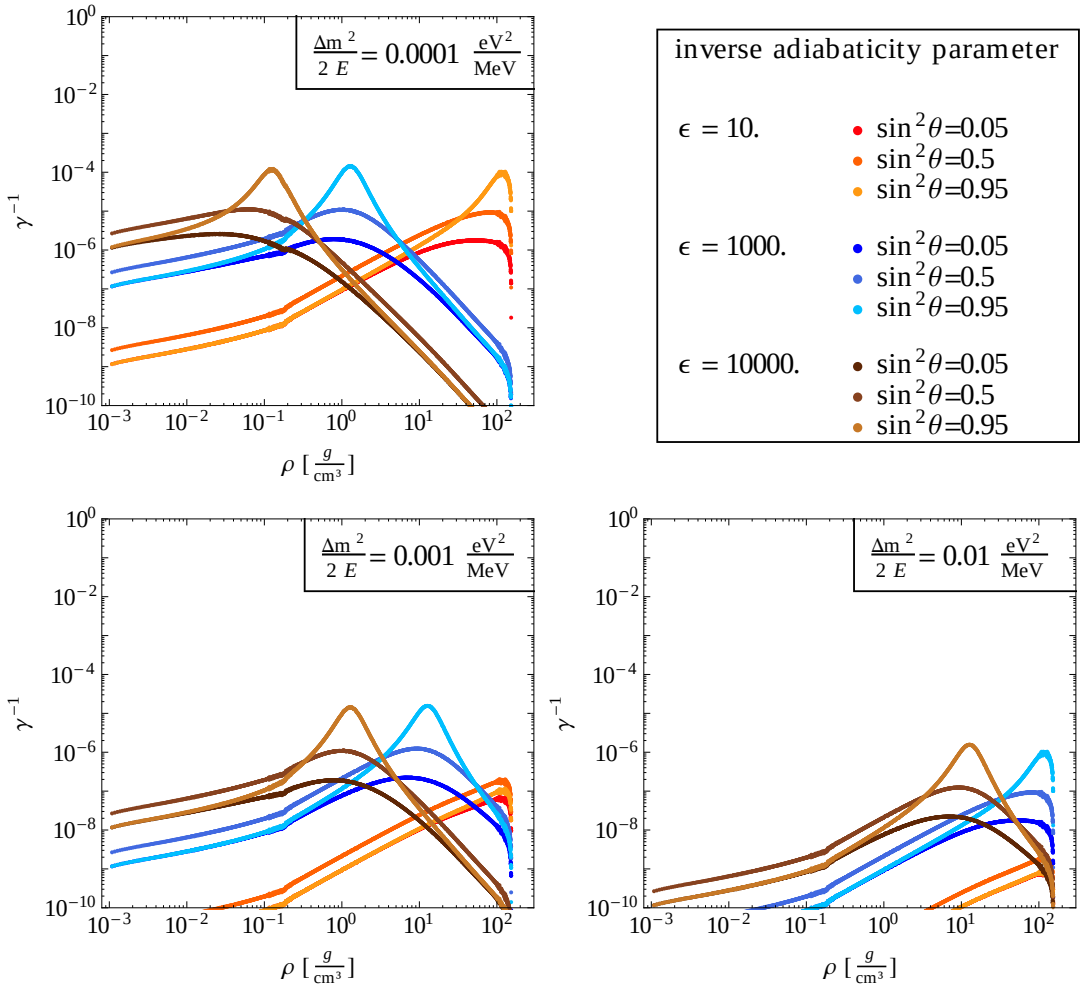

Figure 5.6: The figure shows the inverse adiabaticity parameter as function of the density of the sun. It is shown for several values of θ, ϵ and $\frac{\Delta m^2}{2E}$. Since γ^{-1} always stays below 1 the adiabatic assumption is justified.

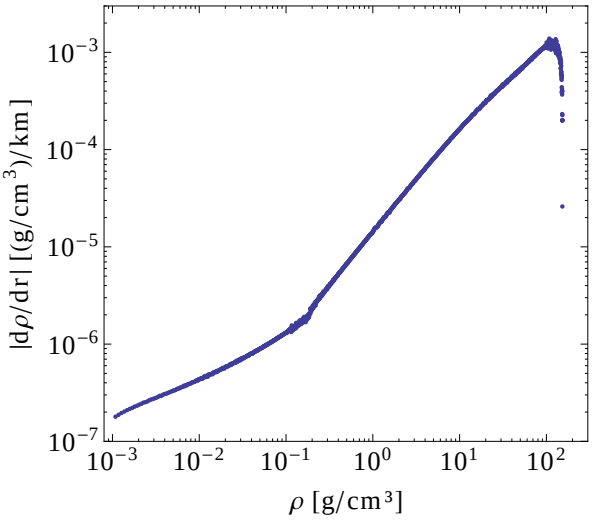

Figure 5.7: The figure shows the change of density inside the sun according to the solar standard model BS'05 (OP) [20]. The change in density increases with decreasing radius. At about $0.2\,\mathrm{g/cm^3}$ there is a little kink and the density change falls down abruptly at the inner layers of the sun.

It explains the flatter increase at the beginning, the little kink at $\rho \sim 0.2\,\mathrm{g/cm^3}$ and the sharp decrease towards the inner region of the sun.

These results clearly justify the adiabatic approximation, since the inverse adiabaticity parameter stays orders of magnitude below 1 even for parameter values satisfiyng the resonance condition, equation 5.29. Only for very large mixing angles θ near to $\pi/2$, γ^{-1} can become close to 1. In this case $\sin^2\theta$ is very small. If now the resonance condition is fulfilled, i.e. if the neutrino passes the resonance density inside the sun, the denominator of equation 5.28 would become proportional to $\sin^3\theta$ and thus γ^{-1} could increase to values of order 1. However such a large mixing angle is not in the interesting regime of the baryonic neutrino model.

Note that this situation is similar in the $\epsilon < 0$ case for very small mixing angles near to 0, what also would lead to small $\sin^2\theta$ values. The resonance condition can then be satisfied, since $\cos 2\theta$ and ϵ woulds have the same sign. In order to check wether the adiabatic assumption is still justified we show in figure 5.8 the results for the regime, where the baryonic potential has a different sign than the charged current potential ($\epsilon < 0$). Here the results are shown only for small mixing angles up to $\sin^2\theta = 0.001$, which is the lower limit in our analysis.

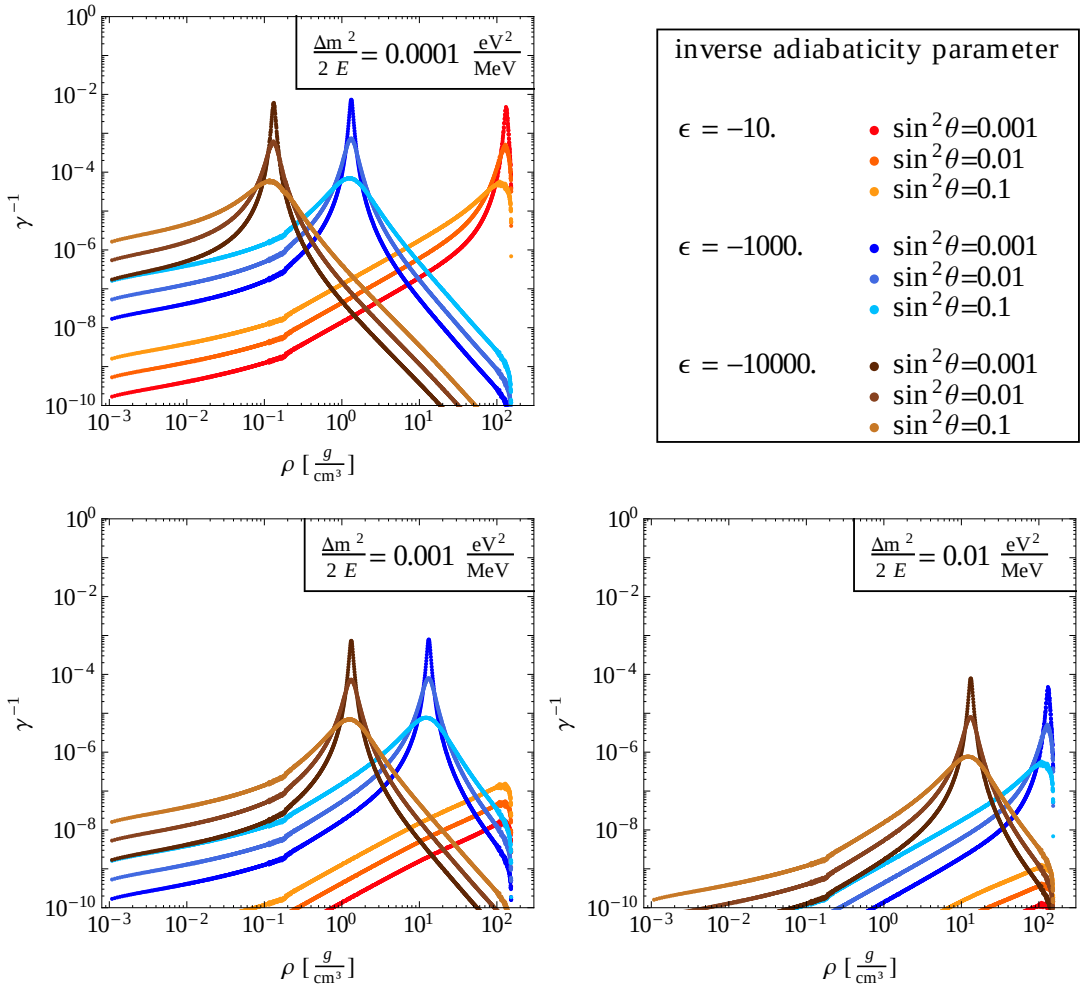

Figure 5.8: The figure shows the inverse adiabaticity parameter as function of the density of the sun, here in the $\epsilon < 0$ regime. It is shown for several values of θ, ϵ and $\frac{\Delta m^2}{2E}$, especially for small mixing angles. Since γ^{-1} always stays below 1 the adiabatic assumption is still justified.

5.2 Results

The parameter space of the baryonic neutrino model was analysed with the methods explained in the previous section. The results are summarized in figures 5.9 and 5.10 and are presented as contour plots showing lines of constant $\chi^2 - \chi^2_{\text{min}}$. Here χ^2_{min} is the minimal χ^2 value, i.e. that of the best fit point. Assuming Gaussian distributed errors each χ^2 value can be assigned to a specific confidence level, which corresponds to a certain probability at which parameters of higher χ^2 value are exluded. Each figure shows the dependence of two parameters, where the remaining ones are either fixed at some values or it has been minimized over them. The minimization procedure works in the following way: First we calculate χ^2 in a given region of the parameter space. Then we choose two parameters, which we want to examine and extract those χ^2 values that are minimal under the remaining parameters. In this way the χ^2 contour plots answer the question: "Assuming that the underlying model is true and that errors are Gaussian distributed, which regions of the parameter space of that model can be excluded and at what confidence level?"

At this point let us mention that the best fit point of the analysis by Karagiorgi, Shaevitz and Conrad [7] is already excluded by MINOS and solar measurements at 99% confidence level. In figure 5.9 this point is indicated with a black triangle. Their best fit values are [7]

$$\Delta m^2_{41} = 0.47\,\text{eV}^2, \quad \sin^2 2\theta_{\mu e} = 0.01, \quad \sin^2 2\theta_{\mu\mu} = 0.188, \quad V_b = 2 \times 10^{-10}\,\text{eV}. \tag{5.30}$$

In our parametrization it corresponds to[2]

$$\Delta m^2_{41} = 0.47\,\text{eV}^2, \quad \sin^2\theta_{24} = 0.052, \quad \sin^2\theta_{14} = 0.05, \quad \epsilon = \frac{2645.5}{\rho/\frac{\text{g}}{\text{cm}^3}}\,\text{eV}. \tag{5.31}$$

In the following we explain the parameter choice for the analysis in detail and discuss the results of the χ^2 scan for each experiment. Afterwards we comment on the impact of $\theta_{34} \neq 0$ on the solar analysis.

[2]Note that in our analysis we have fixed $\sin^2 2\theta_{14} = 0.12$, i.e. $\sin^2\theta_{14} = 0.031$, in order to explain the reactor anomaly. This slightly differs from the actual best fit value, but has a negligible impact on the oscillation probability with respect to the MiniBooNE results. For the purpose of comparison with our analysis, we neglect this difference.

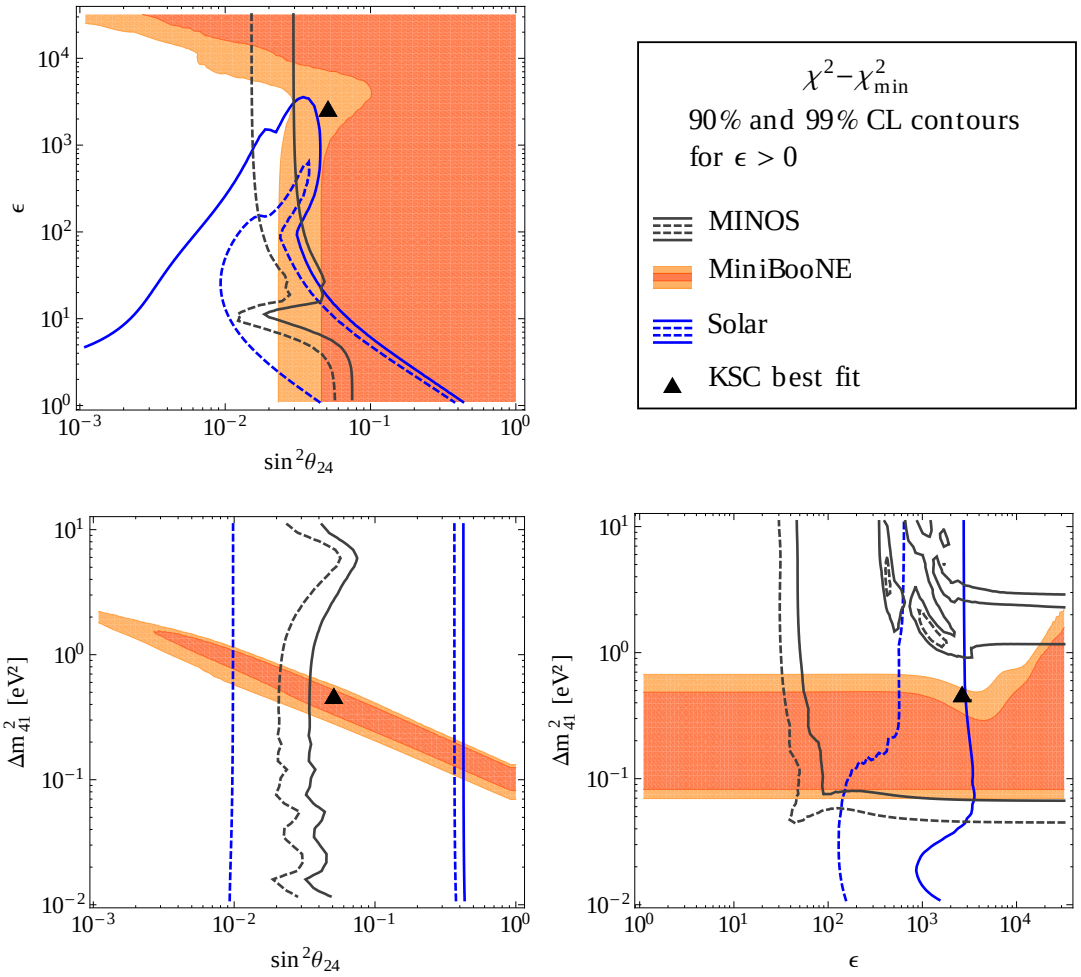

Figure 5.9: The figure shows the $\chi^2 - \chi^2_{min}$ 90% and 99% confidence level contours for the MINOS, MiniBooNE and solar analysis. Here the parameter space with $\epsilon > 0$ has been analysed with respect to ϵ, Δm^2_{41} and $\sin\theta_{24}{}^2$. In each panel the contours are shown as function of two parameters, where we have minimized over the third one. In gray: Limits from the the MINOS ν_μ and $\bar{\nu}_\mu$ disappearance data. In blue: Limits from solar experiments. Coloured regions: Allowed region by the MiniBooNE ν_μ and $\bar{\nu}_\mu$ disappearance data.

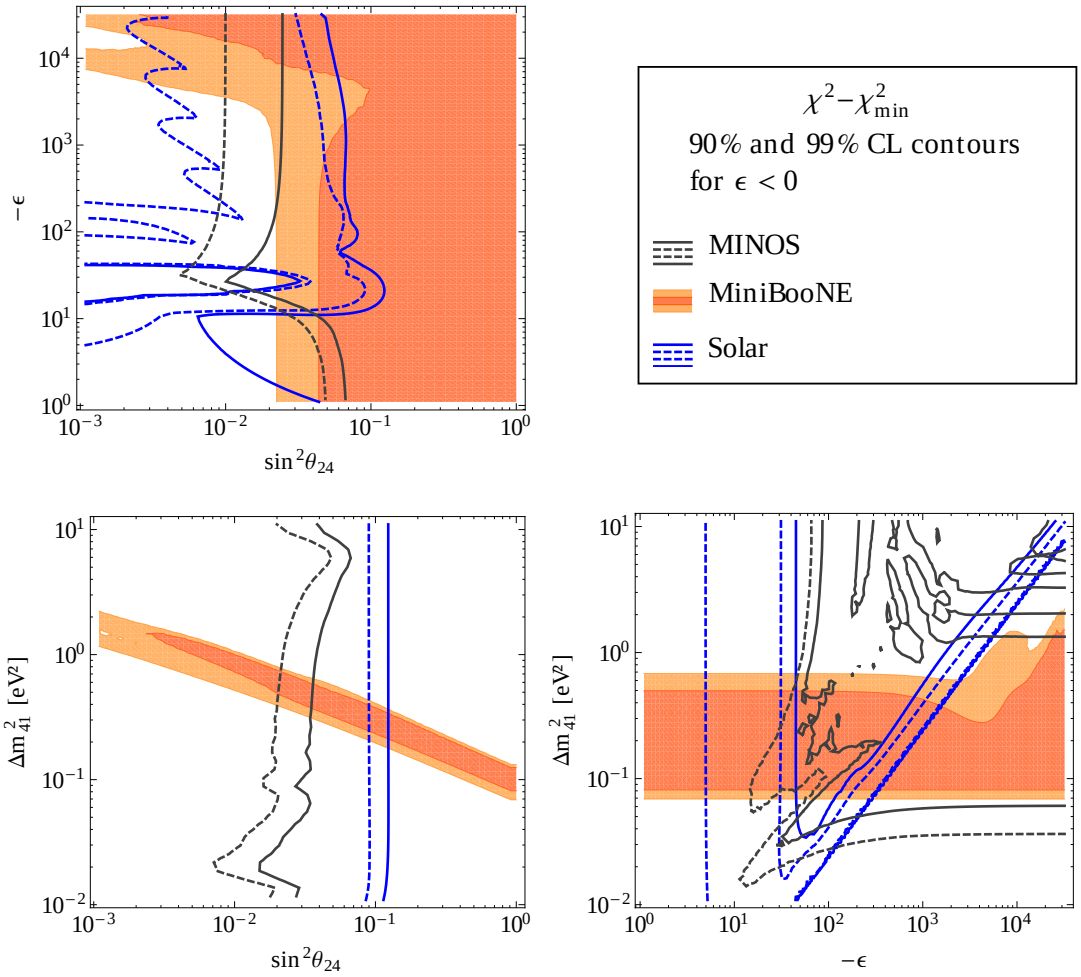

Figure 5.10: The figure shows the $\chi^2 - \chi^2_{min}$ 90% and 99% confidence level contours for the MINOS, MiniBooNE and solar analysis. Here the parameter space with $\epsilon < 0$ has been analysed with respect to ϵ, Δm^2_{41} and $\sin\theta_{24}{}^2$. In each panel the contours are shown as function of two parameters, where we have minimized over the third one. In gray: Limits from the the MINOS ν_μ and $\bar{\nu}_\mu$ disappearance data. In blue: Limits from solar experiments. Coloured regions: Allowed region by the MiniBooNE ν_μ and $\bar{\nu}_\mu$ disappearance data..

$\sin^2\theta_{12}$	$\sin^2\theta_{23}$	$\sin^2\theta_{13}$	Δm^2_{21} [eV^2]	Δm^2_{31} [eV^2]	δ^{CP}_{13}, δ^{CP}_{14}	$\sin^2 2\theta_{14}$	$\sin^2\theta_{34}$
0.302	0.413	0.0227	$7.5 \cdot 10^{-5}$	$2.473 \cdot 10^{-3}$	0	0.12	0

Table 5.1: The table shows the values of all parameters that are fixed for the χ^2 analysis.

5.2.1 Parameter choice

For the following discussion we use this parametrization for the mixing matrix U:

$$U = R_{34} \cdot R_{24} \cdot R_{14} \cdot R_{23} \cdot R_{13} \cdot R_{12}, \tag{5.32}$$

where R_{ij} are 4×4 rotation matrices given by angles θ_{ij} acting in the ij plane. None of this matrices contain complex phases, because we set them to zero in our calculations.

For the χ^2 analysis we fix the three flavour standard oscillation parameters θ_{12}, θ_{23}, θ_{13}, Δm^2_{21} and Δm^2_{31} at the values given by a recent global fit by Gonzalez-Garcia et al. [60], where we use the best fit "Free Fluxes and RSBL". Since there exist no clear experimental evidence yet that the CP violating phase is non-zero, we set $\delta^{CP}_{13} = 0$. For simplicity we also assume $\delta^{CP}_{14} = 0$ as well as normal hierarchy. The mixing angle θ_{14} is chosen such that the flux deficit of the rector experiments can be explained, i.e. we choose $\sin^2 2\theta_{14} = 0.12$ according to the discussion about the reactor anomaly in section 3.3.2, see also figure 3.3. MINOS and MiniBooNE are not sensitive to θ_{34} [6], thus we set it for our analysis to zero. The dependence of the solar experiments on θ_{34} is discussed in section 5.2.4. In table 5.1 the values of all parameters that we have fixed for the parameter scan are summarized. The remaining three parameters θ_{24}, ϵ and Δm^2_{41} are scanned over. Here we write the matter potential for the baryonic neutrino in the form $V_b = \epsilon\sqrt{2}G_F\rho/m_N$ with ϵ being a measure for the magnitude of the new matter potential compared to the standard charged current potential. Since V_b can in principal be of either sign, we perform the analysis for $\epsilon > 0$ as well as for $\epsilon < 0$. The parameters are varied in the ranges $|\epsilon| = 1 - 32000$, $\Delta m^2_{41} = 0.01\,\text{eV}^2 - 10\,\text{eV}^2$ and $\sin^2\theta_{24} = 0.001 - 1$. The resulting best fit values of the χ^2 minimization are listed in table 5.2.

5.2.2 MINOS limits

The limits obtained from the MINOS neutrino and anti-neutrino data sets [81] are shown in figures 5.9 and 5.10. The gray, dashed line corresponds to the 90% and the

		ϵ	Δm^2_{41} [eV^2]	$\sin^2\theta_{24}$	χ^2_{min}/d.o.f.
MINOS	$\epsilon > 0$	16.9	0.014	0.0024	37.7/49
	$\epsilon < 0$	-19.2	0.037	0.00083	36.1/49
MiniBooNE	$\epsilon > 0$	30634	0.316	0.01	16.1/20
	$\epsilon < 0$	-32000	0.116	0.748	16.4/20
Solar	$\epsilon > 0$	37313	0.00033	0.204	0.57/3
	$\epsilon < 0$	-38.0	0.013	0.046	0.44/3

Table 5.2: The best fit points for the different data sets. For the MiniBooNE $\epsilon < 0$ and the solar $\epsilon > 0$ analysis the values for ϵ are located outside the boundary of the analysis region. In both cases χ^2 hardly changes with increasing $|\epsilon|$.

gray, solid line to the 99% confidence level contour. In the following we give a short description of each of the three panels:

- The $\sin^2\theta_{24}$ - Δm^2_{41} plot:

Let us first consider the lower left panel of figure 5.9, i.e. for $\epsilon > 0$. The figure shows that large values $\sin^2\theta_{24} > 10^{-1}$ are exluded.

At Δm^2_{41} values for which the muon neutrino disappearance is enhanced at the MINOS most sensitive energies (around 3 GeV), the exclusion bound is shifted towards lower $\sin^2\theta_{24}$ values. This results in an oscillation pattern as one can see in the lower left panel of figure 5.9, where χ^2 have been minimized with respect to ϵ. A similar structure can be observed in $\sin^2\theta_{24}$ - Δm^2_{41} contour plots of other sterile neutrino analysis like in reference [6], where the two flavour oscillation minima and maxima become visible. At $\Delta m^2_{41} \approx 0.005\,\text{eV}^2$ the disappearance is maximal at neutrinos energies of 3 GeV. The reason is that at that energy the first minimum of the ν_μ and $\bar{\nu}_\mu$ survival probability is given by $\frac{\pi}{L}\frac{2E}{\Delta m^2_{41}} = 1$, as discussed in section 2.2.1. For $\Delta m^2_{41} \approx 0.005\,\text{eV}^2$ this is fulfilled at the far detector. With rising Δm^2_{41} the oscillation becomes faster until it can not longer be resolved (at $\Delta m^2_{41} \approx 0.2\,\text{eV}^2$). At about $3\,\text{eV}^2$ the mass squared difference Δm^2_{41} becomes large enough to suppress oscillations. Therefore the exclusion limit is shifted to higher $\sin^2\theta_{24}$ values. Since the far detector is $\sim 10^3$ times further away from the source than the near detector, at about $3\,\text{eV}^2$ the MINOS near detector becomes sensitive to the disappearance. This is why χ^2 drops again for larger Δm^2_{41}.

For the $\epsilon < 0$ analysis, this behaviour is similar with the exception of the parameter region $\Delta m^2_{41} \sim 0.02\,\text{eV}^2$ and $\sin^2\theta_{24} \sim 2 \cdot 10^{-2}$. At that region is a stronger exclusion limit, as can be seen in figure 5.10, lower left panel. This difference to the $\epsilon > 0$ case is due to the much higher statistics in the neutrino than in the anti-neutrino mode of

the MINOS data set. Therefore, MSW resonances due to the new matter potential only becomes visible in the $\epsilon < 0$ case, where the resonance condition can be met for small mixing angles $\sin^2\theta_{24} < 0.5$. At those values for Δm^2_{41} and $\sin^2\theta_{24}$ the resonance sits at small ϵ. As a consequence, χ^2 is not only large for large ϵ, but also for the low ϵ range due to the resonance position. This means that although in this plot it is minimized over ϵ with respect to χ^2, this resonance effect becomes visible.

- The ϵ - $\sin^2\theta_{24}$ plot:

The MINOS limit on $\sin^2\theta_{24}$ obtained from the upper left panel of figure 5.9 and 5.10 respectively, is essentially the same as for the $\sin^2\theta_{24}$ - Δm^2_{41} plane. Independently of Δm^2_{41} and ϵ, the muon neutrino disappearance for high $\sin^2\theta_{24}$ would be too large to be compatible with the MINOS results. The structure at $\sin^2\theta_{24} \sim 0.02$, $\epsilon \sim 10$ is due to the MSW resonance and can be understood in the following way. As shown in the lower left panel of figure 5.11, for $\epsilon = 10$ the resonance position is inside the MINOS energy region. This is only avoided for $\Delta m^2_{41} \gtrsim 0.1\,\mathrm{eV}^2$ or $\sin^2\theta_{24} \gtrsim 0.5$, what is also not compatible with MINOS leading to large χ^2 values. Hence, there is a stronger bound for $\epsilon \sim 10$. As one would expect, this effect is enhanced, when the resonance appears in the neutrino sector, as one can see in comparing the $\epsilon > 0$ and $\epsilon < 0$ cases.

- The ϵ - Δm^2_{41} plot:

The limit in the ϵ - Δm^2_{41} projection is dominated by χ^2 values corresponding to very low $\sin^2\theta_{24}$, because larger values would yield observable disappearance (as discussed for the $\sin^2\theta_{24}$ - Δm^2_{41} plot: for $\Delta m^2_{41} \approx 0.005\,\mathrm{eV}^2$ the disappearance is maximal at 3 GeV, for rising Δm^2_{41} the oscillation averages out and yields almost energy independent disappearance). This means that the MINOS limits in the lower right panel of figures 5.9 and 5.10 are given by $\sin^2\theta_{24} = 0.001$, which is the lower bound in our analysis. In this sense it is useful to consider the resonance condition for this $\sin^2\theta_{24}$ value: The region between the red lines in the lower right panel of figure 5.11 corresponds to those ϵ and Δm^2_{41} values, for which the resonance position is inside the MINOS energy range. It shows that the structures in the ϵ - Δm^2_{41} plane can be understand in the following way.

For positive ϵ the resonance is only in the anti-neutrino mode and one could expect that it has almost no impact on the oscillation, but this is not the case. At values for the matter potential comparable large as $\Delta m^2_{41}/(2E)$, one of the phases ϕ_2 (equation 4.18) or ϕ_2 (equation 4.19) can become of the order 1, because A contributes with a

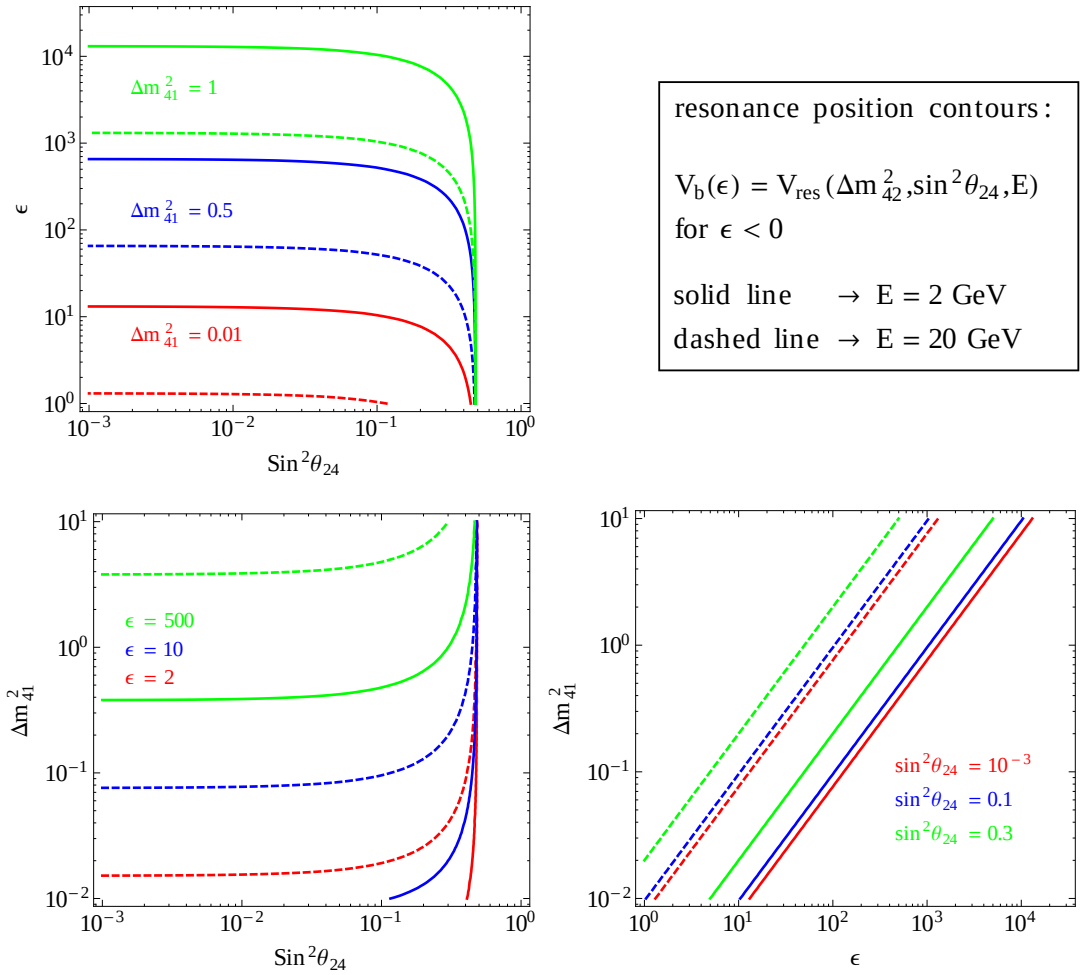

Figure 5.11: The figure shows the resonance position V_{res} shown as contours for different values of $\epsilon, \Delta m^2_{41}, \sin^2\theta_{24}$ and the energy E. The dashed lines are computed for $E = 20\,\text{GeV}$ and the solid lines for $E = 2\,\text{GeV}$. This means that for the whole parameter range in between the dashed and solid lines of the same colour, the resonance condition is fulfilled for energies inside the MINOS sensitive range. The resonance position is computed in the two flavour approximation, equation 4.20. For the computation of V_{res}, we use the matrix element given in our analytical approximation. In our parametrization it is given by $|U_{s4}|^2 = \cos^2\theta_{24}\cos^2\theta_{14}$, where we have set $\sin^2 2\theta_{14} = 0.12$ and use the average density ρ_{far} for the MINOS far detector (as computed in section 5.1.1). The MINOS experiment is sensitive to oscillation effects in the energy range from 2 GeV up to 20 GeV (compare to figure 5.1). Thus, for parameter values in between the dotted and the solid line of the same colour, the MSW resonance affects the MINOS simulation.

minus sign to ϕ_2 and with a plus sign to ϕ_1. Therefore the oscillation become again visible, which explains the complicated oscillation structure in the upper right corner.

In the $\epsilon < 0$ case, the resonance condition is fulfilled and thus leads to an enhancement of these oscillation structures, because now not only the oscillation phases, but also the amplitude are enhanced due to the resonance (compare to equation 4.21).

5.2.3 MiniBooNE limits

The MiniBooNE limit in the $\sin^2\theta_{24}$ - Δm^2_{41} plane is essentially given by the two flavour vacuum oscillations, since the matter effect has only a small impact on such short baselines. Therefore the allowed region is similar to those obtained in the MiniBooNE two flavour analysis [87]. However for large matter potentials, one can see that the allowed region in the ϵ - Δm^2_{41} and ϵ - $\sin^2\theta_{24}$ projections is expanded. This feature arises from the contribution of both, the $\Delta m^2_{24}/(2E)$ term as well as the matter potential, to the oscillation phases $\phi 2$ and $\phi 3$. This is why even for very small $\sin^2\theta_{24}$ the baryonic neutrino model still provides a good fit to the data, if the matter potential is large enough. It is also interesting to note that the difference in the neutrino and anti-neutrino mode (as discussed in [87]) is compensated by the enhancement due to the matter potential. Figure 5.3 illustrates how the $\epsilon > 0$ best fit has the potential to explain the larger excess in the anti-neutrino compared to the neutrino mode. From the MiniBooNE analysis one can conclude that large ($\epsilon > 7{\cdot}10^3$) matter potential[3] are favoured and that the $\epsilon < 0$ case is slightly preferred.

Note that the combined MiniBooNE and MINOS results disfavour matter potentials $10^1 < |\epsilon| < 10^4$ at the 90% confidence level. This can be seen in the ϵ - Δm^2_{41} and ϵ - $\sin^2\theta_{24}$ panels of figures 5.9 and 5.10.

5.2.4 Solar limits

The results for the solar analysis show some interesting features, especially in the $\epsilon < 0$ case, where the resonance occours in the neutrino sector and thus affects the solar $\nu_e \to \nu_e$ survival probability. First of all, note that already the spectrum for our best fit point, shown in figure 5.5, indicates the reason for this feature. The data point between 1 MeV and 2 MeV lies at a slightly higher value than the neighbors. The best fit seems to fit this exactly and explains the lower ν_e event rate at the ^8B points. Note that this is no significant effect, since the error bars are relatively large.

[3] Note that $\epsilon \sim 10^4$ is outside the interesting region for the baryonic model.

However this leads to structures, which eventually affects at least the 90% contour (see figure 5.10, upper right panel).

For $\epsilon \sim -25$ there is a large dip in the χ^2 plot. This is due to the behaviour of the matrix elements $|\tilde{U}_{ei}|^2$ evaluated at the center of the sun (compare to equation 5.19). To illustrate this effect, the solar spectrum for three points in the interesting region for $\epsilon \sim -25$ is shown in figure 5.12. As one can see, there is a sharp transition happening, when going from lower to higher $\sin^2\theta_{24}$. For an analytical description, consider the matrix element $|\tilde{U}_{e4}|^2$ in the two flavour approximation framework of section 4.3, which is given by:

$$|\tilde{U}_{e4}|^2 = |U_{\mu 4}|^4 \left(\frac{\frac{\Delta m^2_{41}}{2E}}{A} \right)^2 \left(\frac{A + \frac{\Delta m^2_{41}}{2E} - V_b}{A + \frac{\Delta m^2_{41}}{2E} + V_b} \right)^2 , \tag{5.33}$$

where A is defined in equation 4.16. If the resonance condition is fulfilled, A becomes minimal and thus $|\tilde{U}_{e4}|^2$ resonantly enhanced. This can only happen for negative ϵ (correspondingly negative V_b) and is compatible with our results, since the structure is absent in the $\epsilon > 0$ case. However the question remains, why this has such a large impact on the exclusion limit, since χ^2 is minimized over Δm^2_{41}.

We can find an answer to this question, when looking at the resonance position in the for the solar experiments relevant energy range. For the MINOS results we have already discussed a similar effect in detail. The lower right panel of figure 5.11 shows the shape of the ϵ - Δm^2_{41} parameter region, which is affected by the MSW resonance. This is similar in the solar analysis as illustrated by the solar ϵ - Δm^2_{41} contour plot (figure 5.10). The allowed region, beginning at $\epsilon \sim 100$ up to larger ϵ has the same shape as expected for the ϵ - Δm^2_{41} parameter region in which for low $\sin^2\theta_{24}$ values the resonance is inside the solar energy range. This means that the solar data can be explained by the new baryonic MSW potential, which in the ($\epsilon \sim -27$, $\sin^2\theta_{24} < 4 \cdot 10^{-2}$) region dominates the effect of the standard charged current potential.

Finally, we consider the impact of θ_{34}. As discussed in [6], MINOS and MiniBooNE are not sensitive on this mixing angle. This can be different for the solar data. Therefore, we perform an additional analysis, where we minimize χ^2 over Δm^2_{41} and ϵ. The result is shown in figure 5.13. It indicates that a non-zero θ_{34} could lead to weaker exclusion limits, if we would have included it as a free parameter. Therefore, we examined the effect on the exclusion limit for $\sin^2\theta_{34} = 0.01$ and 0.1, see figure 5.14. The 1σ, 2σ and 3σ confidence levels are shown for the $\sin^2\theta_{24}$ – Δm^2_{41} projection,

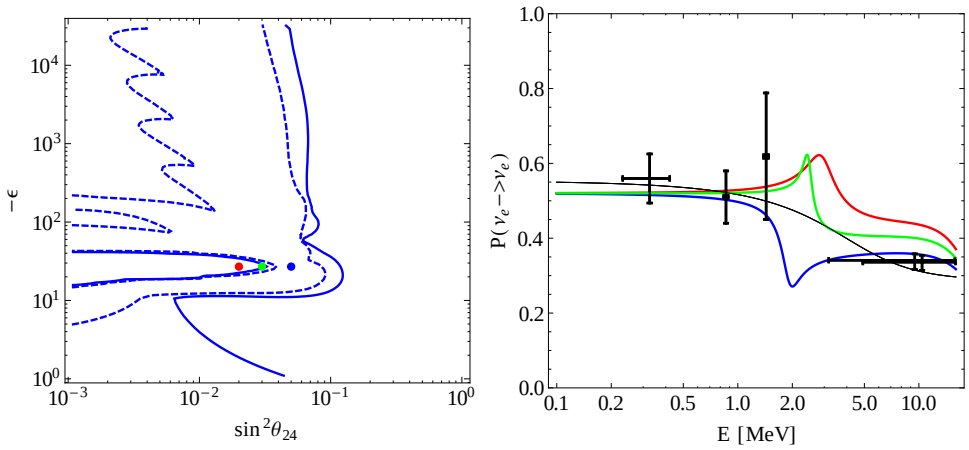

Figure 5.12: Left: the 90% and 99% confidence level contours for the $\epsilon < 0$ solar analysis. The three points indicates the values, for which the spectrum in the right panel is shown. Here we use the mass squared difference $\Delta m^2_{41} = 0.0128$ (corresponding to the best fit) as well as the values $\epsilon = -27$, $\sin^2\theta_{24} = 0.02, 0.03, 0.05$. The black line is calculated for the standard scenario without a fourth neutrino flavour. The structure in the χ^2 plot is only in the $\epsilon < 0$ sector and is due to a resonant transition in the mixing matrix elements relevant for the adiabatic calculation, see equation 5.19.

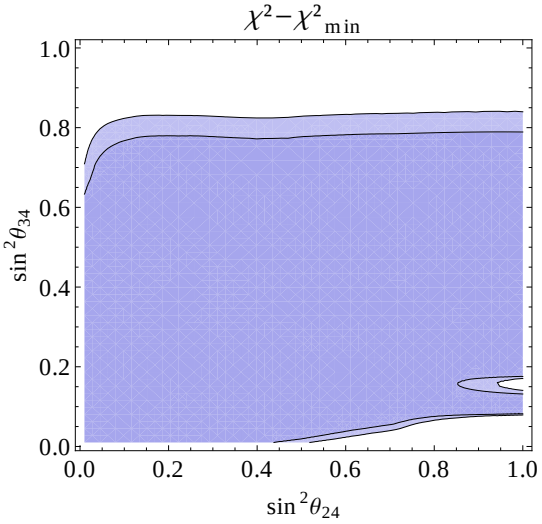

Figure 5.13: The figure shows the 90% and 99% confidence level contours for the solar analysis as function of the two mixing angles θ_{34} and θ_{24} with the purpose to test the dependence of these parameters. The result shows that there is no strong correlation between these angles, thus for $\sin^2\theta_{24} < 0.4$, the angle θ_{34} could essentially have any value below $\sin^2\theta_{34} < 0.6$.

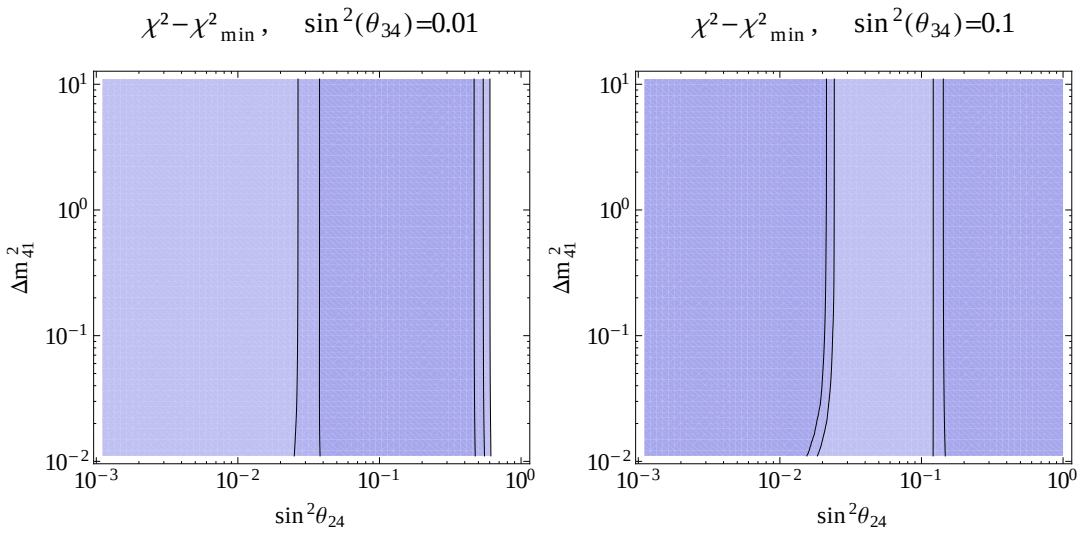

Figure 5.14: The 1σ, 2σ and 3σ confidence levels for the solar χ^2 analysis are shown in the $\sin^2\theta_{24}$ – Δm^2_{41} projection. The difference compared to the lower left panel of figure 5.9 is that the angle θ_{34} has a non-zero value. The left panel shows the contours for $\sin^2\theta_{34} = 0.01$ and the right panel for $\sin^2\theta_{34} = 0.1$. The comparison shows that the exclusion limit depends on θ_{34} in a sensitive way. At 99% confidence level, the solar data does not restrict Δm^2_{41} and $\sin^2\theta_{24}$ for $\sin^2\theta_{34} = 0.1$.

where it is minimized over ϵ with respect to χ^2. This analysis shows that the limits on the baryonic neutrino model obtained from solar experiments can possibly be avoided by a proper choice of $\sin^2\theta_{34}$.

Chapter 6

Discussion and conclusions

In this thesis, the oscillation phenomenology of a recently proposed sterile neutrino model has been investigated. We have re-derived approximate formula for the oscillation probabilities in this model and performed a numerical χ^2 analysis with data sets from MINOS, MiniBooNE and solar experiments. The results show that sterile neutrinos with non-standard interactions can not resolve the tensions, which are due to the short-baseline anomaly. In the following we give a short summary of each chapter, discuss the results and draw conclusions from our analysis.

With the Standard Model as starting point, we introduced in chapter two the concept of neutrino masses and mixing in the context of the general Dirac+Majorana case. We discussed the two and three flavour oscillation probabilities in vacuum and explained the Mikheyev-Smirnov-Wolfenstein effect of resonant neutrino flavour transitions in matter.

In chapter three the development of the by now established picture of neutrino oscillations has been reviewed. We described the discovery of the *solar neutrino problem* and its solution as the first strong evidence for neutrino oscillation. This discovery were followed by atmospheric, accelerator and reactor experiments, which completed our knowledge of the three flavour mass and mixing parameters. Current and future oscillation experiments will focus on the determination of the mass hierarchy, the CP-phase, and on resolving the octant degeneracy. Although most experiments are compatible with this standard picture of three flavour oscillation, there are hints for active-sterile oscillations, which arise in the Gallium, short-baseline and reactor neutrino anomaly. We have seen that in usual sterile neutrino scenarios, there are severe tensions in the appearance and disappearance channels, mostly driven by the LSND/MiniBooNE signals.

As a possible solution to these anomalies a sterile neutrino model has been presented

in chapter four with the original motivation to explain controversial signals in current dark matter direct detection experiments. In this model a neutrino-baryon coupling is introduced with an interaction strength of a few orders of magnitude stronger than the weak interaction. Karagiorgi, Shaevitz and Conrad had the idea that due to this matter interaction the short-baseline anomaly can be explained without being in conflict with constraints from other experiments. We re-derived approximate formulas and found deviations in the MINOS relevant parameter region, whereas in the MiniBooNE sector their approximation led to the same conclusions at the relevant low-energy region.

Finally, in chapter five, we simulated the MINOS disappearance experiment at event rate level, accounting for the background, systematic uncertainties, energy smearing and calculated the average neutrino path length and matter density. We have checked that the simulation can reproduce the MINOS limit obtained from a sterile neutrino fit by Kopp et al. as well as the two flavour fit by MINOS. Data from MiniBooNE and solar experiments are analysed at event ratio level. We checked that flavour transitions inside the sun are still in the adiabatic regime even for large matter potentials and calculated the adiabatic survival probability. We accounted for the incoherent neutrino superposition, but neglected matter effects coming from the neutrino propagation in the earth. We have seen that such a large matter potential has a huge impact on solar oscillation experiments as well as the MINOS experiment, which is due to the new MSW resonance.

We fixed the standard three flavour parameters at values from a global fit, set $\theta_{34} = 0$, chose θ_{14} such that the reactor anomaly is explained and assumed normal hierarchy. In this setting, we investigated the effect of the baryonic model for the MINOS, MiniBooNE and solar data performing a χ^2 analysis, where we scanned over the parameters Δm^2_{41}, $\sin^2\theta_{24}$ and the baryonic potential. We found that the LSND/MiniBooNE best fit from Karagiorgi et al. is excluded by the MINOS and solar limits at 99% confidence level. At this point, we want to point out that the effect of a non-zero mixing angle θ_{34} on the solar analysis can lead to a weaker limit. Including the matter effect of the earth could in principal also lead to a significant change in our results, since one can expect additional effects of MSW resonances. However, the main exclusion limit is due to the MINOS and MiniBooNE data sets, which are not sensitive on θ_{34} as shown by Kopp et al. Thus, we conclude that the results of our analysis give no evidence that the tensions due to the short-baseline anomaly can be resolved by the baryonic neutrino model. Furthermore, assuming that the controversial MiniBooNE signal is due to active-sterile mixing in a three active

plus one sterile neutrino framework we conclude that the interesting parameter range (i.e. baryonic interactions, which are 10^1 to 10^4 times stronger than the weak force) for the baryonic matter potential is disfavoured at 90% confidence level.

In focusing on the oscillation phenomenology, we did not describe the impact of cosmology on sterile neutrinos. The Big Bang Nucleosynthesis, Cosmic Microwave background and large-scale structure formation constrain the introduction of new neutrino flavours. However, these cosmological constraints can be avoided for sterile neutrinos of masses $\sim$ eV, if they are charged under a new gauge group with a light gauge boson as in the baryonic neutrino model. This is discussed in detail in reference [105].

Finally, we want to point out that the Nucifer experiment [76] has the potential to solve the question, whether or not the anomalies are due to active-sterile neutrino oscillations. This is possible, because Nucifer is designed to test reactor fluxes at very short baselines of only seven meters. The experiment already started data taking. First results ere expected in the next two to three years [106].

Acknowledgements

First of all, I would like to thank Joachim Kopp for supervising my work including helpful explanations, inspiring discussions and especially for his motivating way of leading his group members. I am also thankful that he sent me to the ISAPP summer school in Canfranc-Estacion about neutrinos and cosmology.

I want to thank Manfred Lindnder and all group members for helpful and interesting discussions as well as for their contribution to a nice atmosphere. In particular, I am thankful to Stefan Bruenner, Dominik Scala, Pascal Humbert, Simon Stemmle, Dominick Cichon, Lisa Michaels, Dominik Stolzenburg, Sebastian Ohmer, Ludwig Rauch, Steffen Schmidt, Tim Wolf and Meike Danisch, I shared the office with.

I am especially grateful to Ludwig Rauch, Julian Heeck, Sebastian Ohmer and Stefan Bruenner for carefully proof-reading this work.

Schließlich möchte ich mich noch ganz besonders bedanken bei meiner Frau Esther und bei meinen Eltern, Heidi und René. Bei euch habe ich immer ein offenes Ohr gefunden und ihr habt mir Halt gegeben, wenn ich es besonders gebraucht habe. Ebenso bedanke ich mich bei meinen Freunden Kornelius Israel und Simon Danner für ihre konstante Unterstützung und Ermutigung.

Bibliography

[1] **ATLAS Collaboration**, G. Aad *et al.*, "*Observation of a new particle in the search for the Standard Model Higgs boson with the ATLAS detector at the LHC*," Phys.Lett. **B716** (2012) 1–29, arXiv:1207.7214 [hep-ex].

[2] **CMS Collaboration**, S. Chatrchyan *et al.*, "*Observation of a new boson at a mass of 125 GeV with the CMS experiment at the LHC*," Phys.Lett. **B716** (2012) 30–61, arXiv:1207.7235 [hep-ex].

[3] **ATLAS Collaboration**, "*Combined coupling measurements of the Higgs-like boson with the ATLAS detector using up to 25 fb^{-1} of proton-proton collision data*,".

[4] **CMS Collaboration**, "*Combination of standard model Higgs boson searches and measurements of the properties of the new boson with a mass near 125 GeV*,".

[5] B. Pontecorvo, "*Neutrino Experiments and the Problem of Conservation of Leptonic Charge*," Sov.Phys.JETP **26** (1968) 984–988.

[6] J. Kopp, P. A. N. Machado, M. Maltoni, and T. Schwetz, "*Sterile Neutrino Oscillations: The Global Picture*," JHEP **1305** (2013) 050, arXiv:1303.3011 [hep-ph].

[7] G. Karagiorgi, M. Shaevitz, and J. Conrad, "*Confronting the Short-Baseline Oscillation Anomalies with a Single Sterile Neutrino and Non-Standard Matter Effects*," arXiv:1202.1024 [hep-ph].

[8] M. Pospelov, "*Neutrino Physics with Dark Matter Experiments and the*

Signature of New Baryonic Neutral Currents," Phys.Rev. **D84** (2011) 085008, arXiv:1103.3261 [hep-ph].

[9] R. Harnik, J. Kopp, and P. A. Machado, "*Exploring nu Signals in Dark Matter Detectors*," JCAP **1207** (2012) 026, arXiv:1202.6073 [hep-ph].

[10] M. R. Buckley, D. Hooper, J. Kopp, and E. Neil, "*Light Z' Bosons at the Tevatron*," Phys.Rev. **D83** (2011) 115013, arXiv:1103.6035 [hep-ph].

[11] E. K. Akhmedov, "*Neutrino physics*," arXiv:hep-ph/0001264 [hep-ph].

[12] M. Srednicki, *Quantum Field Theory*. Cambridge University Press, New York, 2007.

[13] C. Giunti, C. Kim, and U. Lee, "*Comments on the weak states of neutrinos*," Phys.Rev. **D45** (1992) 2414–2420.

[14] C. Giunti, "*Fock states of flavor neutrinos are unphysical*," Eur.Phys.J. **C39** (2005) 377–382, arXiv:hep-ph/0312256 [hep-ph].

[15] R. N. Mohapatra and P. B. Pal, "*Massive neutrinos in physics and astrophysics*," World Sci.Lect.Notes Phys. **60** (1998) 1–397.

[16] C. Giunti and C. W. Kim, *Fundamentals of Neutrino Physics and Astrophysics*. OUP Oxford, New York, 2007.

[17] M. Fukugita and T. Yanagida, *Physics of Neutrinos and Applications to Astrophysics*. Springer Verlag, Berlin, Heidelberg, New York, 2003.

[18] D. O. Caldwell, *Current Aspects of Neutrino Physics*. Springer Verlag, Berlin, Heidelberg, New York, 2001.

[19] J. N. Bahcall, "*Solar models: An Historical overview*," AAPPS Bull. **12N4** (2002) 12–19, arXiv:astro-ph/0209080 [astro-ph].

[20] J. N. Bahcall, A. M. Serenelli, and S. Basu, "*New solar opacities, abundances, helioseismology, and neutrino fluxes*," Astrophys.J. **621** (2005) L85–L88, arXiv:astro-ph/0412440 [astro-ph].

[21] J. N. Bahcall and C. Pena-Garay, "*Solar models and solar neutrino oscillations*," New J.Phys. **6** (2004) 63, arXiv:hep-ph/0404061 [hep-ph].

[22] B. Cleveland, T. Daily, J. Davis, Raymond, J. R. Distel, K. Lande, *et al.*, "*Measurement of the solar electron neutrino flux with the Homestake chlorine detector*," Astrophys.J. **496** (1998) 505–526.

[23] **GALLEX Collaboration**, W. Hampel *et al.*, "*GALLEX solar neutrino observations: Results for GALLEX IV*," Phys.Lett. **B447** (1999) 127–133.

[24] **GNO Collaboration**, M. Altmann *et al.*, "*GNO solar neutrino observations: Results for GNO I*," Phys.Lett. **B490** (2000) 16–26, arXiv:hep-ex/0006034 [hep-ex].

[25] **SAGE Collaboration**, J. Abdurashitov *et al.*, "*Measurement of the solar neutrino capture rate with gallium metal*," Phys.Rev. **C60** (1999) 055801, arXiv:astro-ph/9907113 [astro-ph].

[26] **Kamiokande Collaboration**, Y. Fukuda *et al.*, "*Solar neutrino data covering solar cycle 22*," Phys.Rev.Lett. **77** (1996) 1683–1686.

[27] **Super-Kamiokande Collaboration**, S. Fukuda *et al.*, "*Solar B-8 and hep neutrino measurements from 1258 days of Super-Kamiokande data*," Phys.Rev.Lett. **86** (2001) 5651–5655, arXiv:hep-ex/0103032 [hep-ex].

[28] **SNO Collaboration**, J. Boger *et al.*, "*The Sudbury neutrino observatory*," Nucl.Instrum.Meth. **A449** (2000) 172–207, arXiv:nucl-ex/9910016 [nucl-ex].

[29] **SNO Collaboration**, Q. Ahmad *et al.*, "*Direct evidence for neutrino flavor transformation from neutral current interactions in the Sudbury Neutrino Observatory*," Phys.Rev.Lett. **89** (2002) 011301, arXiv:nucl-ex/0204008 [nucl-ex].

[30] **SNO Collaboration**, S. Ahmed *et al.*, "*Measurement of the total active B-8 solar neutrino flux at the Sudbury Neutrino Observatory with enhanced neutral current sensitivity*," Phys.Rev.Lett. **92** (2004) 181301, arXiv:nucl-ex/0309004 [nucl-ex].

[31] **SNO Collaboration**, B. Aharmim *et al.*, "*Electron energy spectra, fluxes, and day-night asymmetries of B-8 solar neutrinos from measurements with NaCl dissolved in the heavy-water detector at the Sudbury Neutrino Observatory*," Phys.Rev. **C72** (2005) 055502, arXiv:nucl-ex/0502021 [nucl-ex].

[32] **SNO Collaboration**, B. Aharmim *et al.*, "*An Independent Measurement of the Total Active B-8 Solar Neutrino Flux Using an Array of He-3 Proportional Counters at the Sudbury Neutrino Observatory*," Phys.Rev.Lett. **101** (2008) 111301, arXiv:0806.0989 [nucl-ex].

[33] **GALLEX Collaboration**, P. Anselmann *et al.*, "*First results from the Cr-51 neutrino source experiment with the GALLEX detector*," Phys.Lett. **B342** (1995) 440–450.

[34] **GALLEX Collaboration**, W. Hampel *et al.*, "*Final results of the Cr-51 neutrino source experiments in GALLEX*," Phys.Lett. **B420** (1998) 114–126.

[35] F. Kaether, W. Hampel, G. Heusser, J. Kiko, and T. Kirsten, "*Reanalysis of the GALLEX solar neutrino flux and source experiments*," Phys.Lett. **B685** (2010) 47–54, arXiv:1001.2731 [hep-ex].

[36] D. Abdurashitov, V. Gavrin, S. Girin, V. Gorbachev, T. V. Ibragimova, *et al.*, "*The Russian-American gallium experiment (SAGE) Cr neutrino source measurement*," Phys.Rev.Lett. **77** (1996) 4708–4711.

[37] **SAGE Collaboration**, J. Abdurashitov *et al.*, "*Measurement of the response of the Russian-American gallium experiment to neutrinos from a Cr-51 source*," Phys.Rev. **C59** (1999) 2246–2263, arXiv:hep-ph/9803418 [hep-ph].

[38] J. Abdurashitov, V. Gavrin, S. Girin, V. Gorbachev, P. Gurkina, *et al.*, "*Measurement of the response of a Ga solar neutrino experiment to neutrinos from an Ar-37 source*," Phys.Rev. **C73** (2006) 045805, arXiv:nucl-ex/0512041 [nucl-ex].

[39] **SAGE Collaboration**, J. Abdurashitov *et al.*, "*Measurement of the solar neutrino capture rate with gallium metal. III: Results for the 2002–2007 data-taking period*," Phys.Rev. **C80** (2009) 015807, arXiv:0901.2200 [nucl-ex].

[40] C. Giunti and M. Laveder, "*Statistical Significance of the Gallium Anomaly*," Phys.Rev. **C83** (2011) 065504, arXiv:1006.3244 [hep-ph].

[41] **Kamiokande-II Collaboration**, K. Hirata *et al.*, "*Observation of a small atmospheric muon-neutrino / electron-neutrino ratio in Kamiokande*," Phys.Lett. **B280** (1992) 146–152.

[42] J. W. Flanagan, J. G. Learned, and S. Pakvasa, "*Up - down asymmetry: A Diagnostic for neutrino oscillations*," Phys.Rev. **D57** (1998) 2649–2652, arXiv:hep-ph/9709438 [hep-ph].

[43] **Kamiokande Collaboration**, S. Hatakeyama *et al.*, "*Measurement of the flux and zenith angle distribution of upward through going muons in Kamiokande II + III*," Phys.Rev.Lett. **81** (1998) 2016–2019, arXiv:hep-ex/9806038 [hep-ex].

[44] R. Becker-Szendy, C. Bratton, D. Casper, S. Dye, W. Gajewski, *et al.*, "*The Electron-neutrino and muon-neutrino content of the atmospheric flux*," Phys.Rev. **D46** (1992) 3720–3724.

[45] D. Casper, R. Becker-Szendy, C. Bratton, D. Cady, R. Claus, *et al.*, "*Measurement of atmospheric neutrino composition with IMB-3*," Phys.Rev.Lett. **66** (1991) 2561–2564.

[46] R. Becker-Szendy, C. Bratton, D. Casper, S. Dye, W. Gajewski, *et al.*, "*A Search for muon-neutrino oscillations with the IMB detector*," Phys.Rev.Lett. **69** (1992) 1010–1013.

[47] R. Clark, R. Becker-Szendy, C. Bratton, J. Breault, D. Casper, *et al.*, "*Atmospheric muon-neutrino fraction above 1-GeV*," Phys.Rev.Lett. **79** (1997) 345–348.

[48] E. Kearns, "*Experimental measurements of atmospheric neutrinos*," Nucl.Phys.Proc.Suppl. **70** (1999) 315–323, arXiv:hep-ex/9803007 [hep-ex].

[49] **Super-Kamiokande Collaboration**, Y. Fukuda *et al.*, "*Evidence for oscillation of atmospheric neutrinos*," Phys.Rev.Lett. **81** (1998) 1562–1567, arXiv:hep-ex/9807003 [hep-ex].

[50] **Soudan 2 Collaboration**, M. C. Sanchez *et al.*, "*Measurement of the L/E distributions of atmospheric neutrinos in Soudan 2 and their interpretation as neutrino oscillations*," Phys.Rev. **D68** (2003) 113004, arXiv:hep-ex/0307069 [hep-ex].

[51] **Soudan-2 Collaboration**, W. Allison *et al.*, "*Neutrino oscillation effects in Soudan-2 upward-stopping muons*," Phys.Rev. **D72** (2005) 052005, arXiv:hep-ex/0507068 [hep-ex].

[52] **MACRO Collaboration**, M. Ambrosio *et al.*, "*Matter effects in upward going muons and sterile neutrino oscillations*," Phys.Lett. **B517** (2001) 59–66, arXiv:hep-ex/0106049 [hep-ex].

[53] **MACRO Collaboration**, M. Ambrosio *et al.*, "*Atmospheric neutrino oscillations from upward through going muon multiple scattering in MACRO*," Phys.Lett. **B566** (2003) 35–44, arXiv:hep-ex/0304037 [hep-ex].

[54] H. Kwon, F. Boehm, A. Hahn, H. Henrikson, J. Vuilleumier, *et al.*, "*Search for Neutrino Oscillations at a Fission Reactor*," Phys.Rev. **D24** (1981) 1097–1111.

[55] **CALTECH-SIN-TUM COLLABORATION**, G. Zacek *et al.*, "*Neutrino Oscillation Experiments at the Gosgen Nuclear Power Reactor*," Phys.Rev. **D34** (1986) 2621–2636.

[56] A. Afonin, S. Bogatov, A. Vershinsky, S. Ketov, Y. Klimov, *et al.*, "$\bar{\nu}_e$ *Spectra at Two Distances From the Reactor of the Rovno Nuclear Power Plant: Search for Oscillations*," JETP Lett. **45** (1987) 247–251.

[57] G. Vidyakin, V. Vyrodov, Y. Kozlov, A. Martemyanov, V. Martemyanov, *et al.*, "*Limitations on the characteristics of neutrino oscillations*," JETP Lett. **59** (1994) 390–393.

[58] Y. Declais, J. Favier, A. Metref, H. Pessard, B. Achkar, *et al.*, "*Search for neutrino oscillations at 15-meters, 40-meters, and 95-meters from a nuclear power reactor at Bugey*," Nucl.Phys. **B434** (1995) 503–534.

[59] Z. Greenwood, W. Kropp, M. Mandelkern, S. Nakamura, E. Pasierb-Love, *et al.*, "*Results of a two position reactor neutrino oscillation experiment*," Phys.Rev. **D53** (1996) 6054–6064.

[60] M. Gonzalez-Garcia, M. Maltoni, J. Salvado, and T. Schwetz, "*Global fit to three neutrino mixing: critical look at present precision*," JHEP **1212** (2012) 123, arXiv:1209.3023 [hep-ph].

[61] **CHOOZ Collaboration**, M. Apollonio *et al.*, "*Limits on neutrino oscillations from the CHOOZ experiment*," Phys.Lett. **B466** (1999) 415–430, arXiv:hep-ex/9907037 [hep-ex].

[62] **CHOOZ Collaboration**, M. Apollonio *et al.*, "*Search for neutrino oscillations on a long baseline at the CHOOZ nuclear power station*," Eur.Phys.J. **C27** (2003) 331–374, arXiv:hep-ex/0301017 [hep-ex].

[63] F. Boehm, J. Busenitz, B. Cook, G. Gratta, H. Henrikson, *et al.*, "*Final results from the Palo Verde neutrino oscillation experiment*," Phys.Rev. **D64** (2001) 112001, arXiv:hep-ex/0107009 [hep-ex].

[64] **DOUBLE-CHOOZ Collaboration**, Y. Abe *et al.*, "*Indication for the disappearance of reactor electron antineutrinos in the Double Chooz experiment*," Phys.Rev.Lett. **108** (2012) 131801, arXiv:1112.6353 [hep-ex].

[65] **Daya Bay Collaboration**, F. An *et al.*, "*A side-by-side comparison of Daya Bay antineutrino detectors*," Nucl.Instrum.Meth. **A685** (2012) 78–97, arXiv:1202.6181 [physics.ins-det].

[66] **RENO Collaboration**, J. Ahn *et al.*, "*RENO: An Experiment for Neutrino Oscillation Parameter θ_{13} Using Reactor Neutrinos at Yonggwang*," arXiv:1003.1391 [hep-ex].

[67] **DAYA-BAY Collaboration**, F. An *et al.*, "*Observation of electron-antineutrino disappearance at Daya Bay*," Phys.Rev.Lett. **108** (2012) 171803, arXiv:1203.1669 [hep-ex].

[68] **RENO collaboration**, J. Ahn *et al.*, "*Observation of Reactor Electron Antineutrino Disappearance in the RENO Experiment*," Phys.Rev.Lett. **108** (2012) 191802, arXiv:1204.0626 [hep-ex].

[69] **Double Chooz Collaboration**, Y. Abe *et al.*, "*First Measurement of θ_{13} from Delayed Neutron Capture on Hydrogen in the Double Chooz Experiment*," Phys.Lett. **B723** (2013) 66–70, arXiv:1301.2948 [hep-ex].

[70] **Double Chooz Collaboration**, Y. Abe *et al.*, "*Reactor electron antineutrino disappearance in the Double Chooz experiment*," Phys.Rev. **D86** (2012) 052008, arXiv:1207.6632 [hep-ex].

[71] **KamLAND Collaboration**, K. Eguchi *et al.*, "*First results from KamLAND: Evidence for reactor anti-neutrino disappearance*," Phys.Rev.Lett. **90** (2003) 021802, arXiv:hep-ex/0212021 [hep-ex].

[72] **KamLAND Collaboration**, A. Gando *et al.*, "*Constraints on θ_{13} from A Three-Flavor Oscillation Analysis of Reactor Antineutrinos at KamLAND*," Phys.Rev. **D83** (2011) 052002, arXiv:1009.4771 [hep-ex].

[73] G. Mention, M. Fechner, T. Lasserre, T. Mueller, D. Lhuillier, *et al.*, "*The Reactor Antineutrino Anomaly*," Phys.Rev. **D83** (2011) 073006, arXiv:1101.2755 [hep-ex].

[74] **ALEPH Collaboration, DELPHI Collaboration, L3 Collaboration, OPAL Collaboration, SLD Collaboration, LEP Electroweak Working Group, SLD Electroweak Group, SLD Heavy Flavour Group**, S. Schael *et al.*, "*Precision electroweak measurements on the Z resonance*," Phys.Rept. **427** (2006) 257–454, arXiv:hep-ex/0509008 [hep-ex].

[75] A. Hayes, J. Friar, G. Garvey, and G. Jonkmans, "*Reanalysis of the Reactor Neutrino Anomaly*," arXiv:1309.4146 [nucl-th].

[76] **Nucifer Collaboration**, A. Porta, "*Reactor neutrino detection for non proliferation with the Nucifer experiment*," J.Phys.Conf.Ser. **203** (2010) 012092.

[77] **K2K Collaboration**, M. Ahn *et al.*, "*Measurement of Neutrino Oscillation by the K2K Experiment*," Phys.Rev. **D74** (2006) 072003, arXiv:hep-ex/0606032 [hep-ex].

[78] **MINOS Collaboration**, D. Michael *et al.*, "*Observation of muon neutrino disappearance with the MINOS detectors and the NuMI neutrino beam*," Phys.Rev.Lett. **97** (2006) 191801, arXiv:hep-ex/0607088 [hep-ex].

[79] **MINOS Collaboration**, P. Adamson *et al.*, "*Improved search for muon-neutrino to electron-neutrino oscillations in MINOS*," Phys.Rev.Lett. **107** (2011) 181802, arXiv:1108.0015 [hep-ex].

[80] **T2K Collaboration**, K. Abe *et al.*, "*Evidence of Electron Neutrino Appearance in a Muon Neutrino Beam*," Phys.Rev. **D88** (2013) 032002, arXiv:1304.0841 [hep-ex].

[81] **MINOS Collaboration**, J. de Jong, "*Near-to-Final MINOS Oscillation Results*," Nucl.Phys.Proc.Suppl. **237-238** (2013) 166–169.

[82] **collaboration for the T2K**, K. Abe *et al.*, "*Observation of Electron Neutrino Appearance in a Muon Neutrino Beam*," arXiv:1311.4750 [hep-ex].

[83] **LSND Collaboration**, A. Aguilar-Arevalo *et al.*, "*Evidence for neutrino oscillations from the observation of anti-neutrino(electron) appearance in a anti-neutrino(muon) beam*," Phys.Rev. **D64** (2001) 112007, arXiv:hep-ex/0104049 [hep-ex].

[84] **LSND Collaboration**, C. Athanassopoulos *et al.*, "*Evidence for anti-muon-neutrino to anti-electron-neutrino oscillations from the LSND experiment at LAMPF*," Phys.Rev.Lett. **77** (1996) 3082–3085, arXiv:nucl-ex/9605003 [nucl-ex].

[85] **LSND Collaboration**, C. Athanassopoulos *et al.*, "*Evidence for nu(mu) to nu(e) neutrino oscillations from LSND*," Phys.Rev.Lett. **81** (1998) 1774–1777, arXiv:nucl-ex/9709006 [nucl-ex].

[86] **MiniBooNE Collaboration**, A. Aguilar-Arevalo *et al.*, "*The MiniBooNE Detector*," Nucl.Instrum.Meth. **A599** (2009) 28–46, arXiv:0806.4201 [hep-ex].

[87] **MiniBooNE Collaboration**, A. Aguilar-Arevalo *et al.*, "*Improved Search for $\bar{\nu}_\mu \to \bar{\nu}_e$ Oscillations in the MiniBooNE Experiment*," Phys.Rev.Lett. **110** (2013) 161801, arXiv:1207.4809 [hep-ex].

[88] B. Armbruster, I. Blair, B. Bodmann, N. Booth, G. Drexlin, *et al.*, "*KARMEN limits on electron-neutrino to tau-neutrino oscillations in two neutrino and three neutrino mixing schemes*," Phys.Rev. **C57** (1998) 3414–3424, arXiv:hep-ex/9801007 [hep-ex].

[89] C. Rubbia, M. Antonello, P. Aprili, B. Baibussinov, M. B. Ceolin, *et al.*, "*Underground operation of the ICARUS T600 LAr-TPC: first results*," JINST **6** (2011) P07011, arXiv:1106.0975 [hep-ex].

[90] **NOMAD Collaboration**, P. Astier *et al.*, "*Search for nu(mu) to nu(e) oscillations in the NOMAD experiment*," Phys.Lett. **B570** (2003) 19–31, arXiv:hep-ex/0306037 [hep-ex].

[91] L. Borodovsky, C. Chi, Y. Ho, N. Kondakis, W.-Y. Lee, *et al.*, "*Search for muon-neutrino oscillations (muon-neutrino to electron-neutrino,*

anti-muon-neutrino to anti-electron-neutrino) in a wide band neutrino beam," Phys.Rev.Lett. **68** (1992) 274–277.

[92] **DAMA Collaboration**, R. Bernabei *et al.*, "*First results from DAMA/LIBRA and the combined results with DAMA/NaI*," Eur.Phys.J. **C56** (2008) 333–355, arXiv:0804.2741 [astro-ph].

[93] **CoGeNT collaboration**, C. Aalseth *et al.*, "*Results from a Search for Light-Mass Dark Matter with a P-type Point Contact Germanium Detector*," Phys.Rev.Lett. **106** (2011) 131301, arXiv:1002.4703 [astro-ph.CO].

[94] **MiniBooNE Collaboration**, A. Aguilar-Arevalo *et al.*, "*Unexplained Excess of Electron-Like Events From a 1-GeV Neutrino Beam*," Phys.Rev.Lett. **102** (2009) 101802, arXiv:0812.2243 [hep-ex].

[95] **MiniBooNE Collaboration**, A. Aguilar-Arevalo *et al.*, "*Event Excess in the MiniBooNE Search for $\bar{\nu}_\mu \to \bar{\nu}_e$ Oscillations*," Phys.Rev.Lett. **105** (2010) 181801, arXiv:1007.1150 [hep-ex].

[96] P. Huber, J. Kopp, M. Lindner, M. Rolinec, and W. Winter, "*GLoBES Manual*," September, 2013. http://www.mpi-hd.mpg.de/personalhomes/globes/documentation/globes-manual-3.0.8.pdf.

[97] G. Fogli, E. Lisi, A. Marrone, D. Montanino, and A. Palazzo, "*Getting the most from the statistical analysis of solar neutrino oscillations*," Phys.Rev. **D66** (2002) 053010, arXiv:hep-ph/0206162 [hep-ph].

[98] C. Giunti, "*Coherence and wave packets in neutrino oscillations*," Found.Phys.Lett. **17** (2004) 103–124, arXiv:hep-ph/0302026 [hep-ph].

[99] D. Anderson, *Theory of the Earth*. Blackwell Scientific Publications, 1989.

[100] M. Diwan, B. Viren, D. Harris, A. Marchionni, J. Morfin, *et al.*, "*Ion Chambers for Monitoring the NuMI Beam at FNAL*,".

[101] P. Huber, M. Lindner, and W. Winter, "*Simulation of long-baseline neutrino oscillation experiments with GLoBES (General Long Baseline Experiment Simulator)*," Comput.Phys.Commun. **167** (2005) 195, arXiv:hep-ph/0407333 [hep-ph].

[102] P. Huber, J. Kopp, M. Lindner, M. Rolinec, and W. Winter, "*New features in the simulation of neutrino oscillation experiments with GLoBES 3.0: General Long Baseline Experiment Simulator*," Comput.Phys.Commun. **177** (2007) 432–438, arXiv:hep-ph/0701187 [hep-ph].

[103] **MINOS Collaboration**, P. Adamson *et al.*, "*Measurement of Neutrino and Antineutrino Oscillations Using Beam and Atmospheric Data in MINOS*," Phys.Rev.Lett. **110** (2013) 251801, arXiv:1304.6335 [hep-ex].

[104] **Borexino Collaboration**, G. Bellini *et al.*, "*Final results of Borexino Phase-I on low energy solar neutrino spectroscopy*," arXiv:1308.0443 [hep-ex].

[105] B. Dasgupta and J. Kopp, "*A ménage à trois of eV-scale sterile neutrinos, cosmology, and structure formation*," arXiv:1310.6337 [hep-ph].

[106] M. Lindner. Personal communication, 2013.

Erklärung:

Ich versichere, dass ich diese Arbeit selbstständig verfasst habe und keine anderen als die angegebenen Quellen und Hilfsmittel benutzt habe.

Heidelberg, den (Datum) .....